Fatigue behavior of an adhesive under mixed-mode conditions

Mário Rui Oliveira Cunha

A dissertation submited for the degree of Master of Science in Mechanical Engineering to Faculdade de Engenharia, Universidade do Porto

Supervisor: Lucas da Silva

Co-supervisors: Marcelo Costa & Ricardo Carbas

June 2018

To my grandmother…

Abstract

The use of structural adhesives is increasing globally, due in part to the increased use of composite materials, but also to the replacement of conventional bonding methods. This trend is explained by weight reduction and improved performance of adhesives when compared to the traditional bonding methods.

With the increased use of adhesives in industries, it becomes important to characterize the adhesive under conditions that replicate the actual work conditions. And even though a joint is designed to be subjected to shear stresses, in real situations, they are under mixed-mode stresses, namely shear and opening stresses. In real scenarios, it is often found that rupture happens due to prolonged exposure to cyclic loads, making it important to understand the fatigue behavior of adhesive joints.

The aim of this dissertation is to study the fatigue behavior of an adhesive loaded in mixed-mode conditions. For this, several fracture tests were performed: Double Cantilever Beam (DCB) for pure mode I, End Notched Flexure (ENF) for pure mode II, and mixed-mode testing using an apparatus that allows to perform mixed-mode combinations between mode I and II. A numerical study was also performed for the static tests using finite elements models implemented in ABAQUS®.

The fracture envelope was calculated using the mixed-mode apparatus, where the values seem to be compatible with a quadratic criterion. A quadratic law criterion was developed to fit the envelope. The fatigue behavior was studied recurring to fatigue crack growth (FCG) curves for the same types of loads studied in the quasi-static tests. A relation between mixed-mode phase angle and Paris law slope was found, where the existence of mode II loads delays the crack propagation. By performing fatigue tests at 60% and 80% of the maximum load, it was noticed that increasing the load leads to an increase of the threshold energy release rate values.

Comportamento à fadiga de um adesivo solicitado em modo-misto

Resumo

A utilização de adesivos estruturais tem aumentado globalmente, isto deve-se em parte ao aumento do uso de materiais compósitos, mas também à substituição de métodos convencionais de ligação. Esta tendência deve-se a vantagens em termos de redução de peso e melhoria do desempenho.

Com o aumento do uso de adesivos nas indústrias, torna-se importante caracterizar o adesivo em condições que aproximam as condições reais. Apesar de uma junta ser projetada para estar sujeita a tensões de corte, em situações reais, ficam sujeitas a solicitações de modo-misto, nomeadamente tensões de corte e de abertura.

Em situações reais, muitas vezes verifica-se que a rotura é induzida devido à exposição prolongada a cargas cíclicas, pelo que é importante entender o comportamento à fadiga de juntas adesivas.

O objetivo da dissertação é estudar o comportamento à fadiga de um adesivo em modo-misto. Para isso, começou-se por fazer testes de fratura para os modos puros I e II, utilizando os testes *Double Cantilever Beam* (DCB) e *End Notched Flexure* (ENF), respetivamente, e testes em modo-misto utilizando um dispositivo que permite várias combinações de carga entre modo I e modo II. As taxas de libertação de energia foram calculadas recorrendo ao *Compliance Based Beam Method* (CBBM). Foi também realizado um estudo numérico para os testes quási-estáticos recorrendo a modelos de elementos finitos implementados em ABAQUS®.

O envelope de fratura foi calculado usando um aparelho de modo-misto, o que permitiu verificar que o envelope segue um critério quadrático. Uma lei quadrática foi desenvolvida para aproximar a forma do envelope. O comportamento à fadiga foi obtido por intermédio de curvas de crescimento de fenda para os mesmos tipos de carga estudados nos ensaios quase-estáticos. Verificou-se a existência de uma relação entre o ângulo de modo-misto e o declive da lei de Paris: a presença de forças de modo II atrasa a propagação da fenda. Os testes de fadiga foram desempenhados a 60% e 80% da máxima carga estática, o que permitiu verificar que o aumento da carga provoca um aumento do limiar de energia de libertação.

Acknowledgements

I would like to thank my supervisor Prof. Lucas da Silva for his attention, and his guidance, without which this dissertation would not have been feasible.

I would like to thank my co-supervisors Marcelo Costa and Ricardo Carbas, who accompanied me as I took my first steps in a research laboratory, for the guidance and for the lessons.

I am grateful for being a piece of what the ADFeup group is. I would like to thank every member of the group, specially Paulo, João, Daniel, Marcos, Mateus, Xinlong and Ata, who completed this walk alongside myself, to José Machado and Eduardo Marques, who were always ready to help me with anything.

I would like to thank Prof. Paulo Tavares de Castro for being available to help with fracture mechanics and any subject in general.

I would also like to thank the personnel at *Laboratório de Ensaios Tecnológicos (LET)*, specifically to Prof. Miguel Figueiredo and Rui Silva who helped me with the machine, making the test of so many specimens possible.

I would like to thank John Deere for supporting this work.

And finally, I want to thank my family and friends for being the rock that never lets me go astray.

Contents

List of symbols and acronyms

Symbols

K_t, Concentration factor

σ_{local}, Stress felt at a specific region

σ_∞, applied remote stress

K, Stress Intensity Factor

K_c, Critical Stress Intensity Factor

G, Strain energy release rate

G_c, Critical Strain energy release rate

G_I, Strain energy release rate in mode I

G_{II}, Strain energy release rate in mode II

ν, Poisson's ratio

a_{eq}, Equivalent crack length

P_{max}, Maximum load

P_{min}, Minimum load

σ_e, Tensile strength

ε_r, Failure strain

Acronyms

ADCB, Asymmetric Double Cantilever Beam

ATDCB, Asymmetric Tapered Double Cantilever Beam

BK, Benzeggagh & Kenane

CBBM, Compliance Based Beam Method

CFRP, Carbon Fiber Reinforced Plastic

CZM, Cohesive Zone Model

DCB, Double Cantilever Beam

ENF, End Notched Flexure

FCG, Fatigue Crack Growth

FPZ, Fracture Process Zone

LVDT, Linear Variable Differential Transformer

MMB, Mixed-mode Bending

PL, Paris law

R-curve, Resistance curve

SLB, Single Leg Bending

TAST, thick adherend shear test

List of Figures

List of tables

1 Introduction

Adhesive technology has been around for a long time, as archeologists found evidence that as far as 200,000 years ago Neanderthals were using a tar based mix to position their spears and axe heads in their handles [1], which shows how intuitive adhesive bonding technology is. The use of adhesives leads to weight reduction, uniform stress distribution when compared with rivets, and flexibility, which allows for better vibration damping and thus improved fatigue behavior.

1.1 Background and motivation

When applied in mechanical components, adhesives are designed to sustain mode II loads, since this way higher loads can be supported. However, this does not match what happens in a real joint, since in practice the load applied is a combination of mode I and mode II. To better understand how an adhesive behaves in these conditions, many articles were published on the mixed-mode fracture behavior of an adhesive. Another problem affecting adhesives, and components in general, is fatigue. Sometimes materials fail without reaching critical stresses because of the damage accumulated by multiple small loads throughout the service time. Mode I and II fatigue is well covered in the literature, but mixed-mode fatigue is still lightly explored. By studying how an adhesive behaves in a fatigue solicitation under mixed-mode conditions, it is possible to make better predictions concerning the behavior of the adhesive in a real situation. Which is why this dissertation aims to answer how the fatigue behavior of an adhesive changes as a function of the mixed-mode phase angle.

1.2 Objectives

The objective of this dissertation is to assess the fatigue behavior of an adhesive loaded in mixed-mode. The experimental results were used to validate the numerical models. Quasi-static testing was required to determine maximum fatigue loads and the elastic properties of the adhesive were determined to use in the numerical models. In summary the objectives are:

- Characterize the adhesive's elastic properties;
- Characterize the adhesive in quasi-static conditions in mode I, mode II and mixed-mode;
- Characterize fatigue behavior in mode I, mode II and mixed-mode;
- Determine a fracture envelope with the quasi-static characterization results;
- Aggregate fatigue test results to determine Paris Law parameters as a function of the mixed-mode angle.

1.3 Research methodology

To complete the proposed objectives, the following research methodology was established:

- Literature review: research of adhesive bonding and fundamental concepts, secondly, researching fracture mechanics, namely, fracture and fatigue test methods;
- Perform bulk tensile tests to assess mechanical properties;
- Double Cantilever Beam (DCB) and End Notched Flexure (ENF) testing to characterize fracture energy in each pure mode;
- Perform mixed-mode tests using an apparatus to characterize fracture energy in mixed-mode for the phase angles, φ=56.6° and φ=22.2°;
- Perform fatigue tests for the quasi-static conditions tested, namely pure mode I, pure mode II and mixed-mode, for φ=22.2° and φ=56.6°;
- Determine the fatigue crack growth curves from the fatigue tests' results and measure Paris law parameters;
- Use ABAQUS® to implement a finite element model to compare with the experimental results.

1.4 Thesis outline

This dissertation is divided in the following sections:

Chapter 2: Overview of the core subjects covered in this dissertation. An introduction to adhesive technology is presented, as well as the theoretical formulation for the fracture and fatigue tests carried out. A quadratic law is proposed as a possible fit to fracture envelopes.

Chapter 3: The used materials and the experimental procedures are explained in this chapter. Contains a detailed explanation of all tests done, such as adhesive characterization tests, as well as fracture and fatigue tests.

Chapter 4: This chapter shows the results obtained for each completed test. A discussion meant to interpret the obtained results is also presented. Fracture energies for each test were compiled in a fracture envelope. The fatigue results contain characteristic FCG curves as well as graphics comparing the obtained parameters according to each condition tested.

Chapter 5: Numerical simulations based on a finite element analysis was carried out using models made in ABAQUS®. The experimental data was used to validate the models created.

Chapter 6: Conclusions and future works.

2 Literature review

2.1 Introduction to adhesive technology

Adhesives are polymeric materials used to "glue" other materials together (adherends), thus opposing their separation. The combination of adherends and the adhesive form an adhesive joint [2]. A schematic representation of an adhesive bond is shown below in Figure 1.

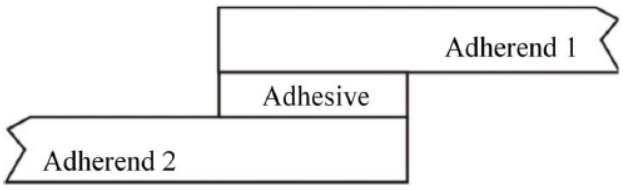

Figure 1 - Adhesive joint [2].

The use of adhesives is increasing steadily because they provide a good alternative to traditional mechanical joints, some advantages being:

- Polymeric properties: low density, ability to bond composite materials, ability to bond dissimilar materials, adds flexibility to the joint making it more resistant to dynamic loadings;
- Geometric properties: with adhesive bonding drill holes and welding marks are avoided and allows the possibility to bond very thin materials. As exemplified in Figure 2, adhesive bonding means that the whole resistive area is bonded together, making the non-reinforced area smaller comparing to traditional mechanical joints while at the same time producing constant shear stress distribution.

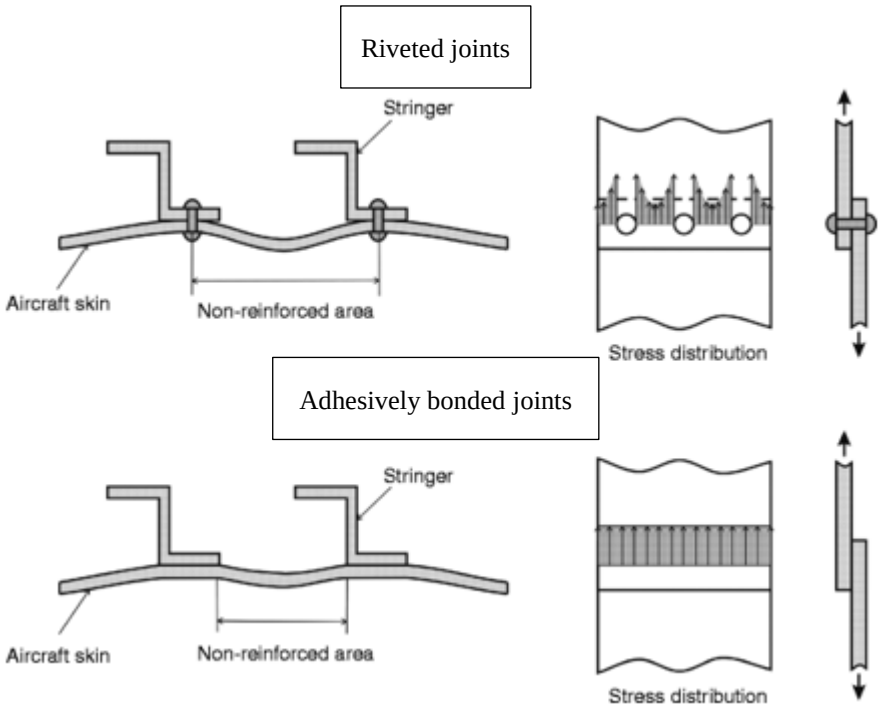

Figure 2 - Adhesive joints compared to riveted joints [3].

Studies have been published to corroborate these advantages: adhesive joints have been compared to mechanical joints, showing that adhesive joints support higher quasi-static loads and more fatigue cycles to failure [4, 5].

2.1.1 Structural adhesives

According to their function, adhesives can be classified into two major groups: structural and non-structural. The main types of structural adhesives are epoxies, polyurethanes, acrylics, phenolics and aromatics. Figure 3 displays some applications according to adhesive type and the respective stress-strain curves.

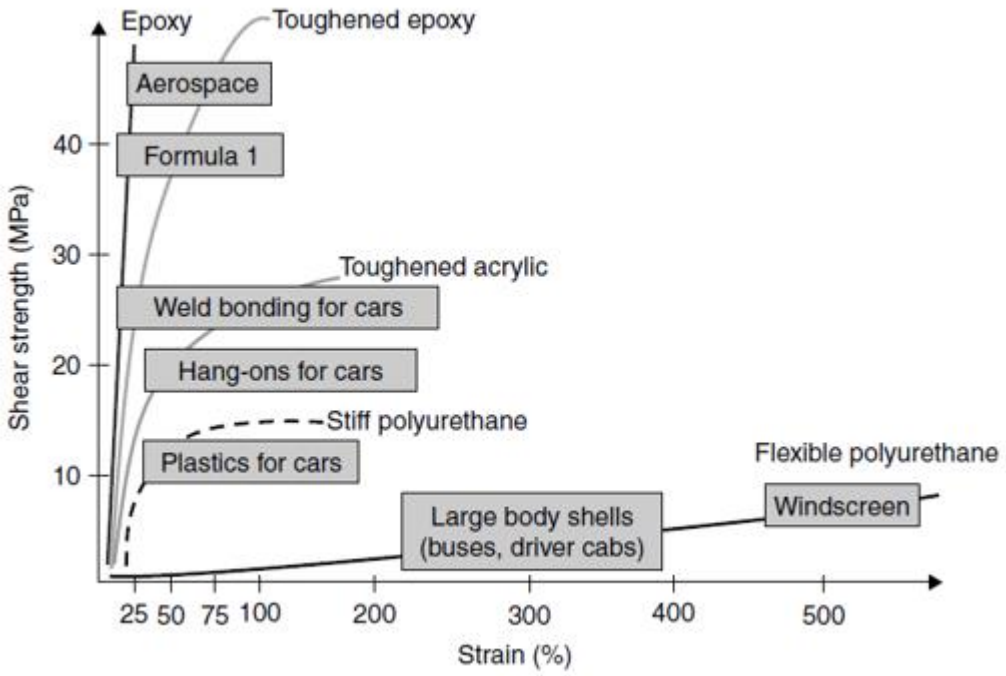

Figure 3 - Shear stress and strain curves for different polymers [6].

Polyurethanes are mainly used when high flexibility is required, their strain to failure can be higher than 300%. Acrylics are known for their fast cure and being able to bond plastics together. Phenolics and aromatics are known for their resistance to temperature, with aromatics resisting higher temperatures and being more expensive. Epoxies are the most used kind of structural adhesives, their main characteristics are high strength and exceptional environmental resistance, plus, they can be chemically modified to have desirable properties.

The use of adhesives to join structural parts is increasing since they provide good properties while contributing to a low weight structure. This increase is particularly substantial in the automotive and other land vehicles industry due to the importance of improving fuel economy and reduce emissions. Figure 4 shows where adhesives can be applied in an agricultural tractor, and the following parts are highlighted:

- Plastic and composite components – 1 and 8
- Door and panel stiffener attachment – 2
- Lower and upper frame assembly – 3 and 4
- Aluminum and stainless components – 5
- Skin to frame assembly – 6
- Bracket attachment – 7

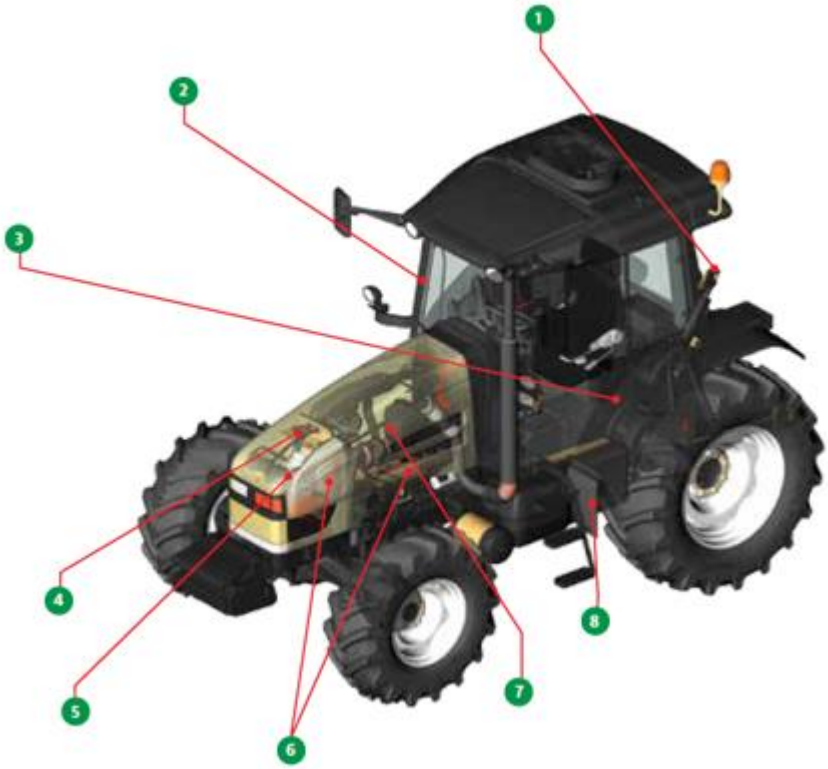

Figure 4 - Adhesive applications in an agricultural tractor [7].

2.1.2 Failure modes

The various types of failure can be seen in Figure 5. Cohesive failure means the crack has propagated in only one material, while adhesive failure means the crack appeared between the bonded materials, through their contact interface.

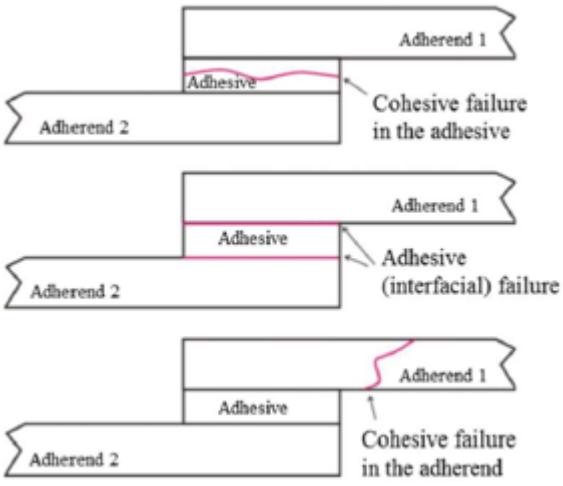

Figure 5- Adhesive failure modes [2].

Ideally, adhesive joints should fail cohesively in the adhesive, because when designing adhesive joints, the adhesive properties are considered. Interfacial failure is difficult to calculate, difficult to predict and thus, undesirable.

2.2 Failure criteria

As adhesives become more common for structural applications, it is important that theories and models are developed to properly assess the failure process. To predict the failure of an adhesive joint, three basic approaches may be followed: continuum mechanics, fracture mechanics or a combination of both, damage mechanics [8].

2.2.1 Continuum mechanics

Continuum mechanics analysis assumes the materials to be defect free, thus, having no pre-existent cracks, the failure criteria is defined in terms of maximum stresses and deformations. These criteria are difficult to apply to adhesive joints due to the singularities in the joint tip geometry as shown in Figure 6, where stresses tend to be infinite [9].

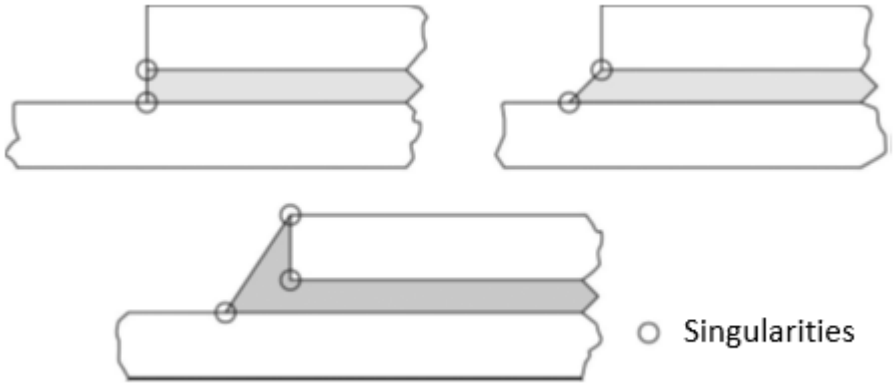

Figure 6 - Singularities in adhesive bonds [9].

2.2.2 Fracture mechanics

By contrast, fracture mechanics is a theory that assumes materials have defects. And even though nowadays fracture mechanics is considered a core subject that deserves attention, in the past, cracks were commonly thought to be insignificant and that they, for instance, could never affect a big structure like a ship or a plane. During World War II and briefly after, accidents

occurred, with many ships and aircrafts suddenly failing. It was later known that the cause for these problems were cracks in the metallic structures [10].

During this period the common way to predict critical areas where a structure might fail was using the concentration factor, K_t. This factor is a quotient between the local tension felt at a specific area σ_{local}, and the remote tension known to be applied in the structure σ_∞, as can be seen in Equation (1):

$$K_t = \frac{\sigma_{local}}{\sigma_\infty} \tag{1}$$

This factor varies with the geometry of the structure and is important from a macroscopical standpoint. But, as fracture studies began to appear, it was obvious that it could not be applied to microscopical cracks. This is due to the fact that a crack with a 0º tip angle has a concentration factor that tends to infinite, which is a problem because there is no differentiation of microscopical cracks, since, for instance, a 8mm crack has the same concentration factor as a 4mm crack.

In 1939, Westergaard successfully developed an exact solution for the stress field surrounding a crack, although his formulation was difficult to apply [11]. Later, in 1957, G. R. Irwin reached similar results, essentially determining that stress quickly drops as the distance to the crack tip increases [12]. This trend can be seen in Figure 7. The difference was Irwin's formulation was simpler because it was applicable to a smaller region, closer to the crack tip. Based on this, Irwin discovered the Stress Intensity Factor (SIF or K) and established Equation (2). The stress intensity factor, K, is a geometric parameter that characterizes the stress field near a crack tip, which is given by Equation (2):

$$\sigma = \frac{K}{\sqrt{\pi a}} \tag{2}$$

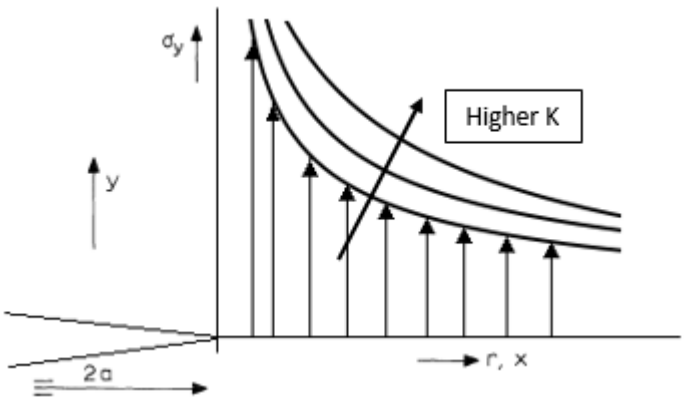

Figure 7 - Stress near a crack tip, adapted from [13].

Equation (3) is a restrictive version of Equation (2) accounting for critical conditions.

$$\sigma_c = \frac{K_c}{\sqrt{\pi a}} \tag{3}$$

The Stress Intensity Factor is a useful tool for predicting fracture in metals, but when it comes to adhesives there is considerable disagreement as to how the stress intensity factor should be calculated [14], and as such, an energetic approach is preferred. The energetic criterion commonly used in adhesives was first considered by Griffiths in 1920 [15], which describes a way to predict cracks based on the "theorem of minimum potential energy". According to it, it is possible to predict when an elastic solid is going to fracture if the energetic effect that comes from the formation of crack surface is accounted for.

Broek's interpretation of this phenomenon is that crack growth can occur if the energy required to form an additional crack of length *da* is matched by the energy created in the material as consequence of the reference stress [13]. As cracking occurs, there is a relaxation of tensions and balance is reestablished. This means that when a material fractures, an area relieved from stress is created, such that the force that used to exist in that area between the material's particles no longer exists: the atomic bond energy that used to hold the material together ultimately can no longer support the stresses and the material fractures, forming a certain crack surface area. Figure 8 shows a schematic of this phenomenon.

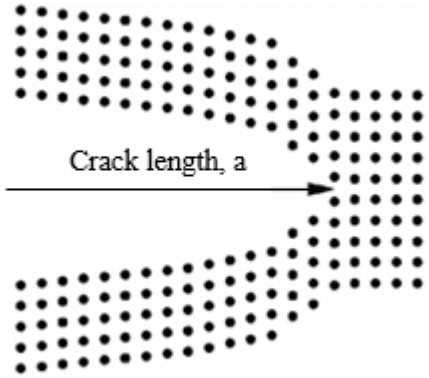

Figure 8 - A crack from an atomic standpoint [16].

The energy required to separate material's particles is called Energy Release Rate G, which according to Griffith, is defined by Equation (4):

$$G = \frac{\partial U}{\partial a} \tag{4}$$

U being the total internal energy, and a the crack length. Another representation for G is the Irwin-Kies's developed Equation (5):

$$G = \frac{P^2}{2B}\frac{dC}{da} \tag{5}$$

Where B is the specimen width, P is the load and C, the compliance is given by Equation (6):

$$C = \frac{\delta}{P} \tag{6}$$

Using Equation (5), it is possible to determine energy release rate in any mode [3]. Each material has a characteristic critical energy release rate, this value is different for each loading mode, shown in Figure 9.

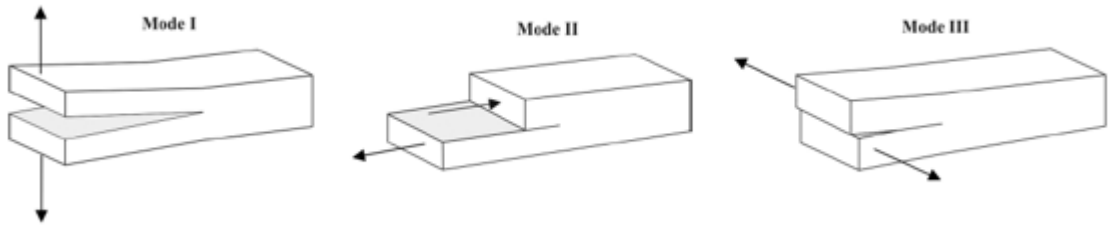

Figure 9 - Pure loading modes: mode I is an opening mode, and mode II and III are shear modes [9].

Mode I is an opening mode, while mode II and III are shear modes, mode II is loaded parallel to the crack progression direction and mode III is loaded perpendicular to the crack progression direction. In most real applications the loading mode is mixed, which means that it is not a pure mode but a combination of two or three modes.

It is important to note that both the Stress Intensity Factor, K, and Energy Release Rate, G, are physical quantities used to characterize fracture in materials and that these quantities are related, which for a plane stress state, the relation is given by Equation (7):

$$G = \frac{K^2}{E} \tag{7}$$

And for a plane strain state by Equation (8),

$$G = \frac{K^2(1-\nu^2)}{E} \tag{8}$$

E, being the Young's modulus and ν, the Poisson's ratio.

2.2.3 Damage mechanics

Damage mechanics is a theory that combines continuum mechanics and fracture mechanics to predict all stages of failure: initiation and propagation of cracks, and fracture of materials, without using microscopic characterization. In this approach, both strength and energy parameters are used, where continuum mechanics tools are used to predict damage initiation and fracture mechanics tools are used to describe crack propagation.

2.3 Numerical approach

The most common numerical approaches to model fracture are based in damage mechanics, namely, cohesive damage models and continuum damage models.

2.3.1 Cohesive damage model

A cohesive zone model (CZM) is a model in which fracture formation is gradual where surfaces separate as the cohesive elements are destroyed. Crack initiation and crack propagation can be predicted using cohesive elements without setting a pre-crack. However, it is required to know where the critical areas are [9]. This disadvantage is less important when it comes to modeling fracture tests since the critical region will be the adhesive layer since the adherends are many times the thickness of the adhesive layer.

Continuum damage models are based in continuum mechanics, where the failure criteria is based in maximum stresses and maximum deformations. Similarly to what happens with continuum mechanics, using a continuum damage model can lead to singularities, where stresses tend to be infinite [8]. Example of singularities points can be seen in Figure 6.

An advantage of using continuum damage models is being able to correctly simulate variations of adhesive layer thickness. There is a region near the crack tip called the fracture process zone (FPZ), the FPZ varies according to the adhesive layer thickness [17]. Figure 10 is a schematic representation showing the influence of thickness on the FPZ: the specimen shown in Figure 10a is thinner, thus exhibiting a longer FPZ, while in Figure 10b the thickness is higher, increasing the FPZ area.

a) b)

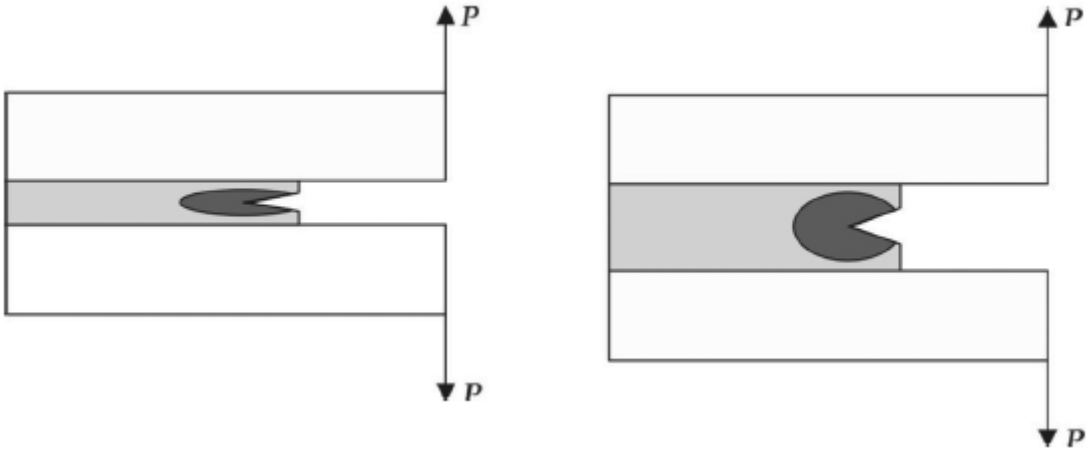

Figure 10 - Effect of thickness in the fracture process zone [9]: a) lower thickness, b) greater thickness.

In a CZM, stress criteria is combined with facture mechanics data making it possible to determine crack initiation and growth. In 1959, Barenblatt [18] was the first to introduce a CZM based on Griffith's theory of fracture, albeit it was only implemented in finite elements modeling by Hillerborg et al. in 1976 [19], establishing the relation between traction and the displacement, which is also known as the law of traction-separation (Figure 11).

Two distinct phases can be seen in the traction-separation law, characterizing the material in different conditions, the first is an elastic stage where no damage occurs. If the maximum stress is reached, damage initiation will take place, which corresponds to the end of the elastic phase.

Traction-separation laws are characterized according to stiffness, stress and fracture energy, and they can present various shapes: triangular (most common), trapezoidal, exponential and others.

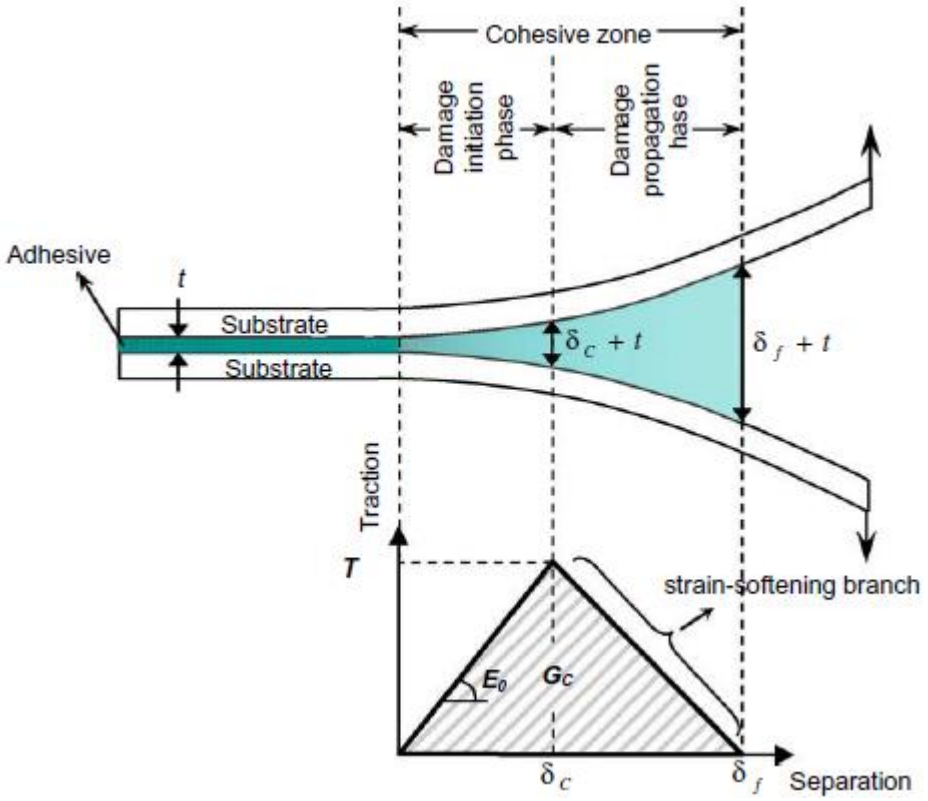

Figure 11 - Schematic comparison between the traction law and the displacement during a test [20].

Displayed in Figure 12, are triangular (Figure 12a) and trapezoidal (Figure 12b) traction-separation laws for a model. Note that two shapes can be seen for each model, one for mode I properties and the other for mode II properties. Depending on the type of adhesive, either a triangular or a trapezoidal law may be more accurate: if the adhesive is ductile, a trapezoidal law is more likely to be appropriate, while if the adhesive is brittle, a triangular law should be more adequate.

a)

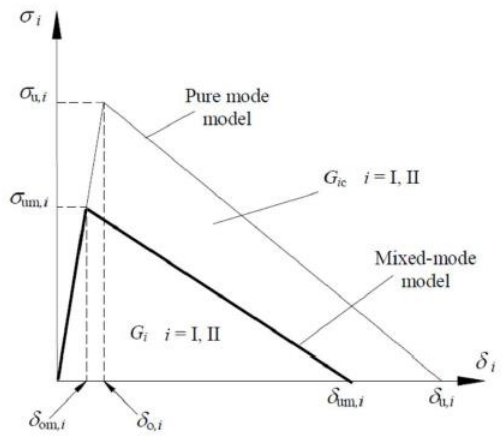

b)

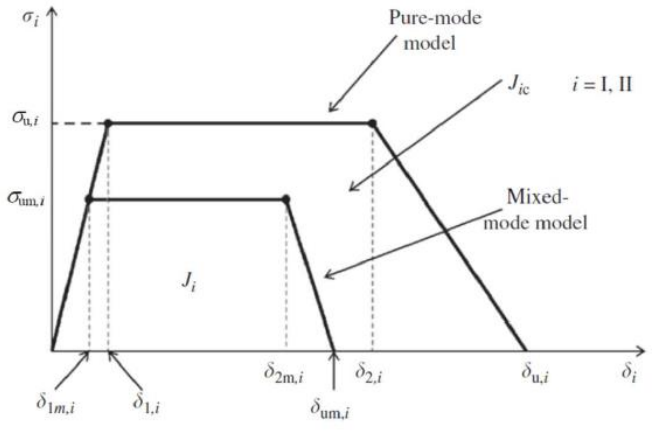

Figure 12 - Adapted from [9]: a) triangular softening law, b) trapezoidal softening law.

2.4 Fracture mechanics tests

Fracture mechanics tests are important tools to evaluate adhesive joints strength. Through the Irwin-Kies equation it is possible to obtain the energy release rate G, characterizing fracture toughness.

By plotting G as a function of the crack length it is possible to obtain a resistance curve (*R-curve*), which represents the energy release rate as a function of the crack length. The value for the critical energy release rate G_c, will be considered when the value of G does not change significantly, thus leading to a plateau, which will correspond to the G_c value [3].

2.4.1 Fracture tests for mode I

The most used test to characterize the mode I fracture toughness is the Double Cantilever Beam (DCB) test. The test is described in standards ASTM D3433 and ISO 25217 for measuring the critical fracture energy in pure mode I (G_{Ic}) [21, 22]. DCB specimens are composed by two adherends bonded with adhesive along their length. In the side where the load is applied, there is an initial length without adhesive layer, called pre-crack a_0, as seen in Figure 13 [2].

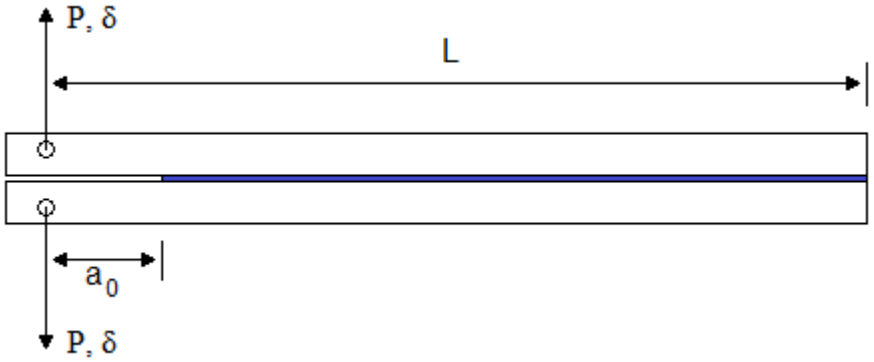

Figure 13 - DCB test scheme.

In accordance with ISO 25217, the specimen is initially loaded at a constant crosshead displacement rate until a small crack occurs [22]. Loading is then stopped, and the specimen is unloaded. This is called the precracking stage, where the crack grows a few millimeters. This stage is important since the initial crack needs more energy to form than stable crack propagation. Due to pre-cracking, an initial peak will be less prominent in the resulting *R*-curve,

making it easier to determine G_{Ic} [23]. After precracking, the specimen is again loaded, this time by opening until failure. The test displacement rate is constant and usually varies between 0.1mm/min and 5mm/min, according to the test geometry and materials. During the procedure, the load P, and the displacement δ, are recorded [24].

Using the CBBM, Equation (9) can be obtained, expressing compliance as a function of the equivalent crack length.

$$C_I = \frac{8a_{eq}^3}{EBh^3} + \frac{12a_{eq}}{5BHG_{13}} \tag{9}$$

G_{Ic} is obtained by deriving the compliance in order to a_{eq}, which is then placed in the Irwin-Kies Equation (5), resulting in the equation for G_{Ic}, using the DCB test, shown in Equation (10):

$$G_{Ic} = \frac{6P^2}{B^2h^3}\left(\frac{2a_{eq}^2}{E_f} + \frac{h^2}{5G_{13}}\right) \tag{10}$$

Where h and B, represent the height and width of each adherend, respectively, and G_{13} the shear modulus. E_f is the flexural modulus, calculated using the measured initial compliance C_0, according to Equation (11):

$$E_f = \left(C_0 - \frac{12(a_0 + |\Delta|)}{5BhG_{13}}\right)^{-1} \frac{8(a_0 + |\Delta|)^3}{Bh^3} \tag{11}$$

Where Δ is a crack length correction accounting for crack tip rotation and deflection defined in Equation (12),

$$\Delta = h\sqrt{\frac{E}{11G_{13}}\left(3 - 2\left[\frac{\Gamma}{1+\Gamma}\right]^2\right)} \tag{12}$$

And

$$\Gamma = 1.18\frac{E}{G_{13}} \tag{13}$$

C_0 is calculated using the C_I equation, given the condition $a_{eq} = a_0$, which is the initial crack that resulted from the precracking stage.

As seen in Figure 14, the FPZ influences the estimation of the equivalent crack length, thus, to prevent errors in the calculations CBBM accounts for the effects of the FPZ, in which $a_{eq} = a + |\Delta| + FPZ$ [25, 26]. The equivalent crack length a_{eq}, is given by Equation (14):

$$a_{eq} = \frac{1}{6\alpha}A - \frac{2\beta}{A} \tag{14}$$

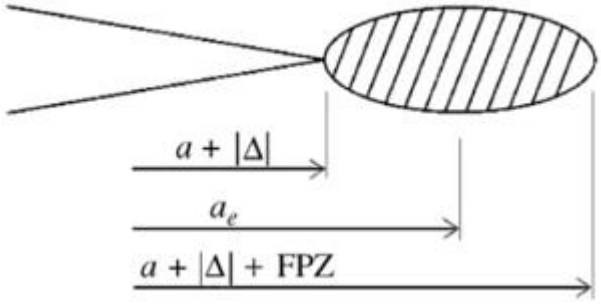

Figure 14 - Schematic representation of the FPZ near the crack tip [8].

Where

$$\alpha = \frac{8}{Bh^3E_f};\ \beta = \frac{12}{5BhG_{13}} \tag{15}$$

And

$$A = \left(\left(1 - 108\gamma + 12\sqrt{\frac{(4\beta^3 + 27\gamma^2 - \alpha}{\alpha}}\right)\alpha^2\right)^{\frac{1}{3}};\ \gamma = -C \tag{16}$$

2.4.2 Fracture tests for mode II

There is no standard for the determination of the fracture toughness in mode II using metal adherends. According to many authors, the End Notched Flexure (ENF) appears to be the most suitable test for fracture characterization in mode II [27], because it is more efficient than other popular mode II tests, facilitating the deduction of a proper data reduction sheet.

The test consists of bending the test specimens inducing shear in the crack tip. A schematic is shown in Figure 15:

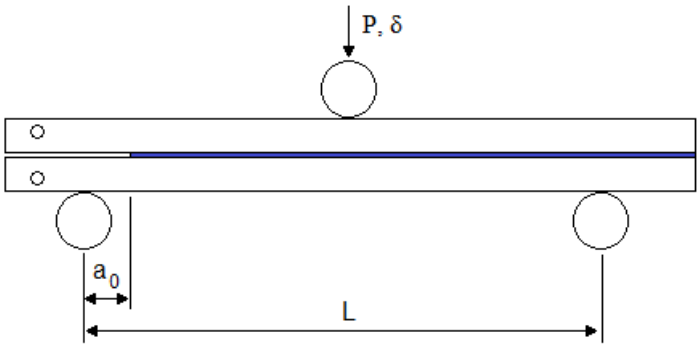

Figure 15 - ENF test schematic.

The ENF test specimen geometry is similar to the one used in the DCB test. As seen in Figure 15, the load is applied in the simply supported beam at mid-length causing the adherends to deform elastically, thus inducing an almost pure shear state at the crack tip [23, 28].

Similarly to the DCB test, the crack length, fracture toughness and compliance for the ENF test are also obtained using the CBBM data reduction scheme, which means crack monitoring is not required during the test.

In the ENF test, G_{IIc} is obtained through a similar process to that of the mode I DCB test. An equation for the compliance as a function of the equivalent crack length is obtained through Equation (17):

$$C_{II} = \frac{3a^3 + 2L^3}{8E_f Bh^3} + \frac{3L}{10G_{13}Bh} \tag{17}$$

The derivative $\frac{\partial C_{II}}{\partial a_{eq}}$ is then placed in Equation (5), resulting in Equation (18), which gives the fracture energy for mode II, for the ENF test:

$$G_{IIc} = \frac{9P^2 a_{eq}^2}{16B^2 E_f h^3} \tag{18}$$

The flexural modulus is calculated using the initial conditions with Equation (19), such as the initial compliance C_0, and the initial crack length a_0:

$$E_f = \frac{3a_0^3 + 2L^3}{8Bh^3 C_{0corr}} \tag{19}$$

Where

$$C_{0corr} = C_0 - \frac{3L}{10G_{13}Bh} \tag{20}$$

2.4.3 Data reduction scheme

The Compliance Based Beam Method (CBBM) determines an equivalent crack length using the information from the experimental test [29]. CBBM is based on the Timoshenko Beam Theory. According to this theory, the internal energy is given by Equation (21):

$$U = 2\left[\int_0^a \frac{{M_f}^2}{2E_1 I}dx + \int_0^a \int_{-h/2}^{h/2} \frac{\tau^2}{2G_{13}} B\, dz\, dx\right] \tag{21}$$

The bending moment M_f, shear stress τ, and the second moment of area of each adherend I, are replaced according to the test setup. These values are dependent of the load P, and the specimens' geometry. According to the Castagliano theorem, the displacement δ, can be obtained by deriving the energy in order to the load, as seen in Equation (22):

$$\delta = \frac{\partial U}{\partial P} \tag{22}$$

This results in an equation for the displacement as a function of the equivalent crack length. According to Equation (6), compliance can be obtained by dividing Equation (22) by the load P, resulting in an equation for the compliance as a function of the crack length. Since the compliance can be calculated throughout the test directly from the load and displacement, rearranging the compliance expression ($C = f(a_{eq})$) can lead to an equation for the equivalent crack length ($a_{eq} = f(C)$) making it possible to use this theoretical equivalent crack length rather than having to monitor crack length. Another particularity inherent to the CBBM is that it accounts for several aspects not included in beam theory, namely the stress concentrations near the crack tip, contact between the specimen's arms and root displacement and rotation effects on the crack tip [27]. The equations for compliance in mode I and mode II were shown in Equation (9) and Equation (17), respectively.

2.4.4 Fracture tests for mixed-mode I+II

Testing adhesive behavior for mixed-mode loadings is very important because in a real application the adhesive joint will be subjected to mixed-mode loadings. Table 1 summarizes some mixed-mode tests.

Table 1 - Mixed-mode fracture tests, adapted from [30].

Test name	Test schematic	Mixed-mode phase angle, φ (°)	Year of the publication
Cracked Lap Shear (CLS)		Fixed, according to the specimen geometry.	1977 [31]
Arcan (left) Modified Arcan (right)		Fixed. Variable, changes according to α.	1980 [32] 2004 [33]
Single Leg Bending (SLB)	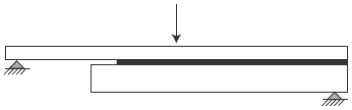	Fixed, according to the specimen geometry.	1990 [34]
Asymmetric Double Cantilever Beam (ADCB)	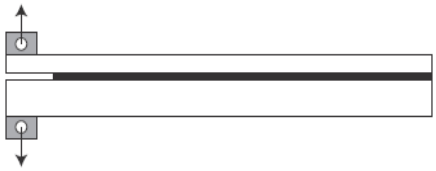	Fixed, according to the adherends' thickness.	1993 [35]
Spelt Loading Jig (SPELT)	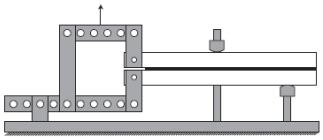	Variable, changes according to the beams setup.	1994 [36]
Asymmetric Tapered Double Cantilever Beam (ATDCB)		Fixed, according to the specimen geometry.	2007 [37]
Mixed Mode Bending (MMB)	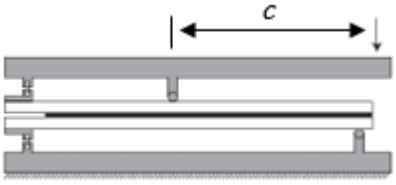	Variable, changes according to the loading arm, c.	2013 [38]

The mixed-mode phase angle φ, is defined by Equation (23):

$$\varphi = tan^{-1}\sqrt{\frac{K_{II}}{K_I}} = tan^{-1}\sqrt{\frac{G_{II}}{G_I}} \begin{cases} \varphi = 0°, & pure\ mode\ I \\ 0° < \varphi < 90°, & mixed\ mode \\ \varphi = 90°, & mode\ II \end{cases} \quad (23)$$

There are many different mixed-mode tests, but most of them require a specific specimen and provide fracture toughness results for only one mixed-mode combination. The Mixed Mode Bending test is the only standard test for mixed mode toughness. This test was proposed and developed for composites, making it inappropriate for stiffer aluminum or steel adherends [9].

To overcome the existing difficulties of measuring mixed-mode fracture toughness, an apparatus was developed by the *ADFeup* group [30]. The proposed apparatus is an evolution of the existent Spelt loading jig [36], with the main difference being that crack length measurement is not needed, instead, two linear variable differential transformer (LVDT) are used to measure displacement. Another difference is that the specimen stays inside of the structure, reducing the overall dimensions of the test setup [39]. The apparatus is presented in Figure 16, note that in Figure 16b, the apparatus is inverted because this machine applies the load from the base.

a) b)

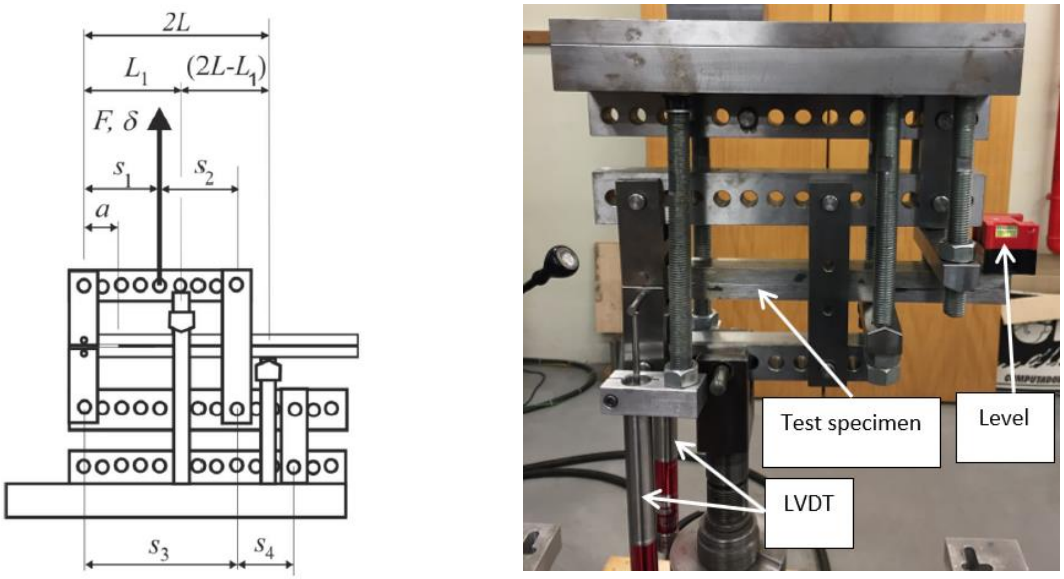

Figure 16 - a) Schematic representation of the apparatus [39], b) photograph of the apparatus.

The apparatus can be configured for multiple phase angles between pure mode I and II by changing the beam lengths (s_1, s_2, s_3 and s_4) of the apparatus.

The phase angle and the forces applied in the top and bottom arm of the specimens change according to the beam lengths. The phase angle can be obtained from the forces applied in the top and bottom arms (see Figure 17) using Equation (24):

$$\varphi_{apparatus} = tan^{-1} \frac{\sqrt{3}\left(\frac{F_1}{F_2} + 1\right)}{2\left(\frac{F_1}{F_2} - 1\right)} \tag{24}$$

The load applied through the apparatus is a combination of mode I and mode II. Figure 17 shows how the apparatus setup can be decomposed, where the mode I component can be viewed as a DCB specimen and the mode II component as a ENF loaded asymmetrically [39].

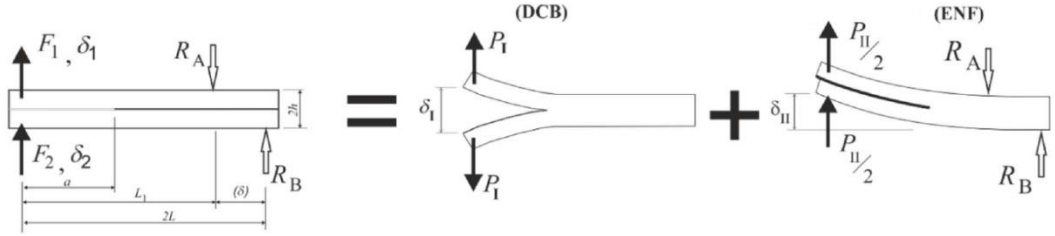

Figure 17 - Specimen loading decomposed [39].

The specimens used in the apparatus for mixed-mode are similar to the ones used in the DCB and ENF tests, making it possible to use only one kind of specimen geometry for all tests. The two LVDT measure the displacement of the top and bottom arm, and the load is registered by the universal test machine. The specimen is placed in the apparatus and fixed through pins inserted in the drilled holes in the specimen in one side, and by contact with the apparatus body in the other (see Figure17).

The load applied by the machine is decomposed in two loads, corresponding to the top and bottom arm's load, F_1 and F_2, respectively (see Figure 16a and 17). The relation is given by Equation (25):

$$F_1 = F\frac{s_1}{s_3};\ \ F_2 = F\frac{s_1 s_4}{s_3(s_3 + s_4)} \tag{25}$$

Using F_1 and F_2 and Equation (26), it is possible to obtain mode I and mode II load components, P_I and P_{II} (Figure 17).

$$P_I = \frac{F_1 - F_2}{2};\ P_{II} = F_1 + F_2 \tag{26}$$

After decomposing the loads, the displacements correspondent of each mode can be obtained from the displacements measured for the top and bottom arms, δ_1 and δ_2, respectively, using Equation (27):

$$\delta_I = \delta_1 - \delta_2;\ \ \delta_{II} = \frac{\delta_1 + \delta_2}{2} \tag{27}$$

Using CBBM, the correspondent compliances for mode I and mode II according to this test setup are given by Equations (28) and (29), respectively:

$$C_I = \frac{\delta_I}{P_I} = \frac{8a^3}{Bh^3E} + \frac{12a}{5BhG} \tag{28}$$

$$C_{II} = \frac{\delta_{II}}{P_{II}} = \frac{8a^3 + 2LL_1^2}{2Bh^3E} + \frac{6LL_1}{5BhG(2L - L_1)} \tag{29}$$

The obtained equation for mixed-mode C_I is equal to the one previously obtained for pure mode I and the equation for mixed-mode C_{II} is equivalent, and equal if $L_1 = L$, which is expected.

Fracture toughness components in mode I and mode II are given by Equations (30) and (31), respectively:

$$G_I = \frac{6P_I^2}{B^2h^3}\left(\frac{a_{eqI}^2}{E_f} + \frac{h^2}{5G_{13}}\right) \tag{30}$$

$$G_{II} = \frac{9P_{II}^2a_{eqII}^2}{16B^2E_fh^3} \tag{31}$$

The same considerations concerning the flexural modulus and crack length correction were applied to the equations above [29].

For the pure modes, the plotted resistance curves allow the determination of G_{Ic} and G_{IIc}. The difference with mixed-mode tests is that the strain energy release rate values are partitioned into mode I and mode II components [26]. It is after obtaining these two components that the

total fracture energy G_T, can be calculated for a given mixed-mode phase angle, according to Equation (32):

$$G_T = G_I + G_{II} \tag{32}$$

2.4.5 Fracture envelope

Fracture envelopes are graphic representations where the strain energy release rate G, is plotted in an x-y axis. The mode I and mode II values correspond to the y and x axis, respectively, and the mixed mode fracture energy is displayed in the quadrant as a two component point, composed by an x coordinate correspondent to the mode II and an y coordinate correspondent of mode I [26], Figure 18 shows an example of a fracture envelope.

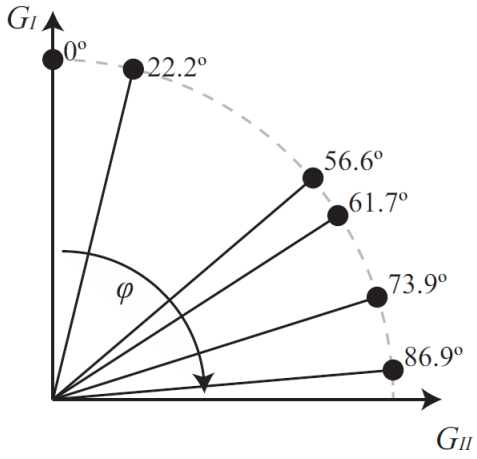

Figure 18 - Example of a fracture envelope [30].

Each scenario shown in Table 2 refers to a different mixed-mode phase angle and through a combined use of Equation (25) and Equation (26), the respective set of beam lengths is displayed, exemplifying how the adjustment of beam lengths changes the mixed-mode phase angle.

Table 2 - Beam length values according to random phase angles [30].

φ (°)	s_1 (mm)	s_2 (mm)	s_3 (mm)	s_4 (mm)
0	60	100	160	-100
22.2	60	100	160	-60
56.6	60	80	140	80
73.9	40	40	80	120
86.9	100	40	140	80

Examples of published fracture envelopes include, for instance, Stamoulis et al. who used the MMB test [40] and within the ADFeup group, da Silva et al. used SLB, ADCB and ATDCB tests [26] to build fracture envelopes, while Costa et al. built one using an apparatus [30].

2.4.6 Fracture envelope criteria

After having the experimental mixed-mode values plotted in an x-y axis, it is sometimes possible to detect a trend for the values obtained. There are essentially two criteria that can be applied using the critical fracture energy for mode I G_{Ic}, and for mode II G_{IIc}: the power law [41], and the Benzeggagh & Kenane law [42]. The power law can fit virtually any curve that does not describe an increase near mode I. The equation used to formulate the envelope is presented in Equation (33). Figure 19 shows the influence of the parameter m on the envelope.

$$\left(\frac{G_I}{G_{Ic}}\right)^m + \left(\frac{G_{II}}{G_{IIc}}\right)^m = 1 \tag{33}$$

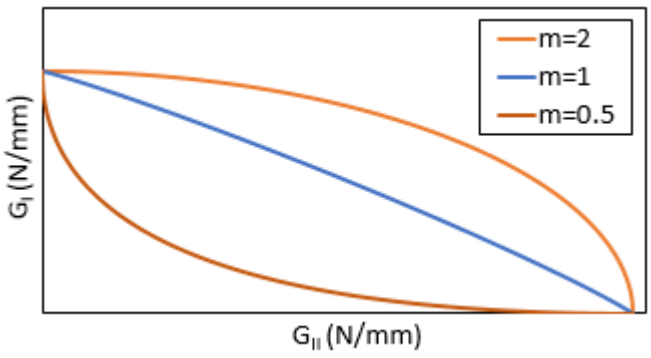

Figure 19 - Power law criterion as a function of the parameter *m*.

This equation can be rearranged to give $G_{II} = f(G_I)$, which means after having each mode's fracture energy component plotted, it is possible build an appropriate envelope by adjusting the parameter m.

The Benzeggagh & Kenane criterion is very efficient to fit envelopes that display an increase near mode I. The equation used to build the envelope is shown in Equation (34), where G_{TC} is the total energy release rate and G_{II}/G_T is the modal ratio.

$$G_{TC} = G_{Ic} + (G_{IIc} - G_{Ic})\left(\frac{G_{II}}{G_T}\right)^m \tag{34}$$

This criterion is especially useful when performing MMB tests, where the modal ratio depends on the geometry of the test setup. The influence of the parameter m is displayed in Figure 20.

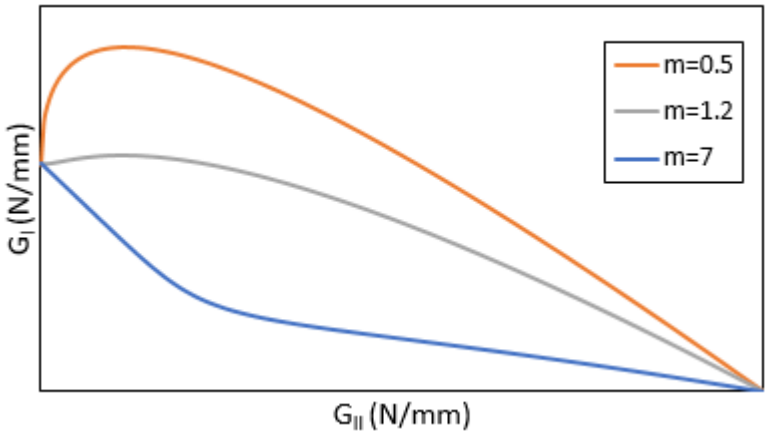

Figure 20 - Benzeggagh & Kenane criterion as function of the parameter *m*.

2.5 Fatigue

Studying how an adhesive behaves over time is of great importance. In fact, fatigue failure is responsible for 80% of failures in service. Fatigue damage is defined as a loss of properties over time due to alternating stresses. Thus, the loads that cause fatigue failure are smaller than those required to cause quasi-static failure [43]. When it comes to fatigue performance, adhesive joints are generally better than the traditional fastening joints due to the fact that they do not exhibit stress concentrations (i.e. drill holes for bolted connections), allowing for a uniform stress distribution, and thus preventing the existence of critical areas. In some cases, adhesive layers can also be combined with conventional fastening joints to improve mechanical behavior [2].

2.5.1 Fatigue load

Fatigue loadings vary within a cycle. The period of one cycle is the time it takes for the load to vary between two adjacent peaks. The frequency f, is the number of cycles that occur per time unit. It is possible to perform tests with varying amplitude and frequency, but normally each experimented specimen is loaded at a constant amplitude and frequency. In most cases, the loading is defined by two parameters, the maximum load P_{max}, and the load ratio R ($R = P_{min}/P_{max}$). The loading can also be described using the minimum load P_{min}, the mean load P_m, or the load range ΔP, since they are all related [2, 43]. Figure 21 shows a schematic representation of a fatigue cycle where some parameters are presented.

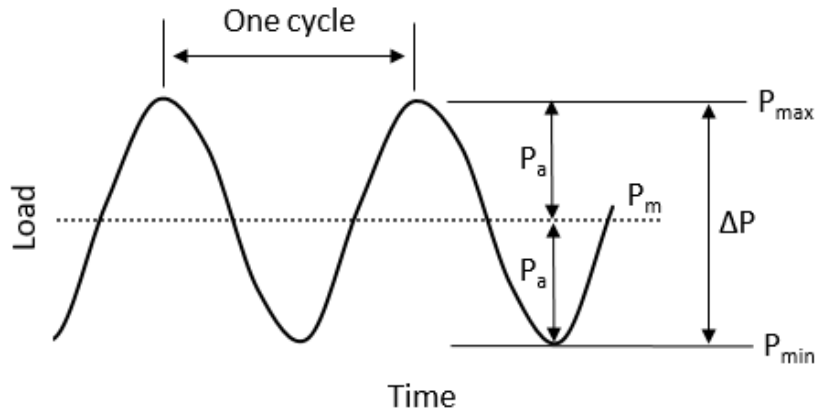

Figure 21 - Example of a fatigue load over time, adapted from [43].

2.5.2 Prediction methods

Studying fatigue induced crack growth is very complex in polymeric materials because many factors influence crack initiation and propagation, such as environmental conditions like humidity and temperature, porosities, lack of homogeneity and insufficient cure, which may be possible factors for fatigue damage, increasing the difficulty of characterizing the crack growth behavior of adhesive joints [44]. Ideally, for each real-life scenario a prototype joint would be tested and have its S-N fatigue curves analyzed (Figure 22a), which would allow to know more accurately what behavior to expect from the specific joint and thus study its safety. As prototyping every joint would require excessive amounts of time and money, instead, adhesive properties are determined using FCG curves to later be used in numerical predictions of the real joint (Figure 22b) [2, 44].

a) b)

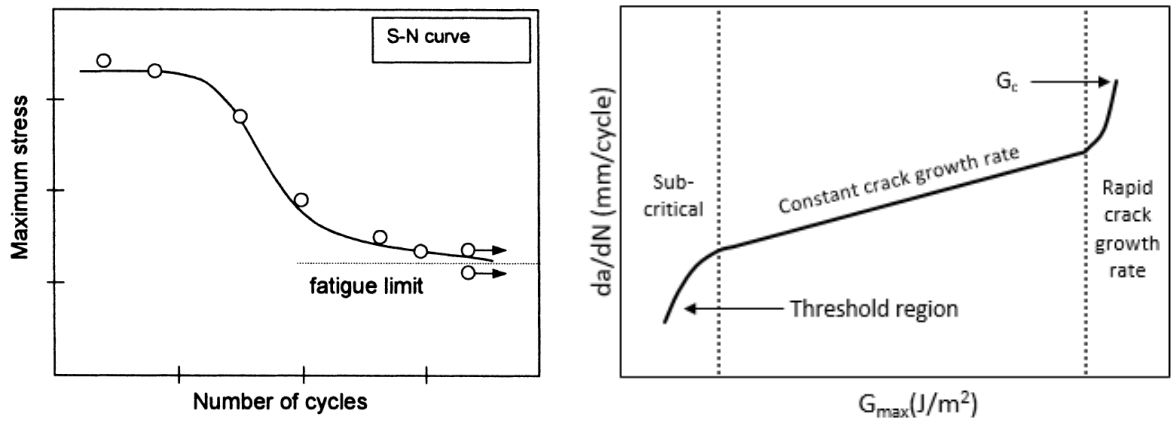

Figure 22 - a) Classical S-N curve [44], b) example of a FCG curve, adapted from [45].

Structural joints, much like all materials, have defects that may become pathways for cracks to propagate if a certain load is applied. The fracture mechanics approach for predicting fatigue behavior is called Fatigue Crack Growth (FCG). This theory assumes the presence of a small crack on a structure under cyclic loading and analyzes its crack propagation [2, 44]. Fatigue crack growth rate da/dN, can be plotted as a function of the strain energy release rate G to create FCG curves. Studies applied to adhesives show that these curves followed the same pattern seen in metals and polymers [14]. Three regions can be distinguished in the FCG graph: a first phase where the crack begins called the subcritical region, a second phase where crack propagation is stable, and a third phase where rapid crack propagation occurs, which is very unstable. It is important to note that FCG theory only applies to the second phase, meaning that the power law relation between strain energy release rate G, and crack growth rate da/dN, exists in this phase only [43, 44]. The relation can be expressed as follows in Equation (35):

$$\frac{da}{dN} = C(G_{max})^m \tag{35}$$

The resemblance to the Paris Law is natural and when plotted in log-log graph it assumes a linear shape. After plotting the experimental data, it is possible to discover an overall equation that approximates the experimental data, values for the Paris Law slope m, and for the y axis intercept C, can be found. The threshold energy release rate G_{th}, and the Paris Law slope m, are key parameters in the FCG curve. Normally, these parameters are used when weighing fatigue damage in the design of adhesive joints [46].

Real joints are mostly under mixed-mode loads and as such, crack propagation is both influenced by mode I and mode II loads. Using the CBBM, one component for each mode is obtained, the total Paris law slope can be calculated using Equation (36):

$$m_T = \sqrt{m_I^2 + m_{II}^2} \tag{36}$$

Studies have been made on how the mixed-mode phase angle affects FCG curves. Differing behaviors were seen, possibly according to the adhesive. One common conclusion being that mixed-mode phase angle greatly affects Paris Law parameters. Figure 23 shows a graphic representation of the envelopes obtained in multiple articles [43, 47-50].

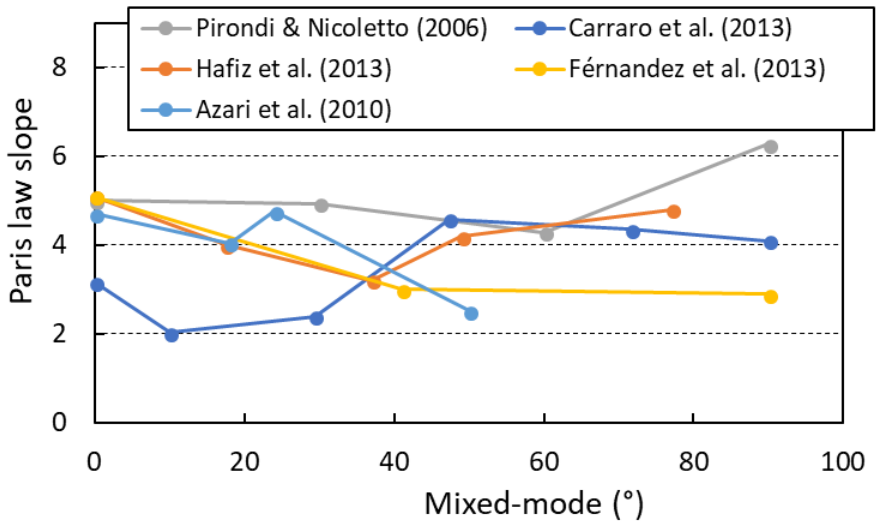

Figure 23 - Paris law slope envelope from multiple published articles [43, 47-50].

2.5.3 Fatigue testing

Fatigue tests allow for the characterization of an adhesive's resistance to cyclic loadings by evaluating both the number of cycles until failure and also the crack propagation behaviour of the material. This is important to understand how the joint will behave under service conditions, since the load amplitudes are under the failure load and multiple load peaks are imposed, similar to what happens in real joints.

Fatigue specimens are the same as the ones used for quasi-static testing. The energy release rate is obtained through the CBBM data reduction scheme, and the equations are equal to the correspondent quasi-static test. Which means Equation (10) can be used to obtain energy release rate in mode I (DCB) tests and Equation (18) displays an expression valid to obtain energy

release rate in mode II (ENF) tests. For mixed-mode testing using the apparatus, two energy release rate components are calculated similarly to static testing, a mode I component and a mode II component can be obtained using Equations (30) and (31), respectively.

The crack growth rate da/dN, is calculated using either the secant method or the incremental polynomial method, as recommended in the ASTM E647 standard [51]. The secant method was chosen since it is the most appropriate approach in crack-opening displacement tests [52]. For a given time interval, the crack growth that took place in this period is divided by the number of cycles that occurred. For two distinct time frames i and $i+1$, crack growth rate is given by Equation (37):

$$\frac{da}{dN} = \frac{a_{eq,i+1} - a_{eq,i}}{N_{i+1} - N_i} \tag{37}$$

3 Experimental details

3.1 Adhesive

The used adhesive was the Teroson EP 5089, a one component commercial epoxy adhesive manufactured by Henkel, a company based in Germany, that is used in the automotive industry. Its main strength is enduring severe environmental conditions such as moisture and extreme temperatures [7]. The adhesive cures at 177°C over 20 minutes.

3.2 Silica glass beads

The adhesive was tested with and without glass beads to test if it had an influence in the adhesive performance since they are used to control the adhesive layer thickness. The beads are made with a common glass, called soda-lime silica glass, manufactured by Potters Beads in the United States of America. The size of the particles varies between 0.25 and 0.35 millimeters, the spheres are 90% round and their density is 2.5 g/cm^3. The particles can endure pressures between 96 MPa and 248 MPa without shattering which is essential since the beads need to endure the adhesive's curing process.

3.3 Adherends

The used adherends were made from DIN 40CrMnMo7 steel. There were two requirements to be met for the chosen steel: a high yield strength so that the adherends do not deform plastically during the tests, and good machinability.

3.4 Specimen geometry

The specimens used for all fracture tests follow standard ASTM D-3433 [21]. This geometry is the standard for DCB tests, while ENF tests and mixed-mode tests using the apparatus are also compatible with the geometry, which is presented in Figure 24:

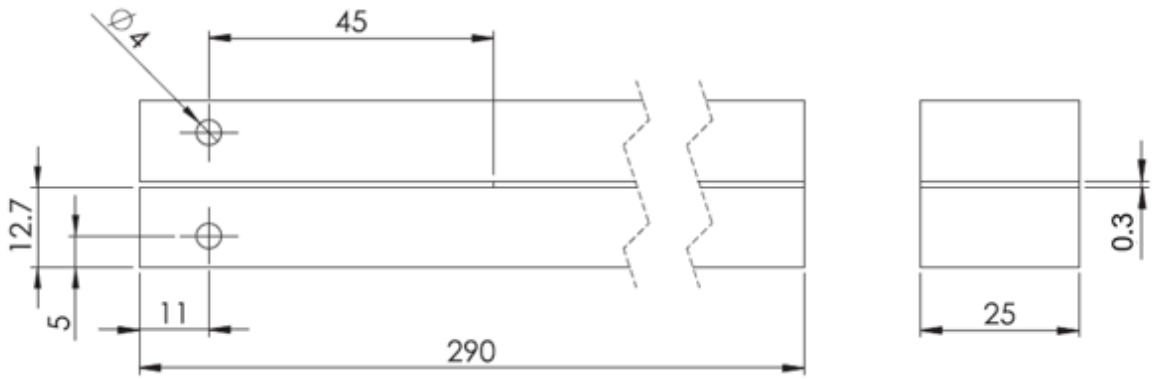

Figure 24 - Specimens' geometry, adapted from [21] (dimensions in millimeters).

3.5 Manufacture of adhesive with glass beads

According to *Deere & Company*, a percentage between 0.5% and 1% of the adhesive weight is used in real applications. According to the literature, this percentage has low impact on the mechanical properties [53], thus a weight percentage of 1% was chosen to guarantee that the thickness is ensured.

The adhesive was first weighed, and then 1% of this weight was added as glass beads particles. After weighing both quantities, particles and adhesive were placed in the same container. At this point the quantities were correct but the mix was not uniform. The container was then placed in a centrifuge at a speed of 3000 rpm for 90 seconds to correctly mix the particles. The adhesive was applied in the specimens or bulk mold with a spatula, as seen in Figure 25a. After evenly spreading the adhesive, the top part of the mold was placed using a basculation technique to prevent air from being trapped inside the adhesive as seen in Figure 25b.

a) b)

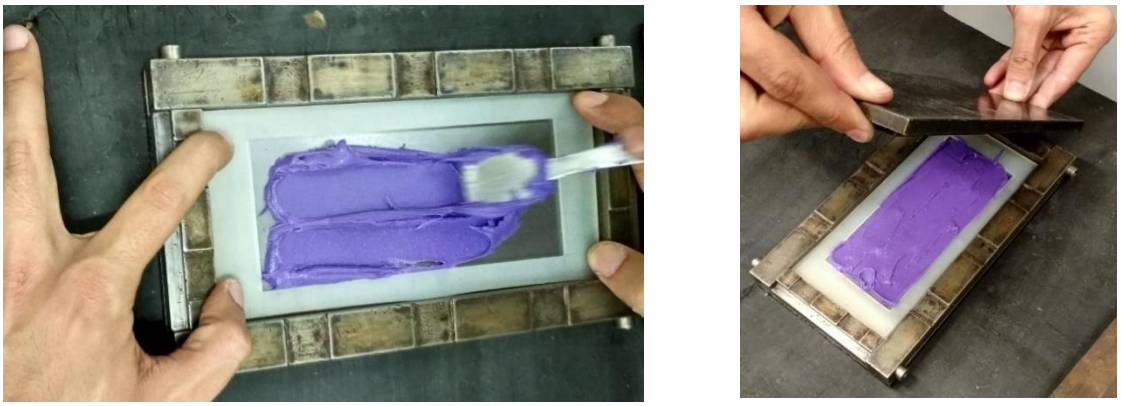

Figure 25 - a) Application of adhesive to a bulk mold, b) closing the bulk sheet mold applying a basculation technique.

3.6 Specimen manufacture

Each specimen surface was sandblasted and degreased with acetone. At the same time, the blades and spacers were brushed with a mold release agent (FREKOTE 770NC) to prevent adhesion to the mold during the cure. The adherends were then placed on the mold between the placement pins and the blades and spacers were placed accordingly over the adherends as seen in a schematic in Figure 26.

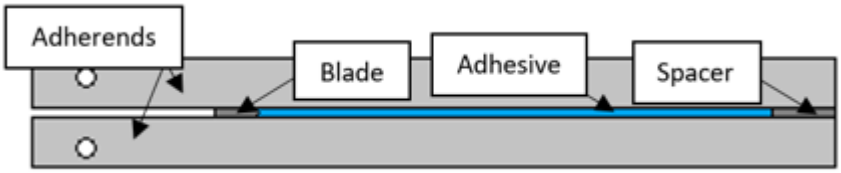

Figure 26 - Side view of the complete specimen.

Figure 27 is a photograph of the mold with the bottom adherends in place, the blades and spacers are in the proper place, which means the adhesive can be applied.

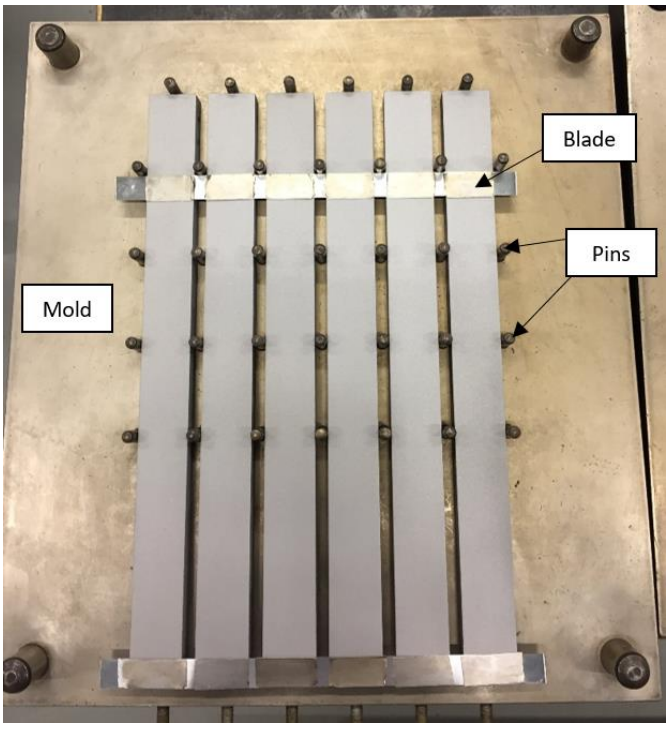

Figure 27 - Specimens in the mold before applying adhesive.

Before applying, the adhesive was placed in the oven for a small period of time, until its temperature was close to 50°C, as recommended by the manufacturer. At the proper

temperature the adhesive was removed from the oven and applied to the adherends' surface. The adherends were then closed by being paired with another adherend on top. The specimens were then placed in a hot plates press to cure for 20 minutes at 177°C. After curing, the specimens' side surfaces were cleaned with sandpaper to prevent the extra adhesive from influencing the results. Finally, the specimens were submitted to precracking to promote stable crack propagation, where they were loaded at a constant crosshead displacement rate of 0.2 mm/minute, until a small crack originated. The loading was then stopped, the razorblade removed, and the new value for the initial crack length was recorded [24].

3.7 Tensile tests

Bulk tensile tests consist on applying a constant displacement rate to a dog bone specimen machined from a bulk adhesive sheet. The stress-strain curves registered throughout the test can be used to determine three properties: Young's modulus E, tensile strength σ_e and strain-to-failure ε_r. Figure 28a shows a representative stress-strain curve for this test, Figure 28b shows a photograph of a tensile test using an extensometer to measure strain.

a) b)

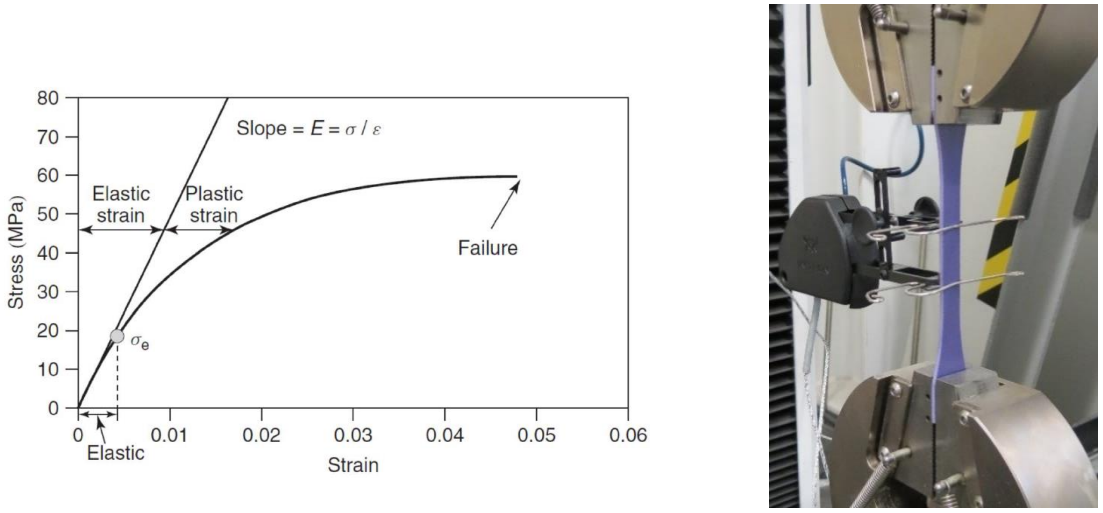

Figure 28 - a) Tensile curve [23], b) tensile test using an extensometer.

To manufacture bulk specimens, a mold is placed in the hot plates press in the same conditions as the DCB specimens, Figure 29 is a photograph of this mold filled with adhesive. The batch displayed in Figure 29 was applied to the mold using a caulk gun directly from the container

since no beads were used. This batch was manufactured using a silicon rubber frame with an opening, so that a thermostat could be used to monitor the actual temperature in the adhesive, ensuring proper cure conditions.

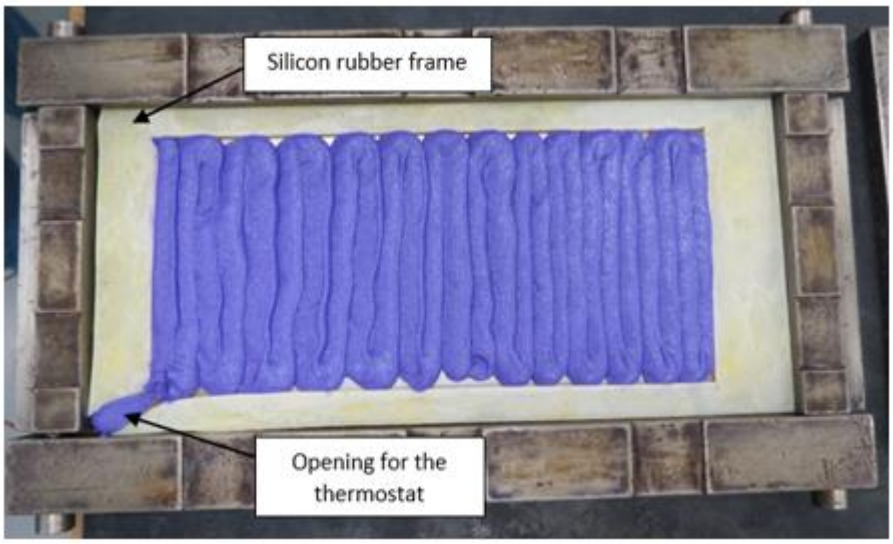

Figure 29 - Bulk sheet mold.

According to the French standard NF T 76-142 [21], a silicon rubber frame was used to keep the adhesive from flowing, guaranteeing thickness and, at the same time, making sure hydrostatic pressure was applied.

Tensile tests were performed to characterize the adhesive's elastic behavior. The results obtained were used as the adhesive properties in the numerical models. The displacement rate was 0.2mm/min, and the strain was measured with the use of an extensometer. The stress was calculated dividing the load by the resistant area, (the thickness of each specimen, was approximately 2 mm, multiplied by the width of smaller cross-section, 10mm). Figure 30 shows a finished bulk tensile specimen.

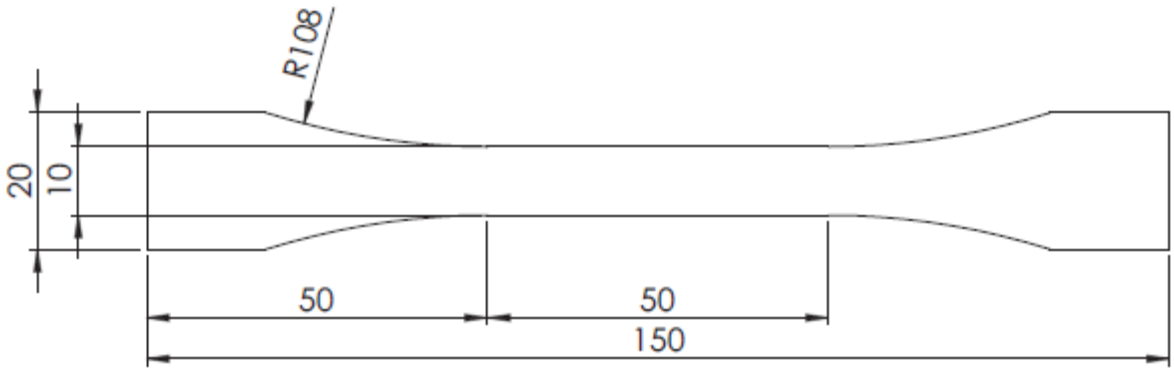

Figure 30 - Geometry of the bulk specimens (ASTM D-638 with dimensions in mm) [22].

3.8 Fracture tests

3.8.1 Mode I tests

DCB tests were completed to assess the adhesive's fracture behavior under pure mode I, allowing for the determination of the critical energy release rate G_{Ic}. A constant displacement rate of 0.2mm/min was used in all tests.

Resistance curves were calculated for each specimen using the CBBM method, which uses the load and displacement values recorded during the test. Equation (12) was used to calculate the value G_{Ic}. Figure 31 shows a DCB specimen being loaded in an universal test machine.

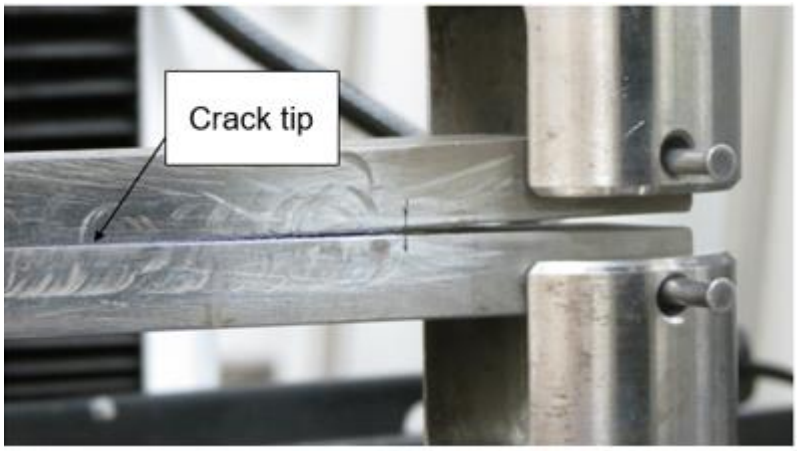

Figure 31 - DCB specimen being loaded.

3.8.2 Mode II tests

ENF tests were performed to define adhesive fracture behavior in mode II, determining critical energy release rate for pure mode II G_{IIc}. The used displacement rate was also 0.2mm/min. Figure 32 shows photographs of an ENF specimen being loaded.

a) b)

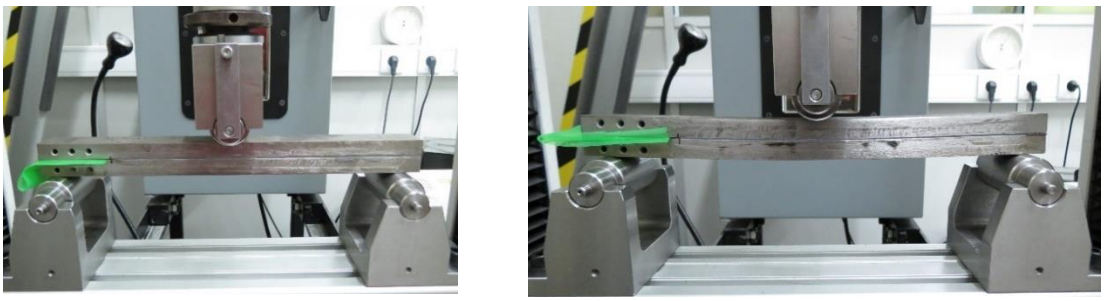

Figure 32 - ENF test setup a) unloaded specimen, b) loaded specimen.

One thing that needs to be considered is that there is friction between the adherends in the cracked side. To reduce friction, a Teflon® sheet with oil was folded and placed in the initial portion of the specimen. The load was applied in the middle of the specimen which also corresponds to the middle of the two support points. The distance between the load point and each support is 130mm. The specimen was centered using a clipper rule to make sure the load was applied symmetrically. G_{IIc} was obtained from resistance curves provided by the CBBM data reduction sheet, using Equation (18).

3.8.3 Mixed-mode fracture tests

Using the mixed-mode apparatus displayed in Figure 33, mixed-mode tests were performed [30, 39]. The tested mixed-mode phase angles were $\varphi = 22.2°$ and $\varphi = 56.6°$.

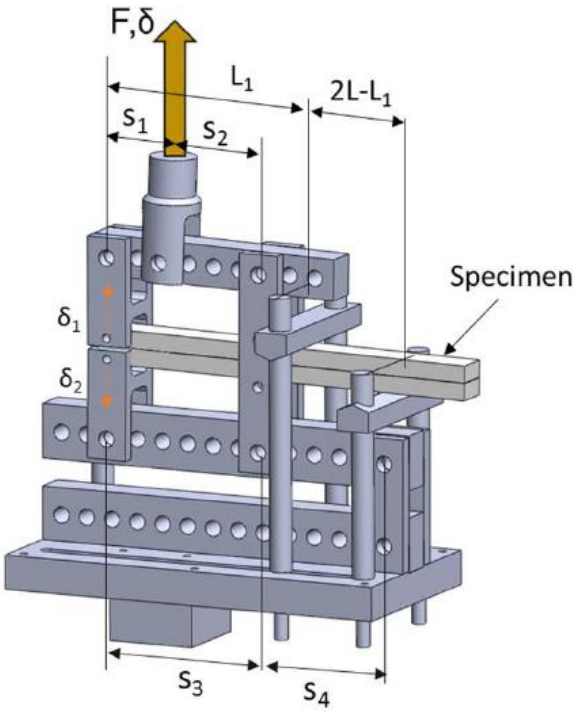

Figure 33 - 3D scheme of the apparatus.

For the tested angles, the beam lengths were set as follows in Table 3:

Table 3 - Apparatus configuration according to the mixed-mode phase angles (φ) tested.

φ (°)	s_1 (mm)	s_2 (mm)	s_3 (mm)	s_4 (mm)	L_1 (mm)	$2L$ (mm)
22.2	60	100	160	-60	205	230
56.6	60	80	140	80	180	230

The displacement rate of 0.2mm/min was maintained for the mixed-mode tests. CBBM was used to obtain two R-curves (one for mode I and one for mode II) using Equations (30) and (31). Two LVDT were used to determine δ_1 and δ_2. The LVDT can be seen in detail in Figure 16b.

3.9 Fatigue tests

To characterize the adhesive fatigue fracture behavior, tests were performed in the same conditions as in quasi-static testing. Namely, the DCB test for pure mode I, the ENF test for pure mode II and, mixed-mode apparatus testing for $\varphi = 22.2°$ and $\varphi = 56.6°$.

Fatigue tests were performed for load percentages of 60% and 80% of the maximum loads obtained in the quasi-static tests. A load ratio of 0.1 was used, meaning P_{min} is 10% of P_{max}. The used frequency was 1Hz as it was the maximum possible frequency so that the machine could apply the correct force in a timely manner.

3.9.1 Mode I tests

DCB tests were performed under fatigue conditions to obtain a FCG curve and determine the Paris law parameters for pure mode I. The setup used was the same as in the quasi-static DCB tests. Table 4 shows a list of the conditions tested.

Table 4 - List of conditions and fatigue parameters for pure mode I.

Tested specimens	Frequency (Hz)	Failure load (N)	P_{max} (N)	P_{min} (N)	Load level (%)
Without beads	1	1800	1080	108	60
			1440	144	80
With beads		1850	1110	111	60
			1480	148	80

During the test, load and displacements were recorded and later analyzed using the CBBM data reduction scheme. Later, FCG curves were obtained using the secant method.

3.9.2 Mode II tests

ENF tests were performed under fatigue conditions to obtain the Paris law parameters for pure mode II. The test setup used was the same as in the quasi-static ENF tests, including the use of Teflon® and oil, for the same reason. Table 5 shows a list of the conditions tested.

Table 5 - List of conditions and fatigue parameters for pure mode II.

Tested specimens	Frequency (Hz)	Failure load (N)	P_{max} (N)	P_{min} (N)	Load level (%)
Without beads	1	16000	9600	960	60
			12800	1280	80

With beads		14500	8700	870	60
			11600	1160	80

Again, the load and displacements were recorded during the test, and later analyzed using the CBBM data reduction scheme. The secant method was used to obtain the FCG curve.

3.9.3 Mixed-mode fatigue tests

After performing fatigue tests for pure mode I and II, mixed-mode tests were performed for the phase angles of 22.2° and 56.6°. The mode I and mode II energy release rates such as the equivalent crack lengths were calculated using CBBM. Fatigue crack growth curves as function of the energy release rate were calculated using the secant method. Table 6 shows the conditions tested for φ=22.2° and Table 7 shows the conditions for φ=56.6°.

In these tests, similarly to the mixed-mode fracture tests, the load and the displacements, given by both the LVDT, were registered during the test. Using CBBM, mode I and mode II components for energy release rate and equivalent crack length were determined during the test. Using the secant method, energy release rate was related to crack growth rate and FCG curves were determined for each component.

Table 6 - List of conditions and fatigue parameters for mixed-mode, φ=22.2°.

Tested specimens	Frequency (Hz)	Failure load (N)	P_{max} (N)	P_{min} (N)	Load level (%)
Without glass beads	1	5000	3000	300	60
			4000	400	80
With glass beads			3000	300	60
			4000	400	80

Table 7 - List of conditions and fatigue parameters for mixed-mode, φ=56.6°.

Tested specimens	Frequency (Hz)	Failure load (N)	P_{max} (N)	P_{min} (N)	Load level (%)
Without glass beads	1	7600	4560	456	60
			6080	608	80
With glass beads			4560	456	60
			6080	608	80

4 Results and discussion

4.1 Tensile tests

Tensile tests were performed to characterize the mechanical bulk properties of the adhesive. The values obtained from this test were later used in the numerical model. Figure 34 shows representative curves:

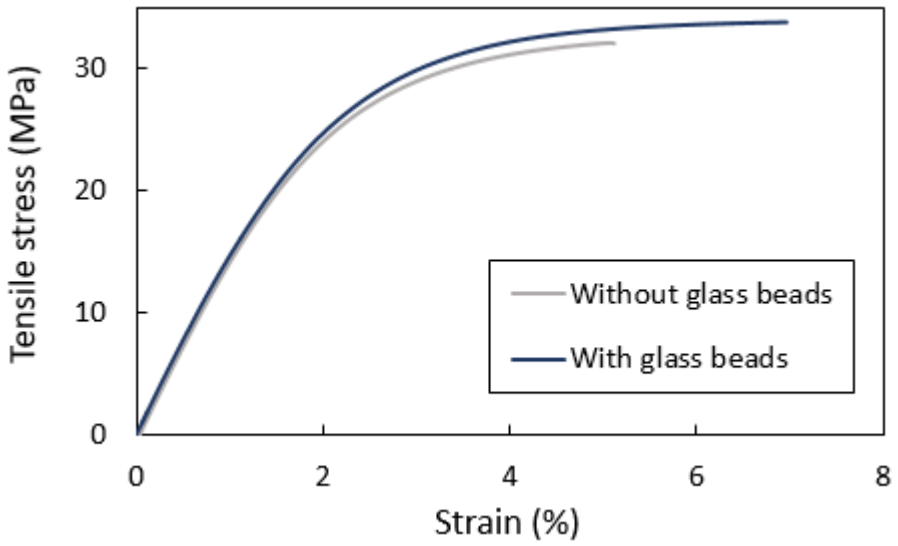

Figure 34 – Tensile curves.

Table 8 shows the results for bulk mechanical properties.

Table 8 - Adhesive properties with and without beads.

	Young's modulus (MPa)	Tensile strength (MPa)	Strain to failure (%)
Without glass beads	1555 ± 43	32.91 ± 0.58	5.96 ± 1.26
With glass beads	1555 ± 142	33.85 ± 0.07	7.23 ± 0.94

According to the literature, the yield strength and Young's modulus of silica filled polymers increases with particulate percentage [54, 55], thus an increase in those properties was expected for our adhesive.

4.2 Fracture tests

4.2.1 Mode I

The DCB tests were performed in quasi-static conditions at a displacement rate of 0.2mm/min and allowed for the determination of the *R-curves* in mode I. The data obtained directly from the test is the $P - \delta$ curve, seen in Figure 35. Initially, the load increases with the displacement, and when the curve hits the peak value, crack growth is eminent. As the displacement increases, crack propagates and the load decreases until the adhesive no longer can keep the adherends together, when the DCB opens in its totality and the load drops to zero.

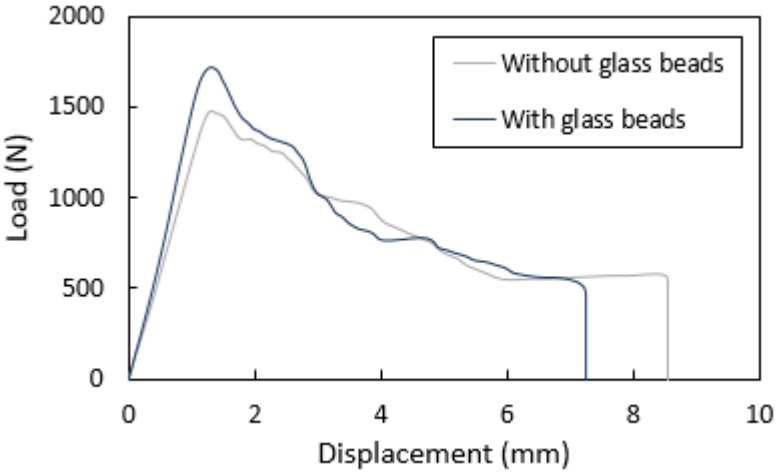

Figure 35 - Load displacement curves obtained from the DCB test.

Using the CBBM, resistance curves were obtained from the loads and displacements, which can be seen in Figure 36.

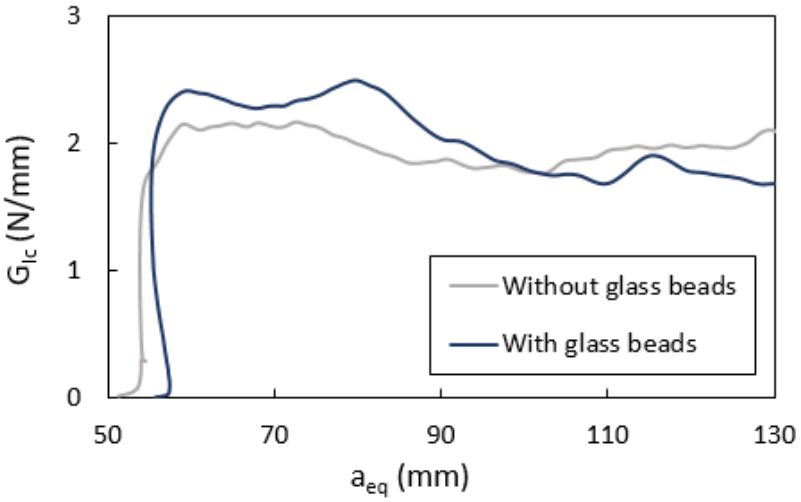

Figure 36 - *R-curves* for mode I according to the DCB test

The energy release rate increases with the equivalent crack length at first, until reaching a plateau. The value of G_{Ic} corresponds to the plateau's energy release rate. After the tests were completed, the debond surface was analyzed and photographed. It was verified that the failure was cohesive in all specimens, as seen in Figure 37.

Figure 37 - Failure surfaces of the tested DCB specimens

Table 9 shows the mode I fracture results.

Table 9 - Critical energy release rate for mode I.

	G_{Ic} (N/mm)
Without glass beads	1.98 ± 0.04
With glass beads	1.89 ± 0.10

4.2.2 Mode II

The ENF tests in quasi-static conditions were also performed at a displacement rate of 0.2mm/min and the *R-curves* for mode II were determined from the load-displacement registered during the test using the CBBM.

The load-displacement curves can be seen in Figure 38. Initially, the load increases with the displacement until reaching a peak, from this point on crack growth occurs. The tested adhesive is considered ductile, which explains the progressive decrease in load after the peak. For a brittle adhesive, a sudden drop would be expected.

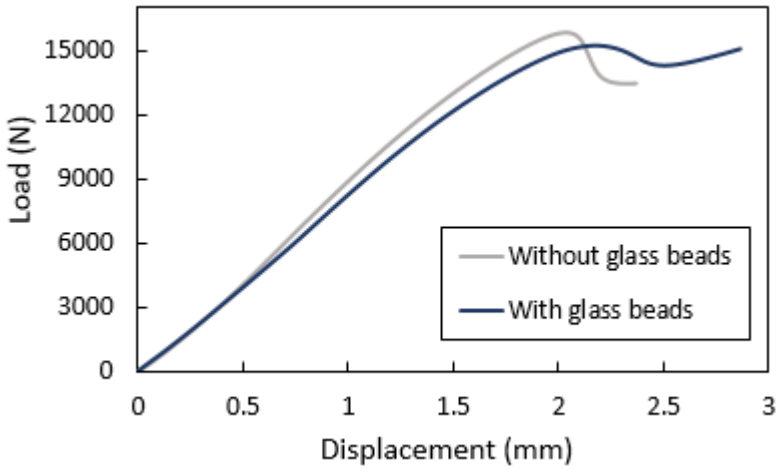

Figure 38 - Load-displacement curve obtained from the ENF test.

The resistance curves for the ENF test are presented in Figure 39. The energy release rate value increases with the equivalent crack length. The plateau is not very pronounced for this adhesive because of its ductility, thus the critical energy release rate values were determined as the average G value for the slope inflexion region. This slope inflexion region corresponds to an equivalent crack length of between 80 and 90mm, approximately.

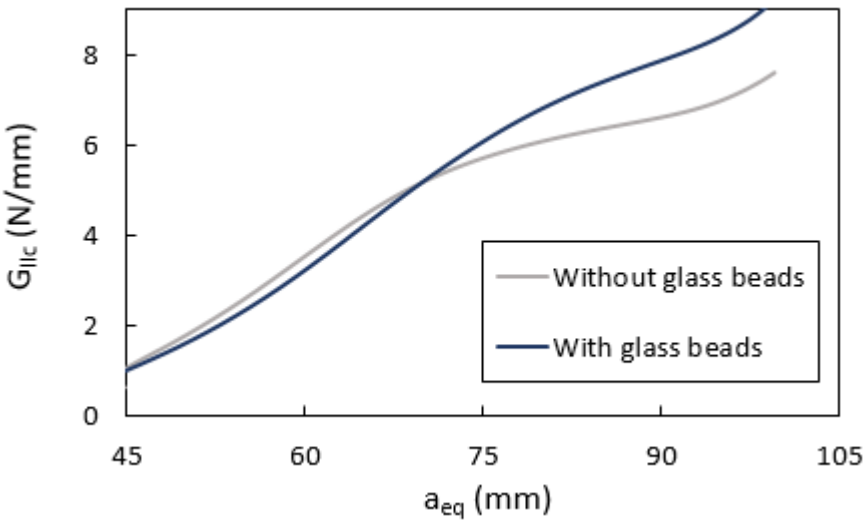

Figure 39 - Representative *r-curves* for the ENF test.

All resulting failure surfaces were cohesive, as seen in Figure 40.

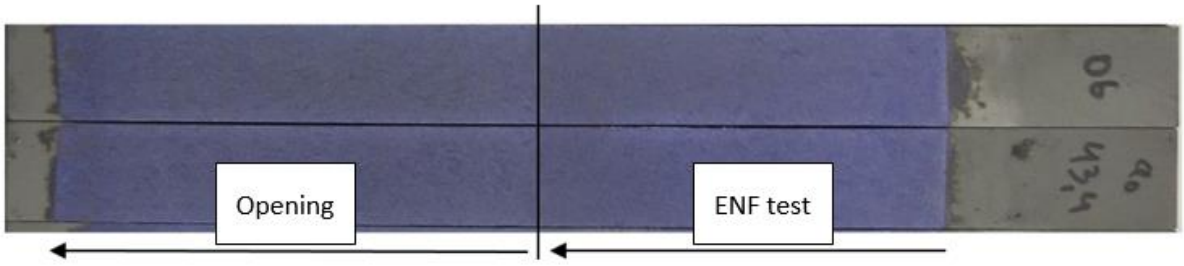

Figure 40 - ENF specimen's surface.

The failure surface correspondent to the loading of the ENF test is signaled on Figure 40 as "ENF test". After the test, since crack length should extend to about half of the specimen's length, the specimen is opened so that the fracture surface can be analyzed. This crack length is signaled as "Opening".

Table 10 shows the mode II fracture results.

Table 10 - Critical energy release rate values for mode II.

	G_{IIc} (N/mm)
Without glass beads	7.84 ± 0.92
With glass beads	7.44 ± 0.62

4.2.3 Mixed-mode I+II (φ=22.2°)

Fracture energy in mixed-mode was determined using the in-house developed apparatus. The load applied was decomposed in mode I and mode II using the procedure shown on chapter 2.4.4. Two LDVT were used to determine the mode I and mode II displacements, shown in Figure 41.

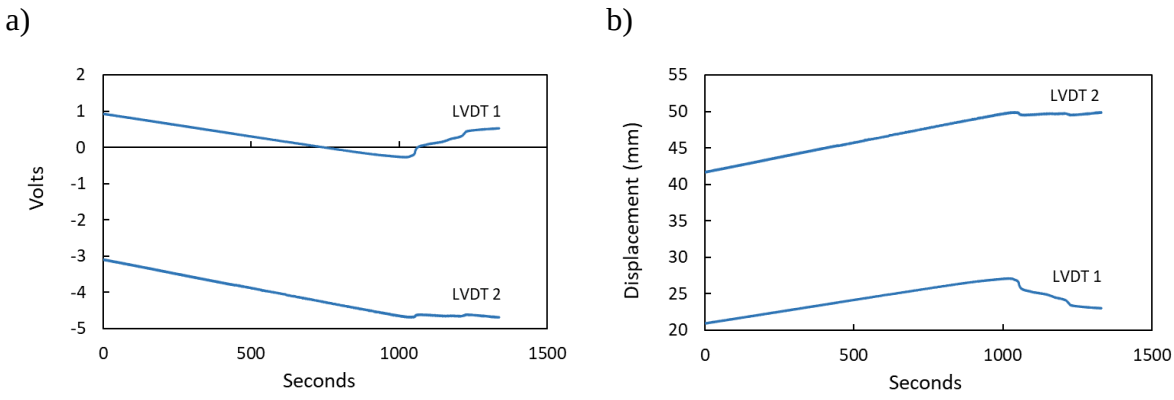

Figure 41 - a) Voltage measured by the two LVDT, b) respective δ measurements obtained from the voltage.

A mixed-mode angle of 22.2° presents a mixed-mode condition close to mode I, this means that the applied load is mainly of this type while at the same time having a small mode II contribution. Figure 42 shows the separated mode I component.

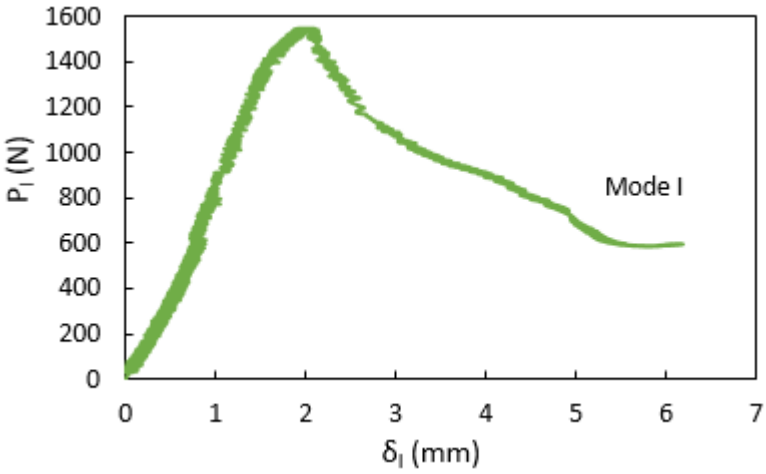

Figure 42 - Load-displacement curve for the mode I component.

The *R-curves* were obtained using the CBBM. Figure 43 displays the obtained results from the mixed-mode tests performed, where φ=22.2°. The mode I curve initially increases to its highest value and later stabilizes at a slightly lower value, this value of G, corresponding to the stabilization of the curve gives the mode I component. As for the mode II component, the value of G was given by the highest value, since its at this point that it seems more stable.

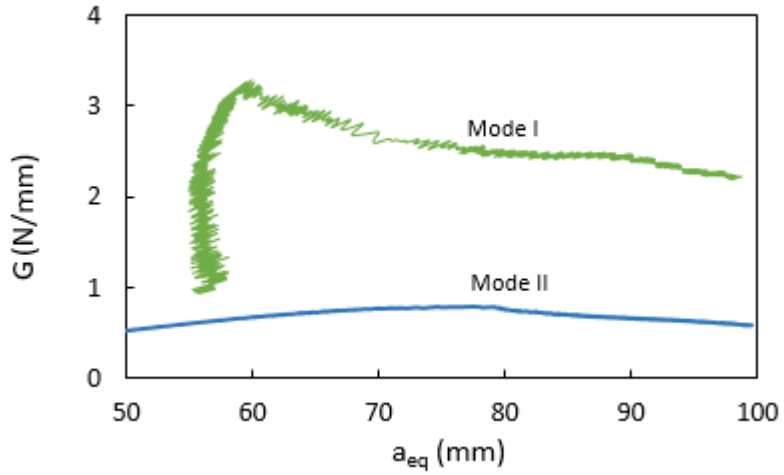

Figure 43 - Resistance curves correspondent of mode I and mode II, φ=22.2°.

It was seen that the fracture energy for mode I is higher than the fracture energy for mode II. This result was expected given the proximity of the phase angle to pure mode I.

Table 11 shows the resulting energy release rates for the phase angle of 22.2°. The effective mixed-mode angle was also assessed using the obtainedG_I and G_{II}, which were higher than 22.2° for every specimen, this might be due to the positioning of the specimens in the apparatus since the optimal theoretical position is not achieved when actually testing.

Table 11 - Fracture energies for the mixed-mode angle, $\varphi_{apparatus}$=22.2°.

$\varphi_{apparatus}$ (°)	G_I (N/mm)	G_{II} (N/mm)	G_T (N/mm)	$\varphi_{effective}$ (°)
22.2	2.40 ± 0.10	0.69 ± 0.09	3.09 ± 0.19	28.11 ± 0.99

As seen in Table 11, results are not separated according to having beads or not, thus the results include both types of specimens. This is because two specimens of each type where firstly tested to determine maximum loads to use in fatigue tests, and while the initial plan was to test more specimens after finishing fatigue testing, it was seen that the results did not appear to be dependent of the particles' weight percentage. For this reason, mean values were calculated with these four specimens, achieving the results seen above. Given the obtained standard deviation, it was considered that the particles had no influence in the fracture toughness, and thus no distinction between specimens was considered.

4.2.4 Mixed-mode I+II (φ=56.6°)

Fracture energies were calculated using the same methodology used for the phase angle φ=22.2°. To test the different mixed-mode phase angle (φ=56.6°) only the placement of the beams in the apparatus was changed.

Figure 44a shows the raw LVDT signal, measured in volts. Using the appropriate conversion for this LVDT model, the displacement of each adherend's arm can be obtained (Figure 44b).

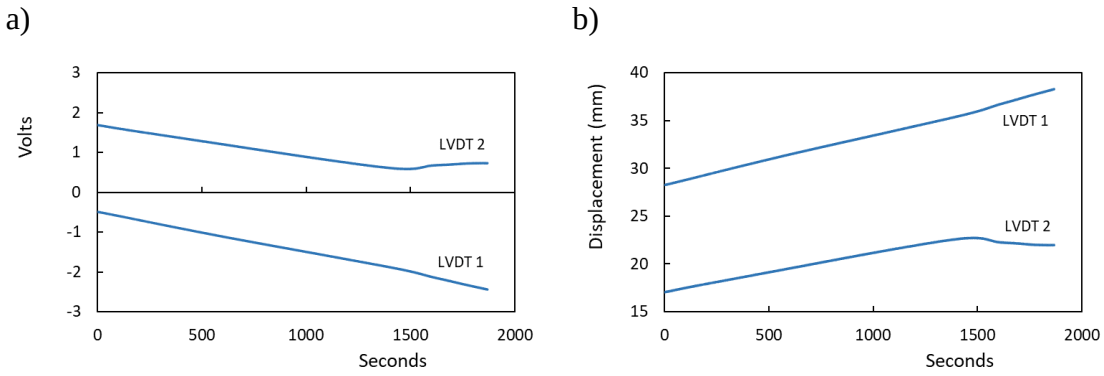

Figure 44 - a) Voltage measured by the two LVDT, b) respective δ measurements obtained from the voltage.

In Figure 45, load-displacement curves for each mode are shown.

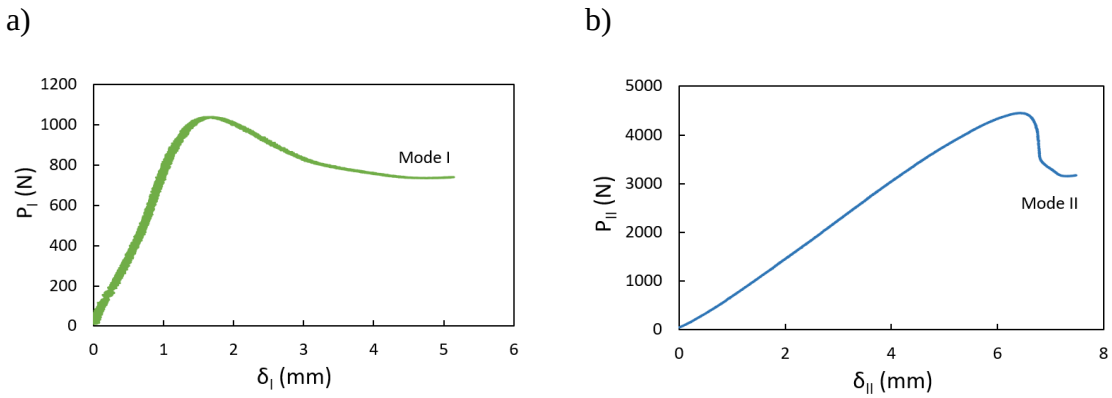

Figure 45 - Load-displacement curves for each mode, a) mode I, b) mode II.

Note that both curves visually resemble the respective pure mode curve. One evident difference between mode I component curve and pure mode I is having no load drop in the final part, which is because DCB tests are performed until complete opening, something impossible to replicate when using the apparatus. This resemblance does not extend to actual values for rigidity, maximum load or displacement, which is expected because these are influenced by the mixed-mode phase angle setup tested.

Finally, as seen in Figure 46, resistance curves were plotted showing how the energy release rate (G_I and G_{II}) changes with equivalent crack increment for each mode (a_{eqI} and a_{eqII}).

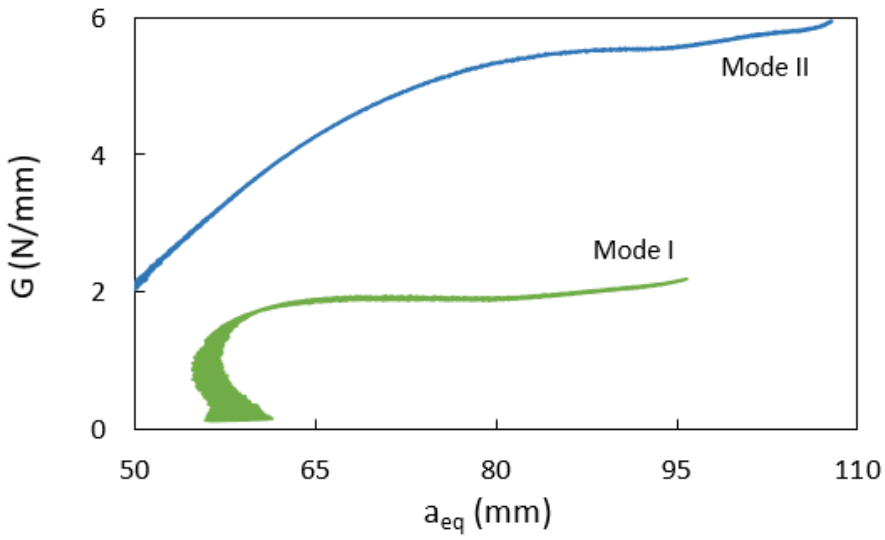

Figure 46 - Resistance curves correspondent of mode I and mode II, φ=56.6°.

This result was within the expected since both components were lower than the respective value obtained for the pure modes (DCB and ENF tests). With a phase angle of 56.6°, it is expected that both components contribute with significant weight to the total fracture energy, which was verified. Also, given that adhesives behave better with shear loads, it is normal that the mode II component is visibly higher.

The resulting fracture energies are exposed in Table 12, where the mean values are shown.

Table 12 - Fracture energies for the mixed-mode angle, $\varphi_{apparatus}$=56.6°.

$\varphi_{apparatus}$ (°)	G_I (N/mm)	G_{II} (N/mm)	G_T (N/mm)	$\varphi_{effective}$ (°)
56.6	1.81 ± 0.08	5.70 ± 0.08	7.51 ± 0.03	60.60 ± 0.70

4.3 Fracture envelope

An adhesive's critical energy release rate G, changes according to the mixed-mode phase angle φ. Adhesives perform better when loaded in shear due to the resistive area being bigger, meaning critical energy release rate in mode II is higher than in mode I. Studying the fracture envelope of an adhesive will provide information on how an adhesive would behave when loaded at any mixed-mode phase angle. The fracture envelope presented in Figure 47 combines information from both pure mode's fracture tests with information from the mixed-mode fracture tests obtained using the apparatus.

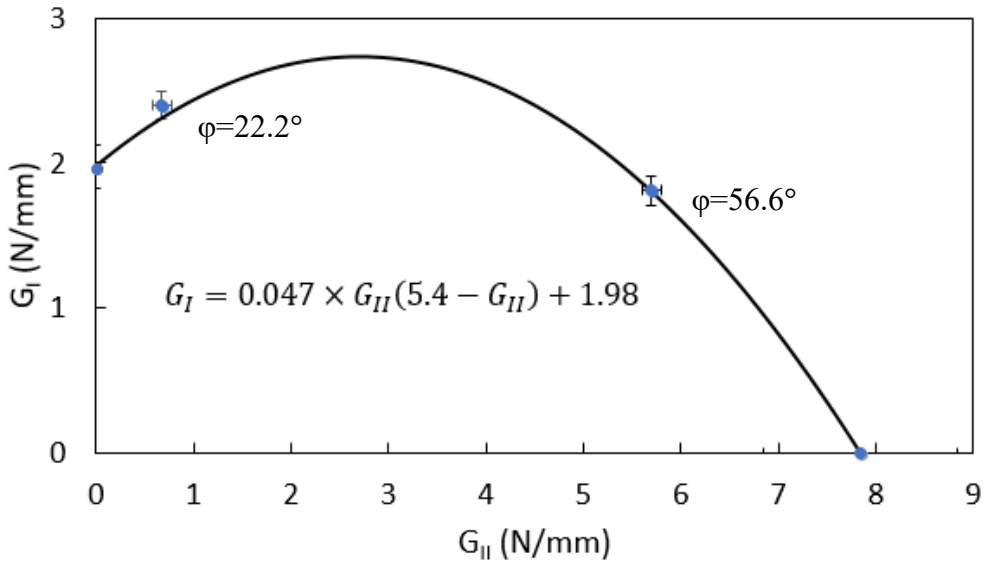

Figure 47 - The obtained fracture envelope for Henkel Teroson EP 5089, using the quadratic criterion.

A quadratic criterion was formulated to achieve the increase near mode I, possible with the Benzeggagh & Kenane criterion and, at the same time, allowing different calculations for the total energy release rate. Equation (38) shows the fundamental equation, which, as the power law, is an equation relating G_I and G_{II}.

$$G_I = A{G_{II}}^2 + BG_{II} + C \tag{38}$$

The scalar values A, B and C can be calculated in terms of G_{Ic} and G_{IIc} by solving the boundary conditions presented in Figure 48.

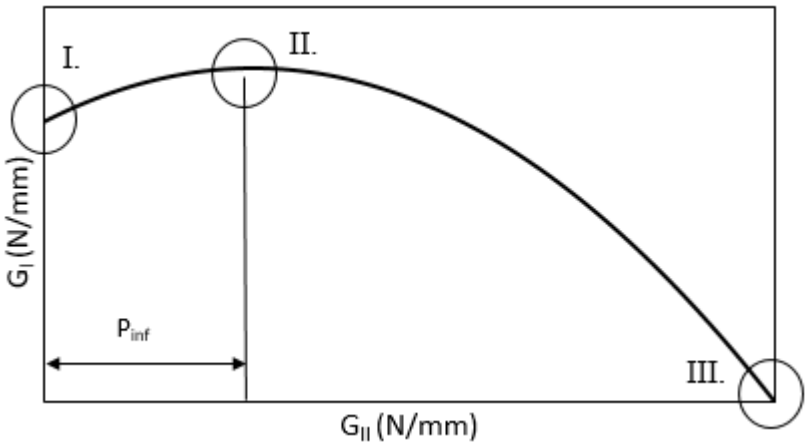

Figure 48 - Boundary conditions used to formulate the quadratic law.

Condition I. implies that when $G_{II} = 0$, $G_I = G_{Ic}$, condition II. implies that the derivative of G_{II} in the point of inflexion is zero, and condition III. implies that when $G_{II} = G_{IIc}$, $G_I = 0$. After simplifying, the set of equations in Equation (39) can be obtained.

$$\begin{cases} C = G_{Ic} \\ B = -2P_{inf} \times A \\ 0 = A \times {G_{IIc}}^2 + B \times G_{IIc} + C \end{cases} \tag{39}$$

The simplified formulation can be seen in Equation (40).

$$G_I = \frac{G_{Ic} \times G_{II}}{G_{IIc}\left(G_{IIc} - 2P_{inf}\right)}\left(2P_{inf} - G_{II}\right) + G_{Ic} \tag{40}$$

By adjusting the value for the point of inflection, which is the parameter in the quadratic law, it is possible to formulate an envelope. Figure 49 shows the influence of the parameter in the envelope.

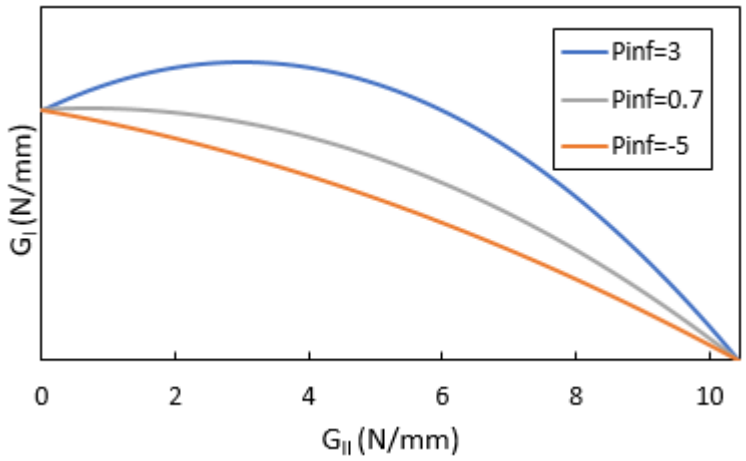

Figure 49 - Quadratic law as function of the parameter P_{inf}.

Both fracture energy values obtained (G_{Ic} and G_{IIc}) are within what is expected for epoxy adhesives. Mode II fracture energies are generally higher than mode I, which was seen when comparing the results for the pure modes and when comparing both components obtained for φ=56.6°. The same did not happen for φ=22.2° because the type of load for this angle was mainly mode I.

The results for φ=22.2° were within the expected since this type of behavior has already been seen in literature. According to the literature, a slight increase near mode I is sometimes visible [40, 56], this behavior was seen when testing for φ=22.2°. According to Costa et al. [56], this may be related to the adhesive's ductility. In the article, three adhesives with different ductilities were tested, where the most ductile adhesive exhibited the greatest increase near mode I, and the least ductile the smallest. Considering that the tested adhesive has a ductile behavior, the increase near mode I was expected.

The results for the mixed-mode phase angle of 56.6° were within the expected, where both mode components reached fracture energies below the respective mode's critical fracture energy. The plotted envelope was obtained assuming a continuous evolution and can be improved if more mixed-mode angles are tested.

Figure 50 shows the different criterions applied to the obtained envelope. While the power law and the Benzeggagh & Kenane criterion can fit one of the mixed-mode values, the quadratic law appears to be a better fit when considering all the values.

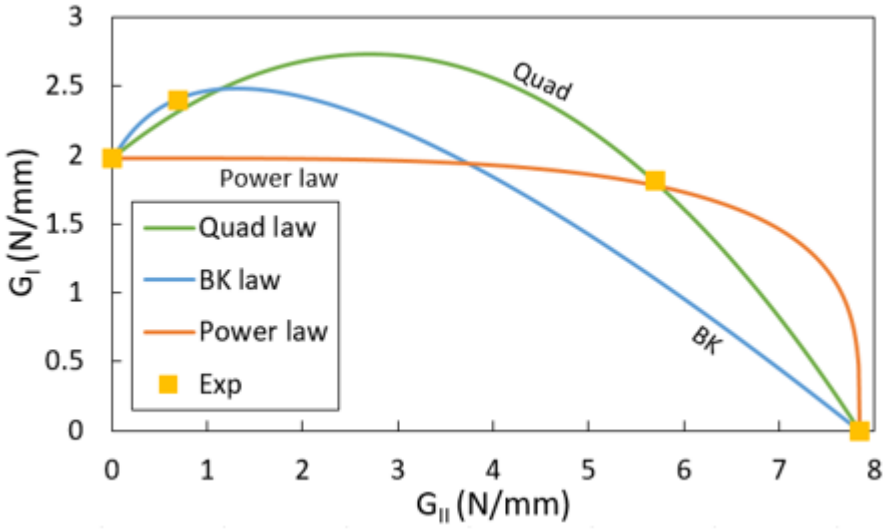

Figure 50 - Multiple criterions applied to the fracture envelope.

4.4 Fatigue

Fatigue tests were performed to assess the FCG behavior. In Figure 51a, the load applied during the test can be seen. The points displayed correspond to the maximum and minimum loads. For the fatigue analysis, only the maximum loads were used because that is when the material is damaged. The graph in Figure 51b shows how the equivalent crack evolves during the test. It was seen that it grows slowly and steadily, until a point when it begins to increase quickly until failure.

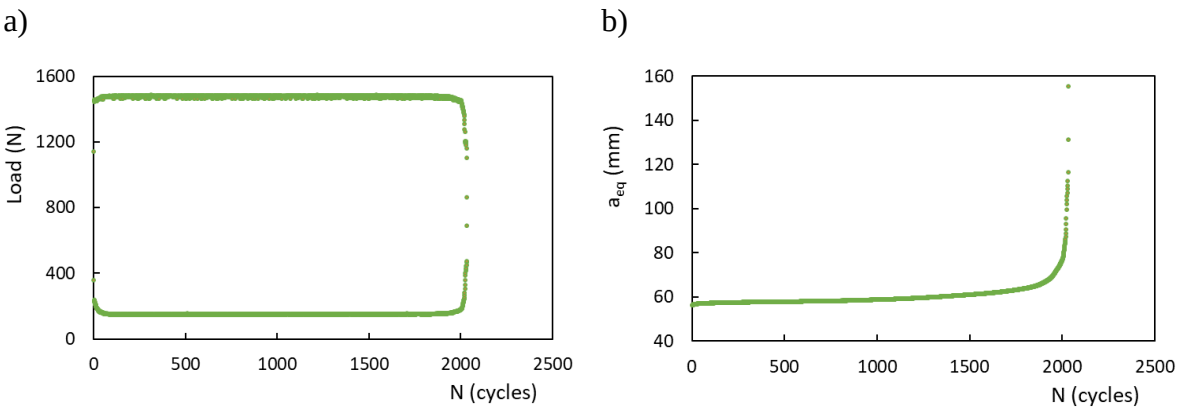

Figure 51 - Data from a DCB fatigue test, a) load variation throughout the cycles, b) equivalent crack length variation throughout cycles.

The energy release rate appears to increase until the end of the test (Figure 52), which is expected because the displacement increases, while the load is constant, leading to an increase in compliance and, consequently, causing G values to increase. As seen in detail in Figure 52, when approaching the critical value, the energy release rate stabilizes. The information presented in Figure 52 refers to an ENF specimen, for DCB tests the variation was similar, where the main difference was the critical energy release rate value.

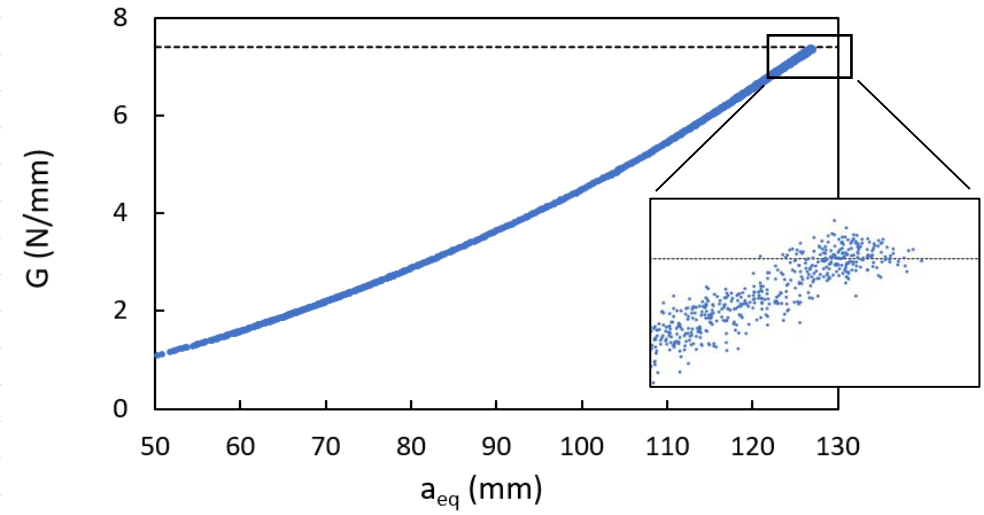

Figure 52 - Energy release rate according to the equivalent crack length.

For each phase angle, the data analysis was divided in two parts: specimens without glass beads, which will be presented first, followed by results for specimens with glass beads. This is so the effects of the beads and the used load percentage can be better understood.

4.4.1 Mode I

To test fatigue in mode I, the specimens were submitted to successive opening cycles at a percentage of the static load. Initially, the applied fatigue load was 80% of the quasi-static failure load, sometimes resulting in tests that would fail quickly, because the load was too close to the fracture load. To make sure the FCG curve would be captured in the test, a load of 60% of the maximum quasi-static load was also tested. Ultimately, results were achieved for both tested load percentages. The resulting 80% FCG curve is displayed in Figure 53.

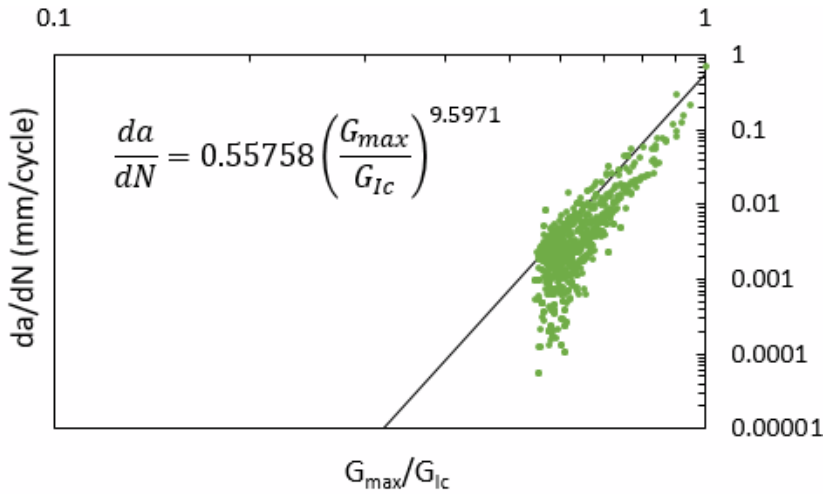

Figure 53 - Overlay of the resulting DCB fatigue crack growth curves for 80% maximum load.

The same testing scheme was followed for the specimens with glass beads and similar FCG curves were obtained. Figure 54 shows a comparison of the obtained Paris law parameters for each tested condition. In Figure 55b, it can be seen that the C value has a high standard deviation, this is because the FCG curve is exponential, and even though some curves might be visually similar plotted in a log-log graph, the C value might differ substantially.

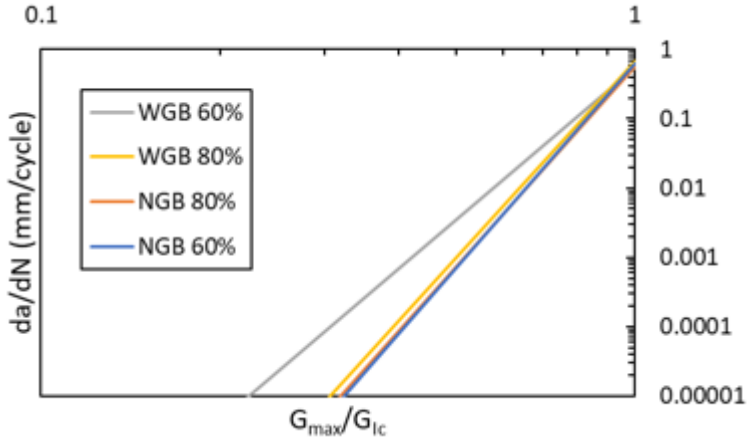

Figure 54 - DCB Paris law trends plotted in the same graph, NGB refers to specimens without glass beads and WGB refers to specimens with glass beads.

Comparing the tests done at 60% and at 80% of the maximum load, it was seen that the Paris law slope (Figure 55a) was not affected by the load increase for specimens without beads, while the specimens with beads displayed a slight increase. The slope obtained for the specimens tested at 60% decreased with the inclusion of beads, this effect was not seen at 80% possibly due to the load being very close to the fracture load, making the presence of beads unnoticed.

The results for the cycles to failure are displayed in Figure 55c, where the effect of the load increase is expected because as distance to the failure load increases, the specimen endures more cycles before failure. Figure 55d displays the threshold energy release rate value, that tends to increase when the load increases, this is expected given that G is directly related to P as seen in Equation (5). This behavior is also seen in the literature, Azari et al. [57] studied threshold behavior for different loads by changing the displacement ratio and obtained similar results.

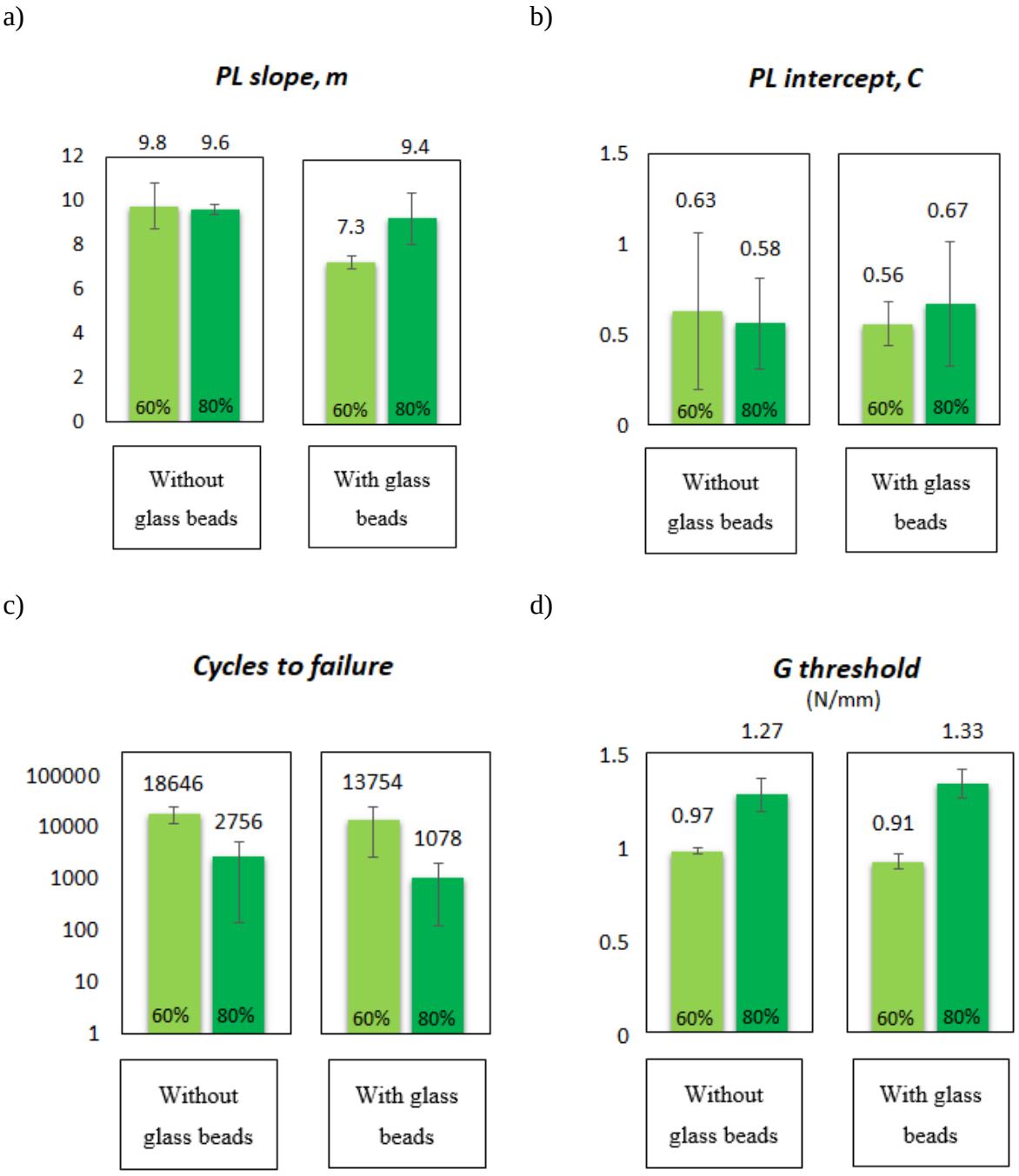

Figure 55 - Fatigue results for mode I, DCB tests, a) Paris law slope results, b) Paris law y-intercept results, c) cycles to failure results, d) G_{th} results.

The results obtained for specimens with beads are very similar to the obtained for specimens without beads. The PL intercept, in Figure 55b, the cycles to failure, in Figure 55c, and the threshold energy release rate, in Figure 55d, are virtually the same. The Paris law slope is slightly lower for 60% compared to 80%, which may be explained by the presence of glass beads, since it is possible that the Paris law slope is affected by crack pinning (when a crack meets an array of particles and slows its progression [54]). It is possible that the same is not

visible for 80% because the load is too high for the beads to make a difference. It is important to note that no difference was evident in the other properties.

4.4.2 Mode II

To test the fatigue behavior in mode II, ENF tests were performed using the CBBM to deduce the energy release rate and equivalent crack length values. The same test scheme used in mode I was followed for mode II tests regarding the load percentages applied.

An example of a FCG curve obtained for the ENF test at 80% of the maximum load is displayed in Figure 56.

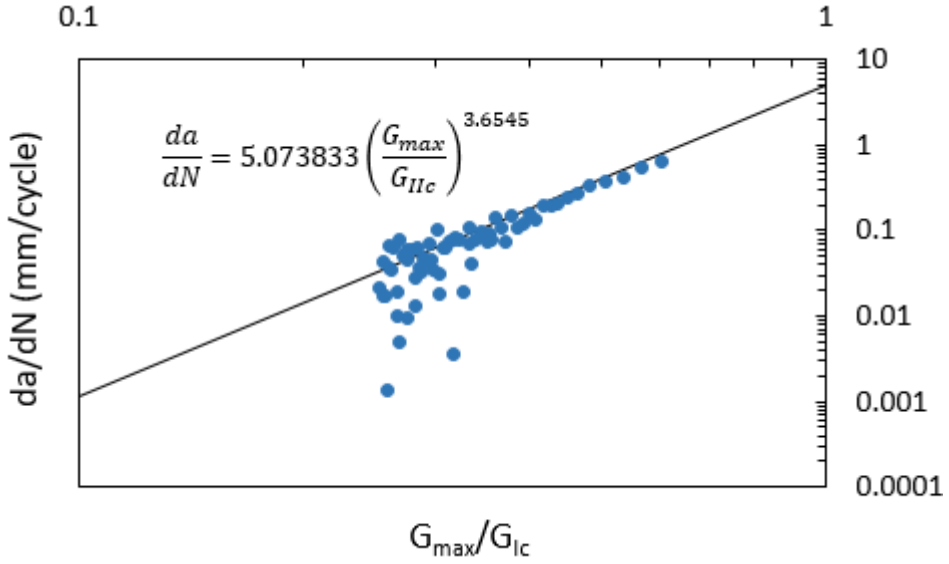

Figure 56 - Representative ENF fatigue crack growth curve. The trendline shown is the average for all tests.

After testing specimens from all conditions, similar FCG curves were obtained. Figure 57 shows a comparison of the obtained Paris law parameters for each condition. As seen in Figure 58b, the PL intercept, similarly to the DCB tests, shows high standard deviation which is natural given the nature of the FCG curves. There was also a clear difference between the C values obtained. This may be explained by a problem that was detected in the precracking stage: cracks did not open to the same extent, which later was a major differentiator in the fatigue testing stage since the time it took to open a visible crack varied from specimen to specimen (even though the rest of the test was more uniform). This led to different PL intercept values for the same type of test.

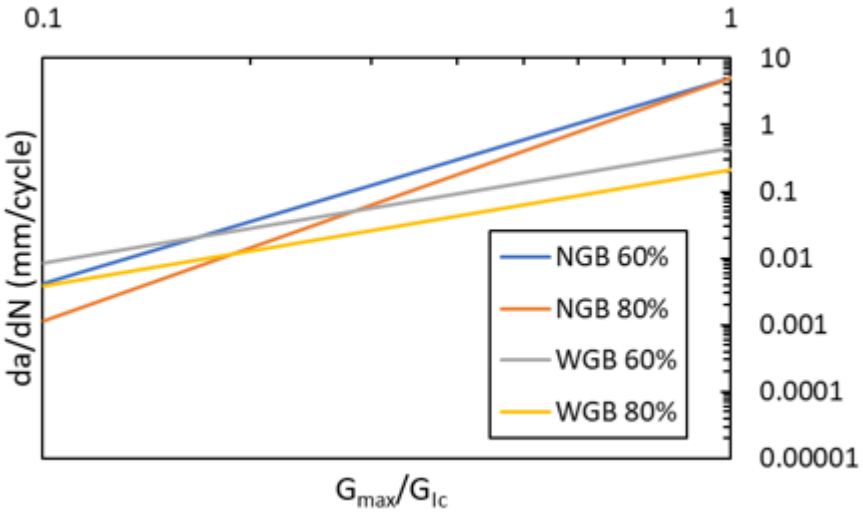

Figure 57 - ENF Paris law trends plotted in the same graph, NGB refers to specimens without glass beads and WGB refers to specimens with glass beads.

Comparing the ENF tests done at 60% and at 80% of the maximum load, it was noticed that the Paris law slope was not affected (Figure 58a) however, when comparing specimens with and without beads, a clear decrease was seen indicating that the presence of beads improves mode II fatigue behavior. In mode I the effect of the beads was not clear but for a 60% load the Paris law slope decreased. For mode II, it is possible that the effect of the beads is clearer because crack pinning is more effective for this type of load. Considering that beads are rigid, and they occupy all the adhesive thickness, they constitute a clear obstacle to crack propagation by resisting some of the shear stress.

The number of cycles to failure, shown in Figure 58c, describes the same trend seen in the DCB tests, decreasing with increasing loads, which is expected. In Figure 58d, it was seen that the threshold energy release rate increases with the load increase due to the energy release rate being directly related to the load applied as seen in the Irwin-Keys equation.

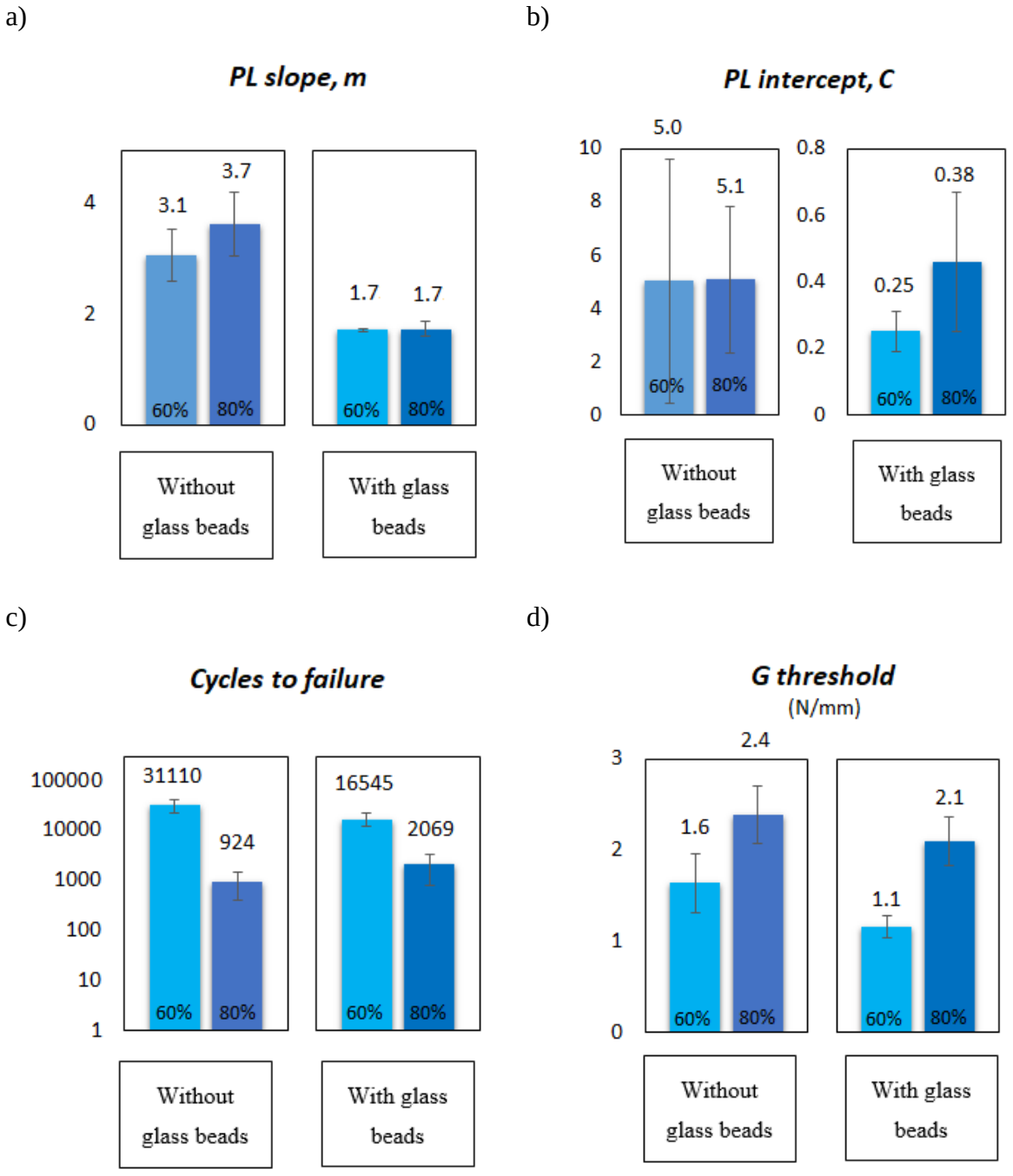

Figure 58 - Fatigue results for mode II, ENF tests, a) Paris law slope results, b) Paris law y-intercept results, c) cycles to failure results, d) G_{th} results.

Comparing the DCB tests to the ENF tests, two main aspects stand out. Firstly, the Paris law slope is higher in the DCB tests, which happens because adhesives perform better when loaded in shear, thus it is expected that applying opening forces leads to the adhesive failing faster. Secondly, the threshold energy release rate is higher in the ENF tests. This is explained by the fact that more energy is required for a crack surface to appear in mode II than in mode I. This trend was documented before [58].

4.4.3 Mixed-mode

The mixed-mode fatigue analysis was performed for the same phase angles used in the quasi-static tests, for a φ of 22.2° and 56.6°. The measurements were accomplished the same way as for quasi-static conditions, two LVDT measured the top and bottom adherend's arm displacement δ_1 and δ_2, and the load P, was registered by the universal test machine throughout each test. CBBM was used to provide values for both equivalent crack lengths a_{eqI} and a_{eqII}, and the energy release rate values correspondent of each mode G_I and G_{II}.

The information retained by the two LVDT is displayed in Figure 59.

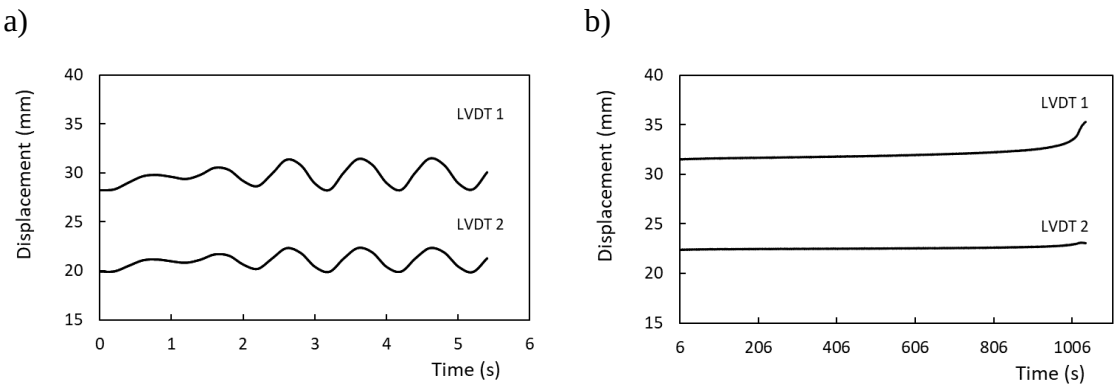

Figure 59 - LVDT output: a) complete signal of the beginning of the fatigue loading converted to millimeters, b) set of maximum values, information used to build the FCG curve.

Figure 59 shows the displacement experienced by each adherend's arm throughout the test. In Figure 59a the first cycles can be seen, when the machine was still adjusting to the target load and frequency. The displacement until the end of the test can be seen in Figure 59b. Note that Figure 59b displays only the maximum displacements reached in each cycle.

The energy release rate and the equivalent crack length relate similarly to the number of cycles, both increasing in a controlled manner at first, followed by an increase which ultimately leads to abrupt failure. Figure 60 shows how the mode I component for the equivalent crack length and the energy release rate evolve throughout test. Figure 60a shows the equivalent crack length as function of the number of cycles, Figure 60b shows the evolution of energy release rate as function of equivalent crack length. Results for the mode II component follows a similar trend, the only difference being the maximum value of the energy release rate.

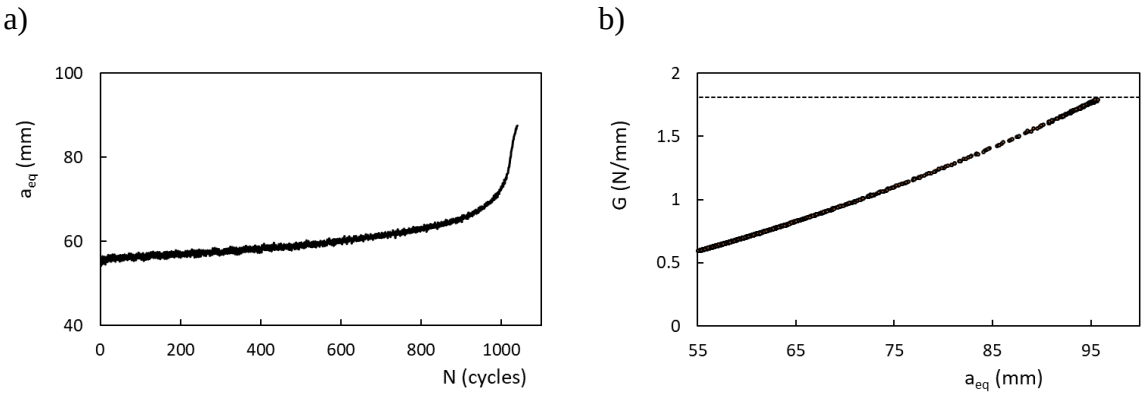

Figure 60 - a) Equivalent crack length as function of the number of cycles, b) energy release rate as function of equivalent crack length.

The initial plan was performing fatigue tests at 80% of maximum quasi-static load but seeing that the first specimens tested were failing too suddenly, the load was lowered to 60% of the maximum quasi-static load in hopes to better capture the stable crack propagation. No difference in performance was noticed between the specimens with and without beads. The FCG curves displayed below are characteristic curves for specimens loaded at 60% and 80% of the quasi-static failure load obtained for each mode.

4.4.4 Mixed-mode (φ=22.2°)

Following the procedure described above, which was similar to the static testing, the FCG curves for φ=22.2° are displayed in Figure 61.

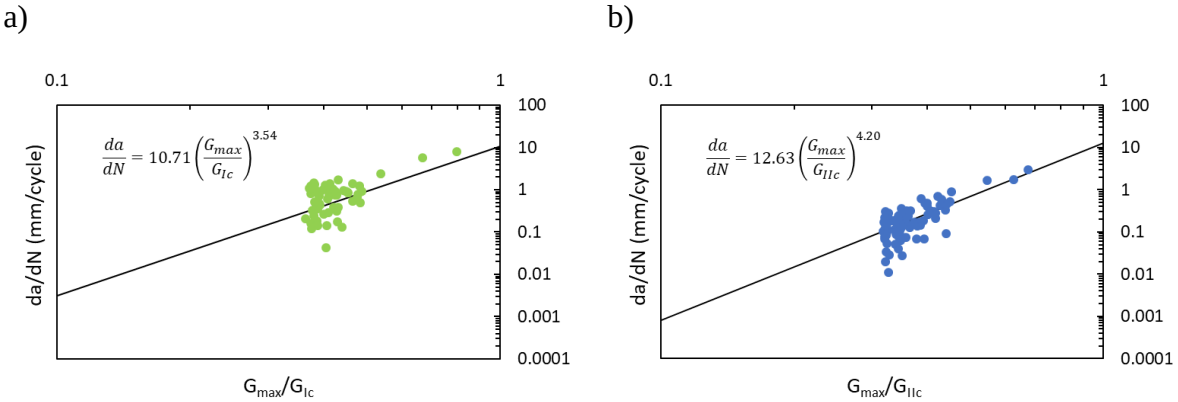

Figure 61 - Resulting FCG curves for a phase angle of 22.2°: a) mode I component, b) mode II component.

The resulting values for the fatigue testing are shown in Figure 62. Paris law slope results in Figure 62a were within the expected considering the pure mode results, Table 13 shows the

total Paris law slope, obtained with Equation (36) which is between the pure mode I and pure mode II results. Considering the literature, the results are within the expected values because similar Paris law slope values have been obtained for phase angles near 22.2° [47, 49, 50].

Table 13 - Paris law slope for φ=22.2°.

$\varphi_{apparatus}$ (°)	m_I	m_{II}	m_T	Load (%)
22.2	4.20 ± 0.34	3.54 ± 0.01	5.50 ± 0.25	60
	4.62	2.76	5.38	80

Similarly to the ENF, the PL intercept results, shown in Figure 62b, not only show a big dispersion but also different mean values for each condition, which is also explained by the difference in crack size, resulting from the pre-cracking stage.

a) b)

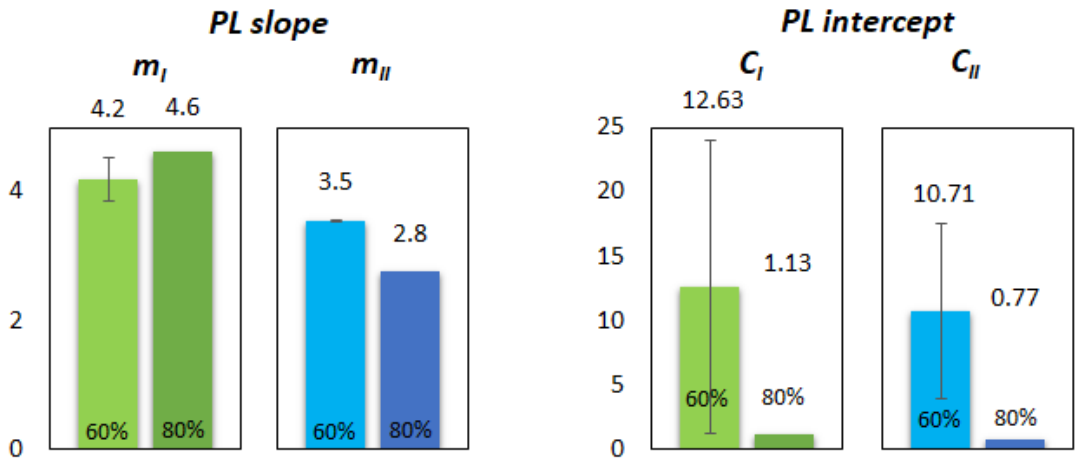

c) d)

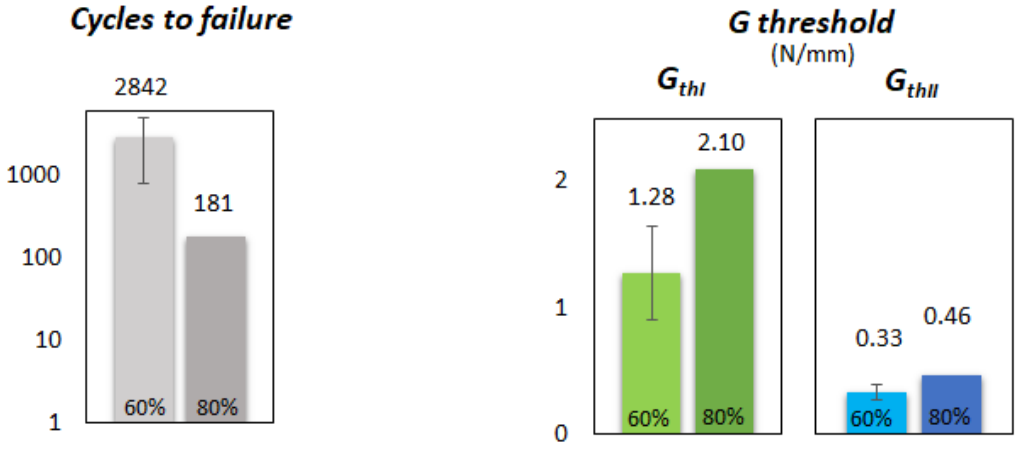

Figure 62 - Fatigue results for φ=22.2°: a) Paris law slope results, b) Paris law intercept results, c) cycles to failure results, d) threshold energy release rate results.

As seen in Figure 62c, the cycles to failure follow the same trend noticed in the previously exposed modes, decreasing with the load increase, as expected. Figure 62d shows the threshold energy release rate values, where the mode I component is higher than the mode II. This is expected since for this mixed-mode angle the load is mainly of mode I, a trend also seen in the static testing. The load increase also led to an increase in the threshold energy release rate, which is expected according to Equation (5).

4.4.5 Mixed-mode (φ=56.6°)

After submitting the specimens to the fatigue loading, the FCG curves shown in Figure 63 were obtained for φ=56.6° using the CBBM.

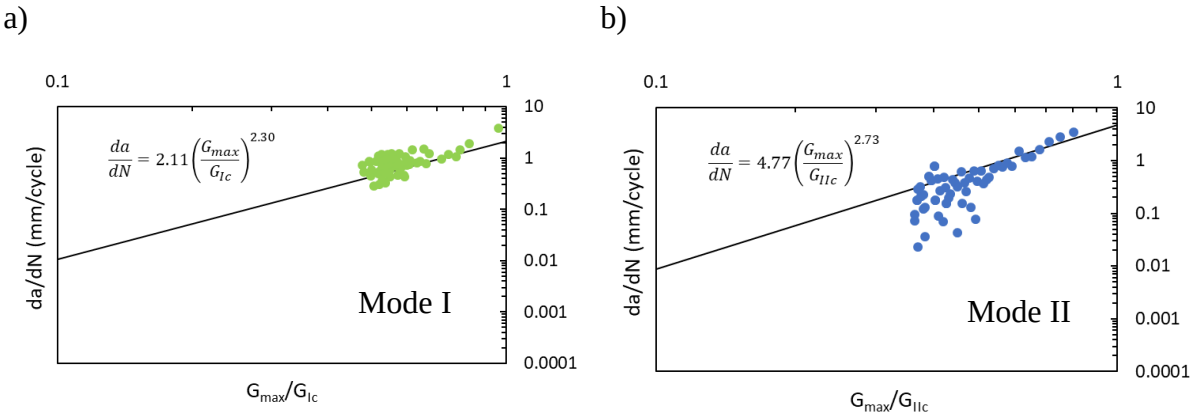

Figure 63 - Representative mixed-mode FCG curves correspondent of each mode, a) mode I component, b) mode II component.

The resulting values for the tested conditions are displayed in Figure 64, as seen in Figure 64a, the PL slope does not appear to be influenced by the load percentage, and the values, which can be seen in Table 14, are within the expected when compared with the literature (see Figure 23). The total Paris law slope was calculated with Equation (36).

Table 14 - Total Paris law slope for φ=56.6°, according to Equation (36).

$\varphi_{apparatus}$ (°)	m_I	m_{II}	m_T	Load (%)
56.6	2.38 ± 0.64	3.35 ± 0.32	4.16 ± 0.32	60
	2.30 ± 0.18	2.73 ± 0.37	3.58 ± 0.32	80

Shown in Figure 64b, the PL intercept values tend to vary with each condition. This is expected due to the discrepancy of C in the crack initiation instant, which is dependent on the size of the pre-crack. The number of cycles to failure are shown in Figure 64c, the expected trend was seen where the number of cycles endured by the specimens decreases with the load increase. The threshold energy release rates, shown in Figure 64d, were higher for mode II than for mode I, which is expected since the energy at play to open new crack surface for this phase angle is higher in mode II is than in mode I. The effect of the load increase, however, was less noticed than for the other tested angles, this might be due to the apparatus' structure, in this given angle, acting as a damper for the specimens.

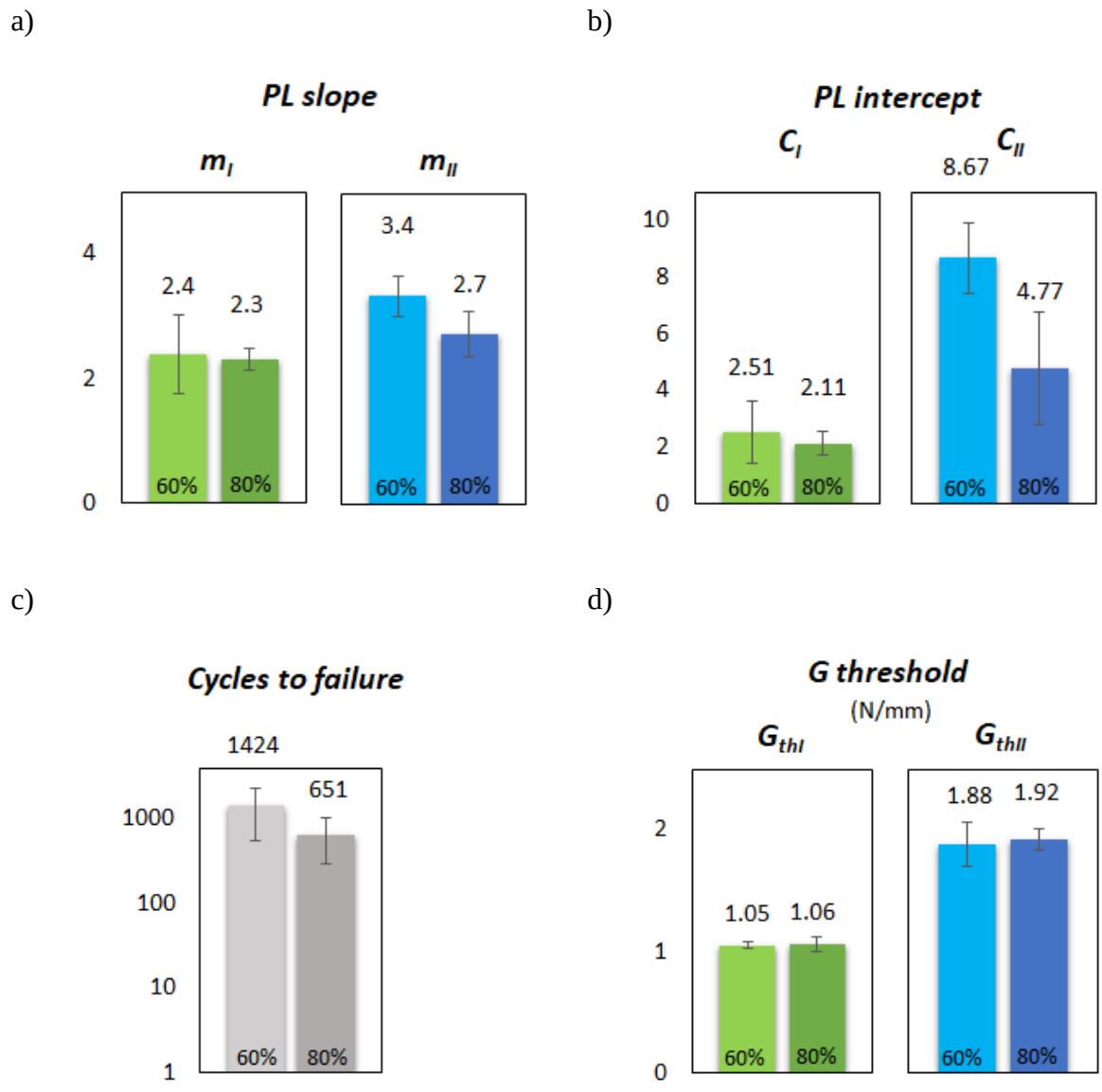

Figure 64 - Fatigue results for φ=56.6°: a) Paris law slope results, b) Paris law intercept results, c) cycles to failure results, d) threshold energy release rate results.

4.5 Paris law envelopes

The Paris law slope envelope displayed in Figure 65 was put together with the fatigue results of each pure mode and the results from the mixed-mode tests. It was seen that the pure modes I and II display the highest and lowest slopes, respectively, while the mixed-mode slopes are situated between these values. It was noticed that the existence of mode II type loads influences the fatigue behavior greatly, as for φ=22.2°, not only the mode II Paris law slope has a considerable value but mode I also decreases considerably comparing to the pure mode I results. The envelope was constructed with a power law to fit the points. The envelope can eventually be improved if more phase angles are tested.

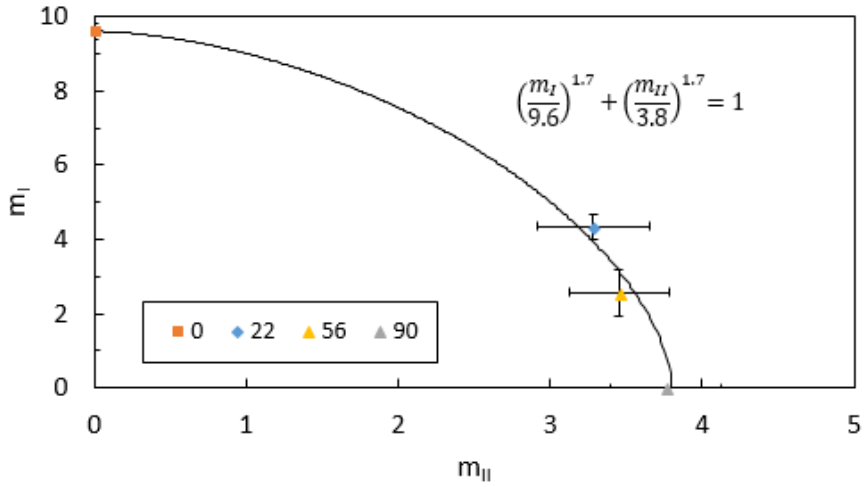

Figure 65 - Paris Law slope envelope.

An envelope for the threshold energy release rate, displayed in Figure 66, was obtained using a quadratic fit. It is interesting to notice that a similar trend was detected for the static testing, where an increase near mode I was followed by a decrease (in mode I) until pure mode II, which is the highest value in both cases.

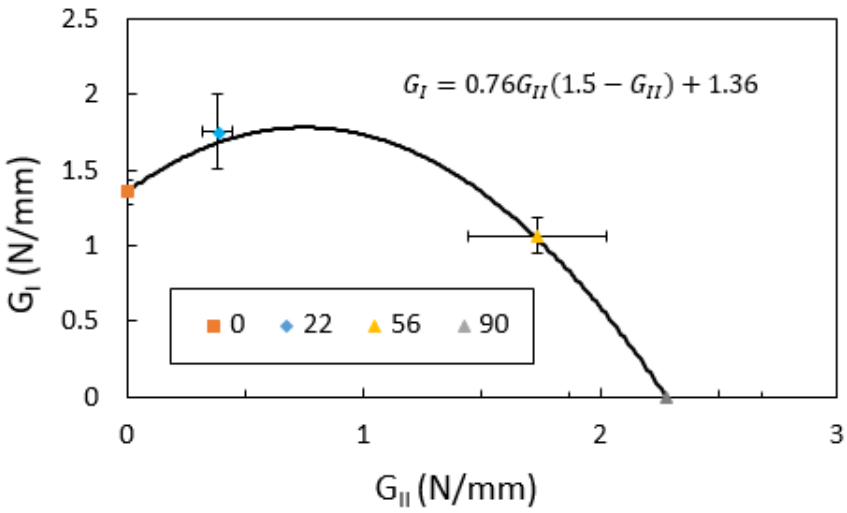

Figure 66 - Threshold energy release rate envelope.

Figure 67 shows both envelopes plotted together. A clear difference between mode I and mode II was noticed, where the G_{th} value and the critical energy release rate value seem to distance themselves as the mixed-mode phase angle increases.

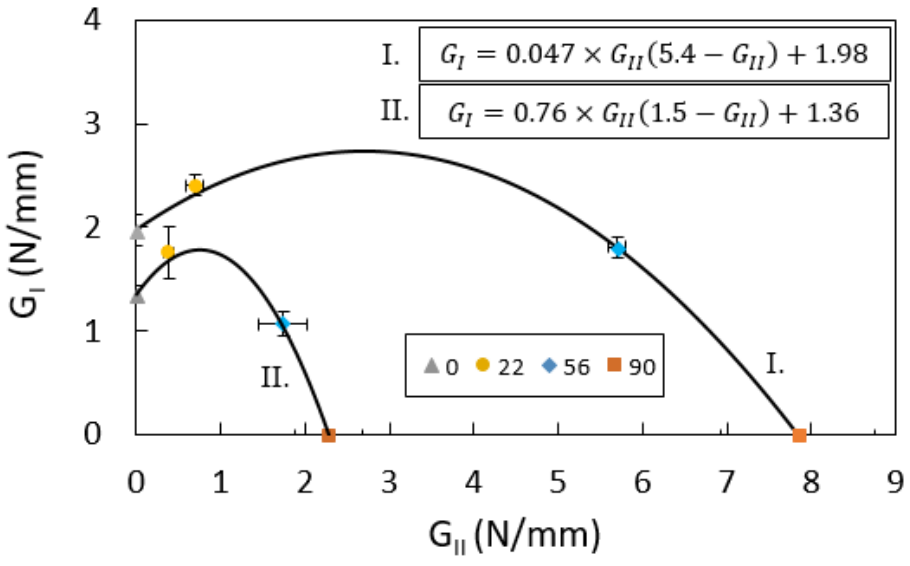

Figure 67 - Threshold energy release rate envelope (II.) plotted with the static envelope (I.), both fitted with the quadratic criterion.

Table 15 shows the threshold as a function of the phase angle in terms of percentage of the total fracture energy obtained in the quasi-static tests. It was seen that the threshold $\%G_c$ decreases as it gets closer to mode II. This might be explained by analyzing the FPZ in the DCB and the ENF tests. Figure 68 was obtained using ABAQUS®, where it is possible to notice that the

adhesive in the DCB test exhibits a smaller FPZ, while on the ENF the FPZ occupies a much higher bonded area. The higher FPZ of the ENF specimen will contribute to a quicker plastic degradation of the relevant bonded area, and considering that the ENF also experiences compressive loads on the adhesive layer (inducing further adhesive degradation), the combination of these phenomena may explain the lower threshold values near mode II.

Table 15 - Percentage of the critical fracture energy as a function of the phase angle.

φ (°)	Threshold $\%G_c$ (%)
0	68
22.2	72
56.6	34
90	29

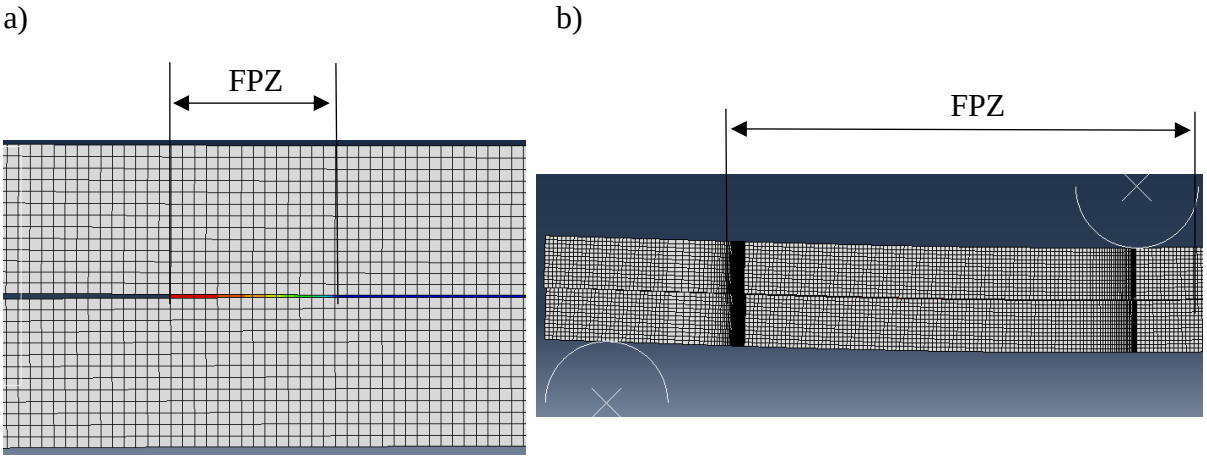

Figure 68 - Comparison between the FPZ, a) DCB specimen, b) ENF specimen.

An envelope for the PL intercept was not possible because this value is influenced by the number of cycles of the test. As the dispersion of the number of cycles to failure was too great, the PL intercept was less accurate.

4.6 Parameters as function of phase angle

To further understand how the phase angle affects adhesive behavior, test results were plotted as function of the phase angle.

4.6.1 Energy release rate

Figure 69 displays the total energy release rate, obtained using Equation (32), as function of the phase angle.

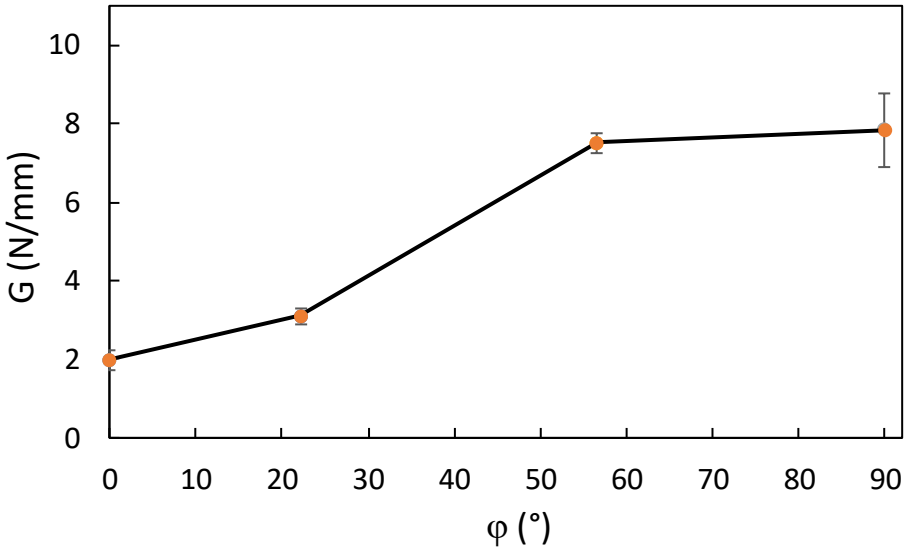

Figure 69 - Total fracture energy as function of the phase angle.

Mode I has the lowest fracture energy, which is expected. A close relation between phase angle and fracture energy was found: as the phase angle increases, the mode II component increases and consequently, fracture energy increases. This is expected and exposed in the literature, for example, Costa et al. obtained similar results for three tested epoxy adhesives [56].

4.6.2 Paris law Slope

Figure 70 shows the total Paris law slope, obtained with Equation (36), as a function of the phase angle.

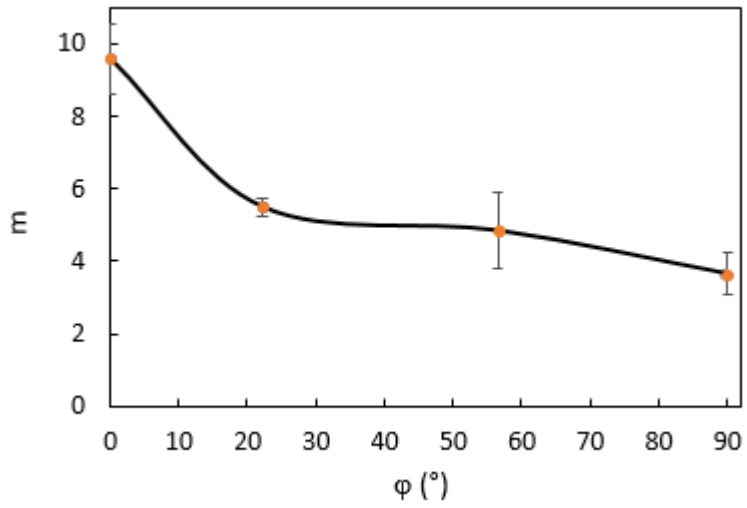

Figure 70 - Paris law slope as a function of the mixed-mode phase angle.

The total Paris law slope decreases as the phase angle increases. Thus, making it possible to conclude that the presence of mode II loads delays crack propagation as opposed to loads closer to mode I. This is expected, as it goes accordingly with the energy release rate results, which describes the opposite trend. As more energy is needed to form fracture surface, the Paris law slope tends to decrease. Similar results were obtained by Férnandez et al. [43], who used CFRP specimens in SLB tests to build FCG curves. Férnandez obtained a higher slope for mode I, while for a mixed-mode phase angle of 40° and pure mode II the slope was more similar, with the mode II slope being slightly smaller.

5 Numerical analysis

A numerical simulation was implemented using ABAQUS® to model the experimental fracture results. Models for the DCB, ENF and mixed-mode tests using the apparatus were implemented. The adherends were modelled as 4-node bilinear elements (CPE4R) and the adhesive layer was modelled as 4-node two-dimensional cohesive elements (COH2D4). The adherends were modeled using steel's mechanical properties.

Damage initiation and propagation in the adhesive were simulated using a triangular traction-separation law. The used adhesive's properties were determined experimentally and are displayed in Figure 71. For each mode, rigidity, maximum stress and fracture energy were inputted. The shear modulus was deduced from the Young's modulus using a Poisson's ratio, ν, of 0.33.

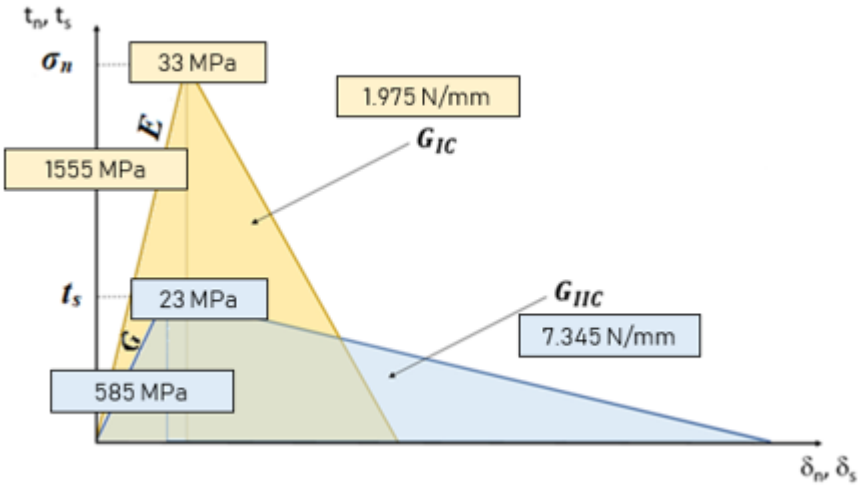

Figure 71 - Adhesive properties used in ABAQUS® for the triangular traction-separation law.

The used mesh is shown in Figure 72, where the elements were organized in size given their proximity to the adhesive layer, since this area has the most importance for the calculations. In total, 66 975 elements were assigned. The adhesive layer is composed of only one layer, 0.3mm thick.

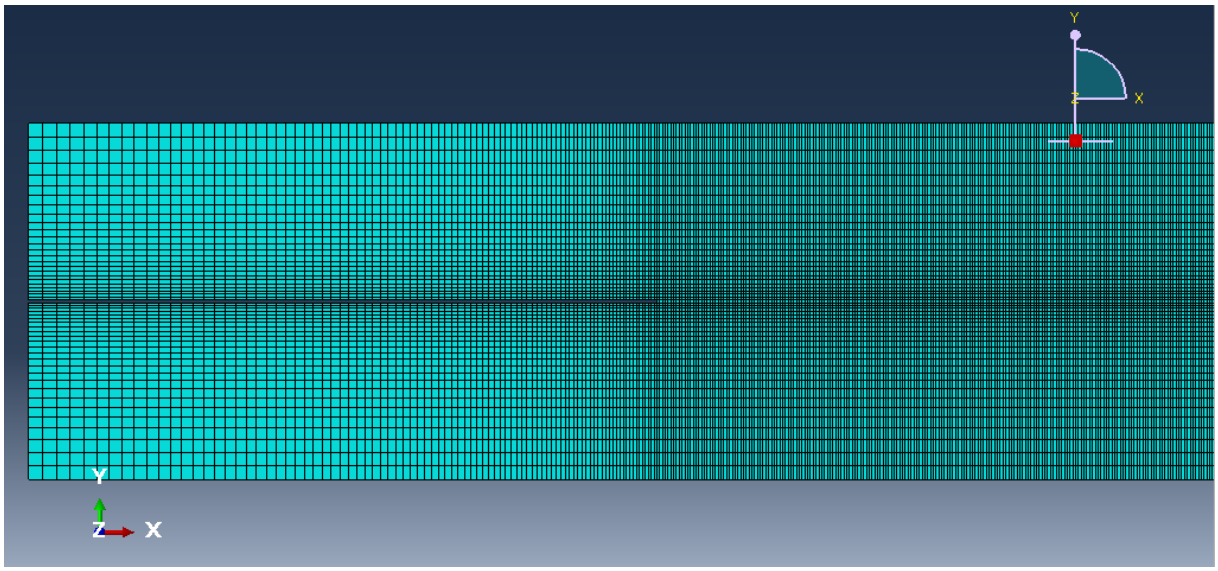

Figure 72 - Meshed DCB type specimen, used in the numerical modeling.

5.1 Mode I model

A schematic of the DCB test is displayed in Figure 73, as well as the boundary conditions imposed in the model to simulate the test.

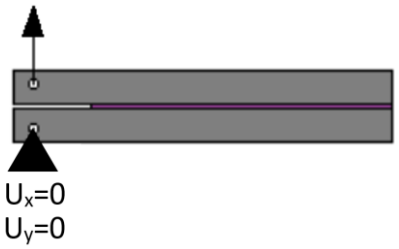

Figure 73 - Schematic of the geometric restrictions of the DCB model.

The resulting P-δ curve is displayed below in Figure 74. It was seen that the rigidity and the maximum load were higher in the numerical curve. The different rigidity is due to the test machine, which also measures the displacements of the components in the machine as they are being loaded as well. The difference in the maximum load might be due to experimental imperfections in the adhesive layer.

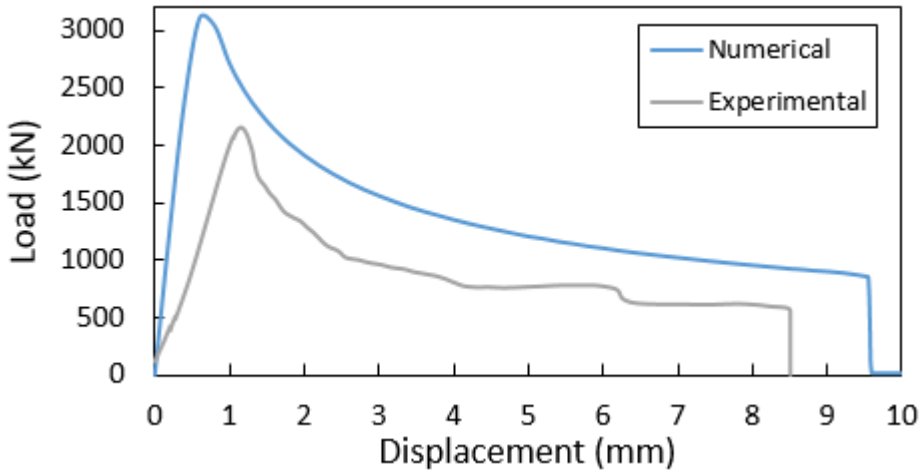

Figure 74 – Load-displacement curves of an experimental curve compared to the obtained numerical simulation.

As seen in Figure 75, the values for the plateaus in the *R-curves* were very similar, as only a difference of 0.2 N/mm was noticed. The representative experimental curve is in grey, and the numerical result in blue. The only detectable difference between the curves is that in the experimental curves, G values drop slightly before stabilizing, while the numerical curve is always stable after reaching the plateau.

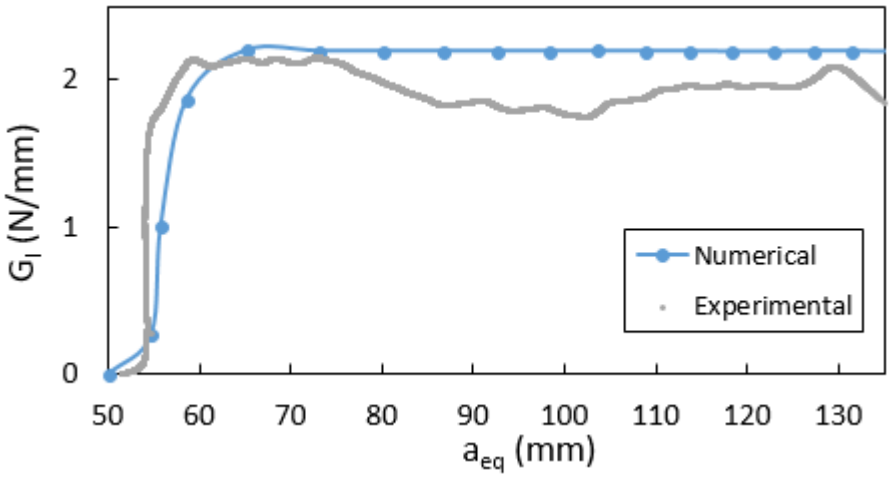

Figure 75 - *R-curve* for the numerical DCB test.

5.2 Mode II model

Figure 76 displays a schematic of the ENF test showing the conditions imposed in the model to simulate the test. Two fixed cylinders were placed under the specimen in each side, and a displacement was imposed in the middle to simulate the load. The diameter of the cylinders and the distance between them was the same as used in the experimental procedure.

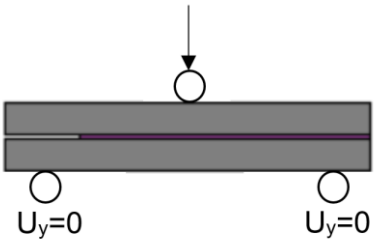

Figure 76 - Schematic of the geometric restrictions of the ENF model.

The comparison to the modeled load-displacement curves for the ENF test are shown in Figure 77a. The simulation of ENF tests is sometimes hard to achieve since low displacements are felt in the adhesive. When using the experimental properties in the model, it was not possible to calculate G because crack propagation did not occur, which was due to the displacements in the cohesive elements not reaching the maximum values set by the triangular law. As demonstrated in Figure 77b, to overcome this problem the maximum tension was increased from 23MPa to 30 MPa to force a reduction of the maximum displacement, while maintaining the G value. The reduced maximum displacement made it possible for crack propagation to occur.

The numerical curve shows higher rigidity than the experimental, which is expected due to components in the experimental test machines absorbing part of the energy when loaded, translating to higher displacements for the same load. An inflexion was not seen when using a maximum tension of 23 MPa.

a) b)

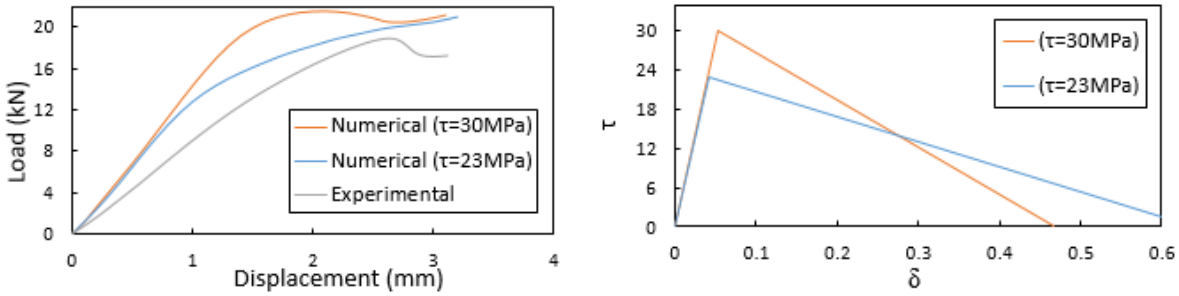

Figure 77 – a) Load-displacement curves obtained for the numerical simulations, b) effect of changing maximum τ in the cohesive law.

As seen in Figure 78, the obtained resistance curve using a maximum tension of 23MPa, in blue, does not tend to stabilize, which happens in the representative experimental curve, in gray. This is expected given that no inflexion was seen in the respective $P-\delta$ curve. When using a maximum tension of 30MPa, a small plateau can be seen near 12N/mm. This value is higher than the experimental result, which is expected since the maximum tension was increased substantially.

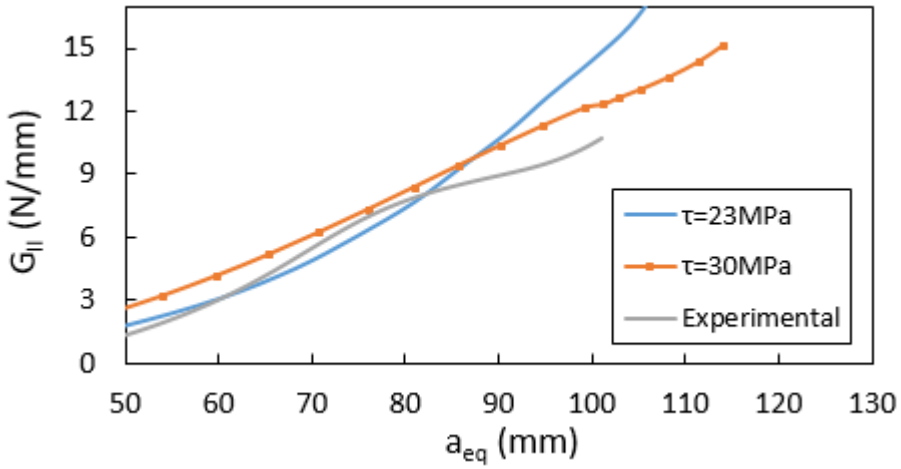

Figure 78 - *R*-curve for the numerical ENF test.

5.3 Mixed-mode model (φ=22.2˚)

The test setup was modeled using the boundary conditions shown in Figure 79. The apparatus was modeled as rigid beam elements connected by MPC Pin links. A displacement was forced in the top, while the three reaction points were simulated by allowing no displacement.

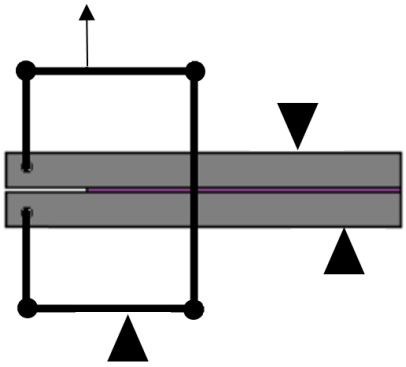

Figure 79 - Test setup for the mixed-mode phase angle of 22.2°.

Load-displacement curves are shown in Figure 80 where the numerical outcome is compared to the experimental curves. Similarly to the other simulations, the numerical curve is more rigid and has a higher maximum load, which is expected.

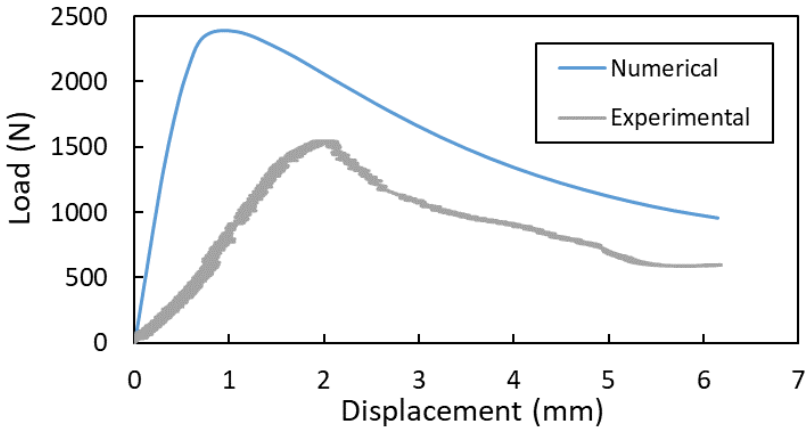

Figure 80 - Load-displacement curves for φ=22.2°, mode I components.

Using the CBBM, resistance curves were obtained, as shown in Figure 81. The mode I curves show similar results, as the plateau is at a close value when comparing the numerical and the experimental result. The mode II curves show different G values, which might be due to the difference in the experimental phase angle being above 22.2°.

a) b)

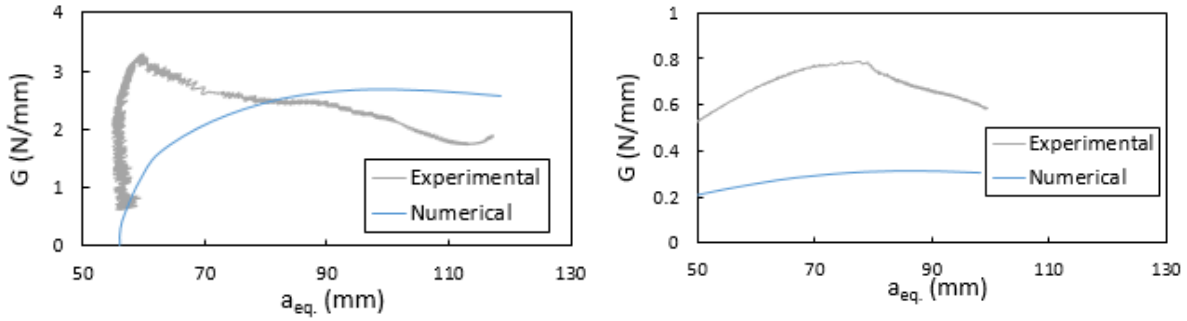

Figure 81 - *R-curves* for φ=22.2°, a) mode I component, b) mode II component.

5.4 Mixed-mode model (φ=56.6˚)

The model for the test setup for φ=56.6° was similar to the one used for 22.2°, where the only difference is the size of the beams. The model is shown in Figure 82.

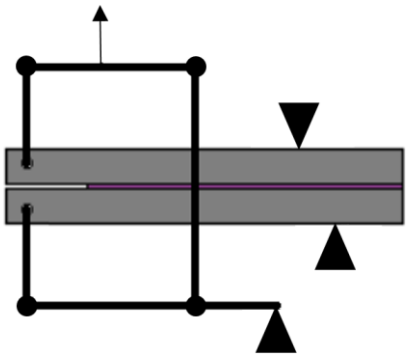

Figure 82 - Test setup for the mixed-mode phase angle of 56.6°.

The numerical load-displacement curves are more rigid and reach higher maximum loads, as expected. The curves are shown in Figure 83.

a) b)

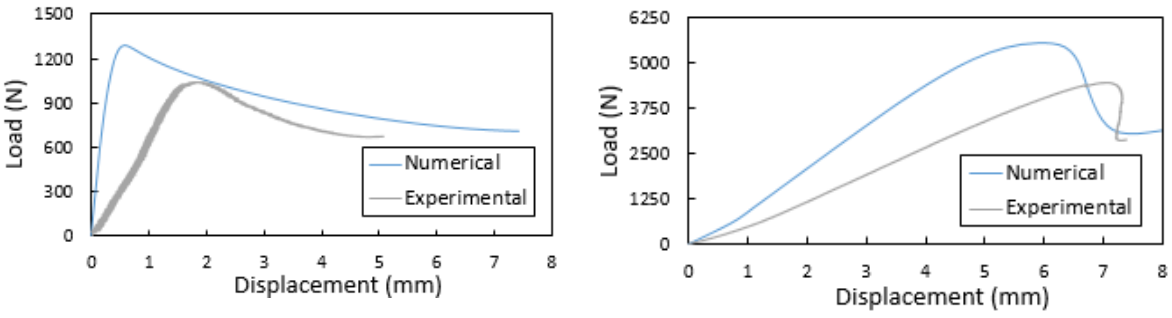

Figure 83 - Load-displacement curves for φ=56.6°, a) mode I component, b) mode II component.

The resulting resistance curves are displayed in Figure 84, where both mode's components reached similar values to the respective experimental curve.

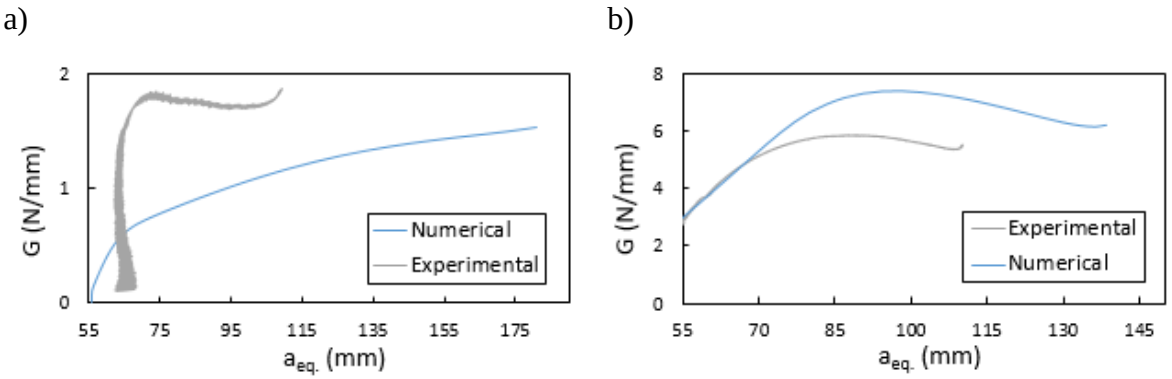

Figure 84 - *R-curves* for φ=56.6°, a) mode I component, b) mode II component.

5.5 Numerical results in the envelope

In Figure 85, the obtained numerical values were plotted in the same graph as the experimental static envelope, to better compare the numerical values with the experimental results. The same trend as the experimental envelope can be seen, as the φ=22.2° results show the same increase near mode I. Results for φ=56.6° are slightly different but seem to maintain close to the experimental envelope. For all angles, the obtained results were slightly higher than the respective experimental result, which is expected since there are no imperfections. The results for the ENF model are specially higher since the maximum tension was increased.

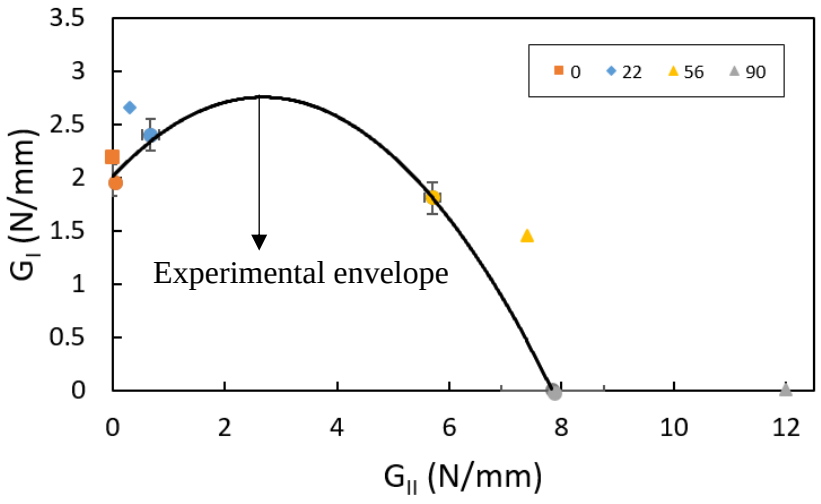

Figure 85 - Static envelope containing the results from the numerical simulations overlapped with the experimental envelope, in circles.

6 Conclusions and future works

6.1 Conclusions

The main objective of this dissertation was to assess the mixed-mode fatigue behavior of Henkel Teroson EP 5089. Since beads are used with this adhesive to ensure thickness, specimens were tested with and without glass beads to evaluate if mechanical performance was affected. Bulk results showed that both the rigidity and strength where not affected by the presence of beads, while the strain to failure values showed that specimens with beads had better performance (5.96% vs 7.23%). By performing fracture tests, it was seen that the energy release rate for the pure modes varied slightly, while the same did not happen in mixed-mode conditions. For DCB and ENF, the energy release rates decreased around 5% with the inclusion of beads, however, this could be due to the dispersion of the tests only. In the fatigue tests, it was also seen that the presence of beads did not affect specimens loaded in mixed-mode, while for the pure modes it was seen that using beads improves fatigue results considerably, which might be related to the improved strain to failure shown by specimens with beads.

To perform the fatigue analysis, DCB, ENF and mixed-mode fracture tests were required to obtain the maximum load to later use in fatigue. Using the data obtained, a fracture envelope was compiled, where an increase near mode I was seen. This appears to confirm other trends shown in the literature [56], where this increase appears to be related to the ductility of the adhesive.

After performing the fatigue tests, it was noticed that the envelope for the threshold energy release rate is similar to the static envelope, only with smaller values. This is expected since fatigue loading is done at a percentage of the maximum load, making the G values measure bellow the critical G calculated in quasi-static conditions. By testing different load percentages it was seen that increasing the load makes the threshold energy release rate increase, while the opposite trend was seen for the cycles to failure, where the load increase originated a drop in the cycles to failure. The Paris law slope envelope appears to be fitted by a power law criterion, where the total Paris law slope decreases as the presence of mode II increases, indicating that the presence of mode II loads delays crack propagation.

6.2 Future works

Performing tests to characterize the adhesive in shear, such as TAST, would be important as they would provide important information for mode II that could later be used in the numerical modeling.

The envelopes would improve if more mixed-mode phase angles were tested, allowing a more precise envelope.

Completing more fatigue tests would help reduce dispersion and ultimately lead to better results.

Higher control in the precracking stage would be very important since it would allow for more consistent PL intercept values. This would possibly lead to acceptable PL intercept envelopes. Also, to further understand this phenomenon, it would be interesting to test fatigue in specimens with different a_0 lengths to see the effect on the PL intercept.

Studying the influence of the loading mode on the fracture mechanism might help understand the different $\%G_c$ values seen for each mode.

It was seen that the load percentage applied in fatigue testing has influence in some of the parameters studied, it would be interesting to test this effect for smaller load percentages.

References

[1] P. Kozowyk, M. Soressi, D. Pomstra, and G. Langejans, "Experimental methods for the Palaeolithic dry distillation of birch bark: implications for the origin and development of Neandertal adhesive technology," *Scientific Reports*, vol. 7, no. 1, p. 8033, 2017.

[2] L. F. M. da Silva, A. G. de Magalhaes, and M. F. S. de Moura, *Juntas adesivas estruturais*. Publindústria, 2007.

[3] L. F. Da Silva, A. Öchsner, and R. D. Adams, *Handbook of adhesion technology*. Springer Science & Business Media, 2011.

[4] N. Chowdhury, W. K. Chiu, J. Wang, and P. Chang, "Static and fatigue testing thin riveted, bonded and hybrid carbon fiber double lap joints used in aircraft structures," *Composite Structures*, vol. 121, pp. 315-323, 2015.

[5] F. Moroni and A. Pirondi, "Technology of rivet: adhesive joints," in *Hybrid Adhesive Joints*: Springer, 2010, pp. 79-108.

[6] B. Täljsten, "The importance of bonding—A historic overview and future possibilities," *Advances in Structural Engineering*, vol. 9, no. 6, pp. 721-736, 2006.

[7] "Agricultural & construction equipment solutions," Henkel, Ed., ed, 2016.

[8] M. De Moura, J. Gonçalves, J. Chousal, and R. Campilho, "Cohesive and continuum mixed-mode damage models applied to the simulation of the mechanical behaviour of bonded joints," *International Journal of adhesion and Adhesives*, vol. 28, no. 8, pp. 419-426, 2008.

[9] F. J. Chaves, L. Da Silva, M. De Moura, D. Dillard, and V. Esteves, "Fracture mechanics tests in adhesively bonded joints: a literature review," *The Journal of Adhesion*, vol. 90, no. 12, pp. 955-992, 2014.

[10] S. T. Rolfe and J. M. Barsom, *Fracture and fatigue control in structures: applications of fracture mechanics*. ASTM International, 1977.

[11] H. M. Westergaard, "Bearing pressures and cracks," *Journal of applied mechanics*, vol. 6, no. 2, pp. A49-A53, 1939.

[12] A. A. Griffith and M. Eng, "VI. The phenomena of rupture and flow in solids," *Phil. Trans. R. Soc. Lond. A*, vol. 221, no. 582-593, pp. 163-198, 1921.

[13] D. Broek, *Elementary engineering fracture mechanics*. Springer Science & Business Media, 2012.

[14] D. Jablonski, "Fatigue crack growth in structural adhesives," *The Journal of Adhesion*, vol. 11, no. 2, pp. 125-143, 1980.

[15] G. R. Irwin, "Analysis of stresses and strains near the end of a crack traversing a plate," 1957.

[16] M. Karimi, T. Roarty, and T. Kaplan, "Molecular dynamics simulations of crack propagation in Ni with defects," *Modelling and Simulation in Materials Science and Engineering*, vol. 14, no. 8, p. 1409, 2006.

[17] L. F. M. Da Silva and A. Öchsner, *Modeling of adhesively bonded joints*. Springer, 2008.

[18] G. Barenblatt, "Equilibrium cracks formed on a brittle fracture," *Doklady Akademii Nauk Sssr*, vol. 127, no. 1, pp. 47-50, 1959.

[19] A. Hillerborg, M. Modéer, and P.-E. Petersson, "Analysis of crack formation and crack growth in concrete by means of fracture mechanics and finite elements," *Cement and concrete research*, vol. 6, no. 6, pp. 773-781, 1976.

[20] H. Khoramishad, A. Crocombe, K. Katnam, and I. Ashcroft, "Predicting fatigue damage in adhesively bonded joints using a cohesive zone model," *International Journal of fatigue*, vol. 32, no. 7, pp. 1146-1158, 2010.

[21] ASTM, "Standard Test Method for Fracture Strength in Cleavage of Adhesives in Bonded Joints," vol. ASTM D3433-99, 2004.

[22] "Determination of the mode 1 adhesive fracture energy of structural adhesive joints using double cantilever beam and tapered double cantilever beam specimens," vol. ISO 25217.

[23] L. F. Da Silva, D. A. Dillard, B. Blackman, and R. D. Adams, *Testing adhesive joints: best practices*. John Wiley & Sons, 2012.

[24] B. R. Blackman and A. J. Kinloch, "Protocol for the determination of the Mode I adhesive fracture energy, GIc, of structural adhesives using the double cantilever beam (DCB) and tapered double cantilever beam (TDCB) specimens," *Version 00-08. European Structural Integrity Society Polymers, Adhesives and Composites TC4 Committee*, 2000.

[25] M. De Moura, R. Campilho, and J. Gonçalves, "Crack equivalent concept applied to the fracture characterization of bonded joints under pure mode I loading," *Composites Science and Technology,* vol. 68, no. 10-11, pp. 2224-2230, 2008.
[26] L. Da Silva, V. Esteves, and F. Chaves, "Fracture toughness of a structural adhesive under mixed mode loadings," *Materialwissenschaft und Werkstofftechnik,* vol. 42, no. 5, pp. 460-470, 2011.
[27] M. De Moura, R. Campilho, and J. Gonçalves, "Pure mode II fracture characterization of composite bonded joints," *International Journal of Solids and Structures,* vol. 46, no. 6, pp. 1589-1595, 2009.
[28] R. Campilho and L. da Silva, "Mode I fatigue and fracture behaviour of adhesively-bonded carbon fibre-reinforced polymer (CFRP) composite joints," in *Fatigue and Fracture of Adhesively-Bonded Composite Joints*: Elsevier, 2015, pp. 93-120.
[29] F. J. Chaves, M. de Moura, L. da Silva, and D. A. Dillard, "Numerical validation of a crack equivalent method for mixed-mode I+ II fracture characterization of bonded joints," *Engineering Fracture Mechanics,* vol. 107, pp. 38-47, 2013.
[30] M. Costa, R. Carbas, E. Marques, G. Viana, and L. da Silva, "An apparatus for mixed-mode fracture characterization of adhesive joints," *Theoretical and Applied Fracture Mechanics,* vol. 91, pp. 94-102, 2017.
[31] T. Brussat, S. Chiu, and S. Mostovoy, "Fracture mechanics for structural adhesive bonds," LOCKHEED-CALIFORNIA CO BURBANK1977.
[32] A. Voloshin and M. Arcan, "Pure shear moduli of unidirectional fibre-reinforced materials (FRM)," *Fibre Science and Technology,* vol. 13, no. 2, pp. 125-134, 1980/03/01/ 1980.
[33] R. El-Hajjar and R. Haj-Ali, "In-plane shear testing of thick-section pultruded FRP composites using a modified Arcan fixture," *Composites Part B: Engineering,* vol. 35, no. 5, pp. 421-428, 2004/07/01/ 2004.
[34] S. Yoon and C. Hong, "Modified end notched flexure specimen for mixed mode interlaminar fracture in laminated composites," *International Journal of Fracture,* vol. 43, no. 1, pp. R3-R9, 1990.
[35] F. Xiao, C.-Y. Hui, and E. Kramer, "Analysis of a mixed mode fracture specimen: the asymmetric double cantilever beam," *Journal of Materials Science,* vol. 28, no. 20, pp. 5620-5629, 1993.
[36] G. Fernlund and J. Spelt, "Mixed-mode fracture characterization of adhesive joints," *Composites science and technology,* vol. 50, no. 4, pp. 441-449, 1994.
[37] S. Park and D. A. Dillard, "Development of a simple mixed-mode fracture test and the resulting fracture energy envelope for an adhesive bond," *International Journal of Fracture,* vol. 148, no. 3, pp. 261-271, 2007.
[38] "ASTM, "Standard test method for mixed mode I-mode II interlaminar fracture toughness of unidirectional fiber reinforced polymer matrix composites," vol. ASTM D6671-13e1, 2013. West Conshohocken, PA.."
[39] F. Chaves, L. Da Silva, M. de Moura, A. Dillard David, and J. Fonseca, "Apparatus and method for characterization of bonded joints mixed-mode I and II fracture, patent number: 20131000070010," *UP—Universidade do Porto, submitted patent,* 2013.
[40] G. Stamoulis, N. Carrère, J.-Y. Cognard, P. Davies, and C. Badulescu, "On the experimental mixed-mode failure of adhesively bonded metallic joints," *International Journal of Adhesion and Adhesives,* vol. 51, pp. 148-158, 2014.
[41] H. Chai, "Shear fracture," *International Journal of Fracture,* vol. 37, no. 2, pp. 137-159, 1988.
[42] M. Benzeggagh and M. Kenane, "Measurement of mixed-mode delamination fracture toughness of unidirectional glass/epoxy composites with mixed-mode bending apparatus," *Composites science and technology,* vol. 56, no. 4, pp. 439-449, 1996.
[43] M. V. C. Fernández, "Fracture Characterization of Composite Bonded Joints Under Fatigue Loading," 2013.
[44] W. De Goeij, M. Van Tooren, and A. Beukers, "Composite adhesive joints under cyclic loading," *Materials & design,* vol. 20, no. 5, pp. 213-221, 1999.
[45] A. Vassilopoulos, M. Shahverdi, and T. Keller, "Mode I fatigue and fracture behavior of adhesively-bonded pultruded glass fiber-reinforced polymer (GFRP) composite joints," in *Fatigue and Fracture of Adhesively-Bonded Composite Joints*: Elsevier, 2015, pp. 149-186.

[46] J. Renart, J. Costa, C. Sarrado, S. Budhe, A. Turon, and A. Rodríguez-Bellido, "Mode I fatigue behaviour and fracture of adhesively-bonded fibre-reinforced polymer (FRP) composite joints for structural repairs," in *Fatigue and Fracture of Adhesively-Bonded Composite Joints*: Elsevier, 2015, pp. 121-147.

[47] A. Pirondi and G. Nicoletto, "Mixed mode I/II fatigue crack growth in adhesive joints," *Engineering fracture mechanics,* vol. 73, no. 16, pp. 2557-2568, 2006.

[48] P. Carraro, G. Meneghetti, M. Quaresimin, and M. Ricotta, "Crack propagation analysis in composite bonded joints under mixed-mode (I+ II) static and fatigue loading: experimental investigation and phenomenological modelling," *Journal of Adhesion Science and Technology,* vol. 27, no. 11, pp. 1179-1196, 2013.

[49] T. Hafiz, M. Abdel-Wahab, A. Crocombe, and P. Smith, "Mixed-mode fatigue crack growth in FM73 bonded joints," *International Journal of Adhesion and Adhesives,* vol. 40, pp. 188-196, 2013.

[50] S. Azari, M. Papini, J. Schroeder, and J. Spelt, "The effect of mode ratio and bond interface on the fatigue behavior of a highly-toughened epoxy," *Engineering Fracture Mechanics,* vol. 77, no. 3, pp. 395-414, 2010.

[51] ASTM, "ASTM E647-15e1, "Standard Test Method for Measurement of Fatigue Crack Growth Rates"," 2015.

[52] G. Yoder, L. Cooley, and T. Crooker, "Procedures for precision measurement of fatigue crack growth rate using crack-opening displacement techniques," in *Fatigue Crack Growth Measurement and Data Analysis*: ASTM International, 1981.

[53] M. Imanaka, Y. Takeuchi, Y. Nakamura, A. Nishimura, and T. Iida, "Fracture toughness of spherical silica-filled epoxy adhesives," *International journal of adhesion and adhesives,* vol. 21, no. 5, pp. 389-396, 2001.

[54] H. Chai, "Deformation and fracture of particulate epoxy in adhesive bonds," *Acta metallurgica et materialia,* vol. 43, no. 1, pp. 163-172, 1995.

[55] D. Maxwell, R. Young, and A. Kinloch, "Hybrid particulate-filled epoxy-polymers," *Journal of materials science letters,* vol. 3, no. 1, pp. 9-12, 1984.

[56] M. Costa, R. Carbas, M. Benedita, E. Marques, G. Viana, L.F.M. da Silva, E Yokoi, S. Nakada, T. Furusawa + "Static assessment of the mixed-mode behaviour of three epoxy adhesives," *Engineering Fracture Mechanics,* vol. 182, pp. 552-565, 2017.

[57] S. Azari, G. Jhin, M. Papini, and J. Spelt, "Fatigue threshold and crack growth rate of adhesively bonded joints as a function of load/displacement ratio," *Composites Part A: Applied Science and Manufacturing,* vol. 57, pp. 59-66, 2014.

[58] S. Azari, M. Papini, J. Schroeder, and J. Spelt, "Fatigue threshold behavior of adhesive joints," *International Journal of Adhesion and Adhesives,* vol. 30, no. 3, pp. 145-159, 2010.